Università degli Studi di Modena e Reggio Emilia

DIPARTIMENTO DI INGEGNERIA "ENZO FERRARI"
Corso di Dottorato di Ricerca in Ingegneria Industriale e del Territorio - XXXIV ciclo

SSD ING-IND/10 - FISICA TECNICA INDUSTRIALE

Thermal Analysis of Power Module Devices for Hybrid Traction Vehicles

Candidato:
Massimo Sabato

Supervisori:
Chiar.mo Prof. Enrico Stalio
Dott. Federico Brusiani

Coordinatore del Corso:
Chiar.mo Prof. Alberto Muscio

Anno Accademico 2020-2021

"My mum always said:
Life is like a box of chocolates...
You never know what you're gonna get"

Forrest Gump

Acknowledgements

Non sono mai stato bravo a dedicare parole e ringraziamenti alle persone che mi hanno guidato, accompagnato e sostenuto durante questi tre anni di dottorato, ma mi sembra doveroso farlo. Il Professor Enrico Stalio, che è stato il mio tutor, merita un sentito ringraziamento. I suoi consigli, insegnamenti e la sua professionalità hanno contribuito in maniera importante alla mia crescita professionale ed umana. Un immenso grazie al Dottor Federico Brusiani, che è stato il mio tutor aziendale. E' stata la persona che più di tutte ha creduto in me: mi ha dato l'opportunità di imparare, di sbagliare, di mettermi in discussione quotidianamente in un ambiente competitivo come quello della Ferrari. La sua guida è stata preziosa per la mia crescita. Oltre a Federico, devo ringraziare gli altri Ferraristi: Marco Colapietro, la sua competenza, esperienza ed i suoi consigli hanno giocato un ruolo importante per me in questi tre anni (Marco, appena posso ti faccio il bonifico). Devo ringraziare inoltre Thierry Baritaud, Pete May, Marco Sibilio, Andrea Fogliani, Maurizio Tranchero, Francesco Cassarini, Matteo Ermini (che ha preso il mio posto) e tanti altri che hanno contribuito a rendere davvero speciale questo percorso. E' doveroso dedicare due parole anche alla mia famiglia, un infinito grazie va a mia madre e a mio padre per avermi sostenuto in maniera incondizionata dal giorno in cui sono nato. E' grazie ai vostri insegnamenti, sacrifici e incoraggiamenti se ho potuto inseguire i miei sogni. Devo ringraziare mio fratello Raffaele che per me è stato sempre presente, una figura solida ed un punto di riferimento. Grazie a mio fratello Manuel, per le sua curiosità, la sua leggerezza e il suo modo di essere ed esserci. Grazie ai tanti amici di una vita che mi hanno dato la giusta dose di energia in questo percorso così importante. Grazie all'associazione Don Chisciotte per tutto quello che mi ha dato. Grazie al Teatro Nero per avermi aiutato a comprendere me stesso.

Sintesi

Negli ultimi anni, i veicoli a trazione ibrida si stanno diffondendo in maniera sempre più estesa, rendendo più forte l'interesse dei ricercatori. Con ciò, componenti come Motori Elettrici, Batterie, e Convertitori di Potenza sono stati interessati da significative innovazioni. Il presente lavoro di tesi di dottorato si focalizza principalmente sui convertitori di potenza, il cui scopo è quello di garantire la conversione di potenza da Corrente Alternata in Corrente Continua, e viceversa, per mezzo di semiconduttori come IGBT, DIODI e MOSFET. Nonostante i convertitori di potenza raggiungano tipicamente efficienze superiori al 90%, essi possono essere interessati da flussi termici nell'ordine di centinaia di W/cm^2.

Lo scopo principale di questa tesi di dottorato è quello di eseguire un'analisi termica dettagliata sui sistemi di conversione di potenza.

E' stato sviluppato un tool di simulazione in grado di effettuare simulazioni di tipo elettro-termico (Banco Prova Virtuale). Questo strumento è in grado di valutare qualsiasi topologia di convertitore di potenza considerando un ampio range di condizioni operative. Inoltre, un elevato numero di moduli di potenza può essere esaminato con una potenza di calcolo limitata e bypassando test sperimentali. Tale strumento è in grado di identificare e scartare le configurazioni che presentano una bassa efficienza. In questo modo è possibile focalizzarsi solo sulle soluzioni più promettenti. In questo lavoro, il tool di simulazione è stato accuratamente validato con dati sperimentali e risultati di letteratura. Successivamente, è stata condotta una larga campagna di simulazione su diverse configurazioni di convertitori di potenza. Le prestazioni di tali dispositivi sono state valutate attraverso un accurato calcolo delle dissipazioni sia in condizioni stazionarie che dinamiche. Inoltre, è stato descritto in maniera dettagliata il comportamento dei signoli semiconduttori di potenza.

Per garantire prestazioni e affidabilità di tali dispositivi è necessario lo studio di un sistema di raffreddamento. Ci si è concentrati su una strategia di cooling a getti sommersi. Tutto lo studio è stato svolto con un approccio 3D-CFD. Inizialmente, la metodologia di calcolo è stata effettuata su una geometria semplificata che includeva un singolo getto, i cui risultati sono stati confrontati con un caso test sperimentale,

ottenendo un'ottima correlazione. Di conseguenza, la metodologia di calcolo è stata adottata per effettuare un dettagliato studio parametrico. E' stato valutato nel dettaglio l'effetto del diametro, dell'aspect ratio, della disposizione e del numero degli ugelli.

L'attività di ricerca ha permesso di comprendere in dettaglio il comportamento dei convertitori di potenza dal punto di vista elettro-termico. La progettazione dei convertitori di potenza può essere fortemente supportata dal Banco Prova Virtuale sviluppato, infatti l'individuazione della migliore configurazione dei moduli di potenza è veloce ed accurata. I getti sommersi rappresentano un approccio di raffreddamento efficiente e flessibile per i semiconduttori e la potenza di pompaggio in gioco è piuttosto bassa.

Abstract

Over the last years, hybrid electric vehicles are becoming increasingly widespread attracting the interest of researchers in this field. Significant innovations have been recently achieved about components like electrical machines, energy storages, and power converters. Focusing on power converter, its function is to ensure the energy conversion from alternating current to direct current sides, and vice versa, by using power semiconductors as IGBTs, DIODEs, and MOSFETs. Despite power electronic devices are usually characterized by efficiencies over 90%, they can be characterized by heat flux densities in the order of hundreds of W/cm^2.

The main purpose of the present PhD thesis is to perform a detailed thermal analysis on power conversion systems.

An electro-thermal simulation tool (Virtual Test Bench) which can address the power converter design is developed and presented. The tool allows to evaluate any multilevel power converter topologies by covering a wide range of possible operating conditions. Moreover, many power module technologies can be evaluated at low computational cost and by avoiding costly laboratory tests. The proposed tool enables the anticipated identification of designs to be rejected because of their low efficiency. Therefore, the experimental efforts can be only focused on the most promising solutions. In the present work, the simulation tool is successfully validated against experiments and literature results. A large simulation campaign is then conducted by considering a number of power converter configurations. Their performance are evaluated by means an accurate power losses computation in both steady-state and time-dependent conditions. In addition, the behavior of single semiconductors equipping the power converter is detailedly investigated.

Performance and reliability of such devices are ensured by means a dedicated cooling system. In the current work, only active cooling systems are taken into account. In detail, the focus is on design and application of submerged impinging jet cooling technique. A 3D-CFD simulation approach is adopted. The simulation methodology is firstly applied on a simplified geometry made by a single jet. For this geometry, results are compared to experimental test case obtaining a good overall correlation. Then, the

validated 3D-CFD methodology is adopted to complete a detailed parametric study of jet cooling solution applied in power converters. The effect of nozzle diameter, aspect ratio, arrangement, and number of jets are accurately investigated.

The research activity allows to understand in detail the power converter behavior from a thermal point of view. The power converter design process can be strongly supported by the developed Virtual Test Bench, in fact the individuation of the best power module configuration is fast and accurate. Moreover, the tool can be furthermore developed to allow a multi-objective optimization of power converter. Finally, submerged impinging jets represent an efficient and flexible cooling approach for semiconductors with low pumping power level.

Contents

Nomenclature

Acronyms

DoD	Depth of Discharge
OCV	Open Cell Voltage
SoC	State of Charge
2L	2-Level
3L	3-Level
AC	Alternating Current
AR	Aspect Ratio
BJT	Bipolar Junction Transistor
BJTs	Bipolar Junction Transistors
CFD	Computational Fluid Dynamics
DC	Direct Current
DoH	Degree of Hybridization
EM	Electrical Machine
EMs	Electrical Machines
ERS	Energy Recovery System
ES	Energy Storage
ESs	Energy Storages

EV Electric Vehicle

FW Field-Weakening

GDB Gate Drive Board

HEV Hybrid Electric Vehicle

HEVs Hybrid Electric Vehicles

ICE Internal Combustion Engine

IGBT Insulated-Gate Bipolar Transistor

IGBTs Insulated-Gate Bipolar Transistors

MGU Motor Generator Unit

MOSFET Metal-Oxide-Semiconductor Field-Effect Transistor

MOSFETs Metal-Oxide-Semiconductor Field-Effect Transistors

MTPA Maximum Torque Per Ampere

NPC Neutral-Point Clamped

PC Power Converter

PCs Power Converters

PMSM Permanent Magnet Synchronous Motor

PMSMs Permanent Magnet Synchronous Motors

PWM Pulse Width Modulation

RANS Reynolds Averaged Navier-Stokes

RMS Root Mean Square

SiC Silicon Carbide

SPWM Sinusoidal Pulse Width Modulation

SVM Space Vector Modulation

TNPC T-type Neutral-Point Clamped

Greek Symbols

α	length of vector ψ
β	length of vector δ
Δp	Pressure drop
δ	Discretisation vector of n_{MGU}
η	Power converter efficiency
η_c, η_d	Charge and discharge battery efficiency
γ	Puekert's constant
ω	Electrical angular speed
ω_B	Maximum motor angular speed
ω_m	Motor angular speed
ϕ	Concatenated magnetic flux
ϕ_m	Flux provided from the permanent magnets
ϕ_{PM}	Permanent magnet flux linkage
ψ	Discretisation vector of T_{MGU}
ρ	density
τ	Time constant
Θ	Period
θ	Electrical angular position
φ	Current phase angle

Roman Symbols

$[A_w]$	Average temperature at the interface
$\bar{h}$	Overall heat transfer coefficient
$\bar{I}$	Electric current vector

$\dot{Q}$	Heat
$\dot{q}$	Heat flux
$\dot{V}$	Volumetric flow rate
$\hat{I}$	Peak current
A_n	Nozzle area
A_{chip}	Chip area
C	Capacitance
c	Specific heat
C_d	Discharge coefficient
C_{el}	Electrical capacity
d_n	Nozzle diameter
E_m	Magnetic energy
E_{off}	Deactivation switching energy
E_{on}	Activation switching energy
E_{rr}	Reverse recovery switching energy
f_m	Frequency of the reference signal
f_{sw}	Switching frequency
H	Jet-to-target distance
h	Local heat transfer coefficient
H_d	Heat flux density
I	Electric current
I_c	Electric current flowing through the semiconductor circuit
L	Nozzle length
l	Length

L_i i phase auto inductance

M Modulation index

M_{ij} Mutual inductance between i and j phases

N Nozzle number

n_{MGU} MGU speed

NF Number of phases

P Electrical Power

P_0 Heat generation of the chip

P_p Pumping power

P_{el} Electrical power

P_{ICE} Power deliverable from an ICE

P_{Joule} Joule dissipation

P_{mecc} Mechanical power

P_{MGU} Power deliverable from an MGU

P_a Active power

$P_{c,DIODE}$ DIODE conduction losses

$P_{c,IGBT}$ IGBT conduction losses

$P_{c,MOSFET}$ MOSFET conduction losses

$P_{c,X1X2}$ Conduction losses of the chip X1 or X2

$P_{d,cycle}$ Power converter losses over the dynamic cycle

P_d Power converter losses

P_{ij} Power converter losses at i-th and j-th position

P_r Reactive power

$P_{sw,X1X2}$ Switching losses of the chip X1 or X2

pp	pole pairs number
R	Resistance
r	Radial distance from the center of nozzle to the exhaust region
R'_{ref}	Reference thermal resistance per unit area
R'_{al}	Aluminum thermal resistance unit area
R'_{ce}	Ceramic thermal resistance unit area
R'_{co}	Copper thermal resistance unit area
r_f	DIODE forward resistance
R_s	Stator resistance
R_{fillet}	Fillet radius
r_{ce}	IGBT collector emitter resistance
$r_{DS,on}$	MOSFET drain-source resistance
$S_{\min}, S_{\max}$	Ellipse minor and major semi-axes
t	time
T, T_j	Chip or junction temperature
$T_{b,\text{in}}$	Fluid bulk temperature at the inlet
T_{in}	Fluid inlet temperature
T_{MGU}	MGU Torque
u	Velocity
U_{ij}	Usage time
V	Voltage
V_Δ	Triangular carrier voltage signal
V_f	DIODE forward saturation voltage
V_m	Sinusoidal reference voltage signal

V_{ce0} IGBT collector emitter saturation voltage at $I_c = 0$A

V_{ce} IGBT collector emitter saturation voltage

$V_{dc,f}$ Bus DC voltage corresponding to the concatenated stator value

V_{dc} Bus DC voltage

V_{f0} DIODE forward saturation voltage at $I_c = 0$A

Y Ratio between f_{sw} and f_m

y_+ Dimensionless wall distance

Z Impedance

$\mathbf{T}$ Torque

Superscripts

$*$ Dimensionless

$\mathbf{T}$ Transpose

Subscripts

a, b, c phases

d along the direct axes of the Park's domain, dissipation

i i-th position

j j-th position

k k-th position

q along the quadrature axes of the Park's domain

avg average

eff effective

el electrical

max maximum

min minimum

nom	nominal
ref	reference condition
th	thermal

Chapter 1

Introduction

1.1 Background

Worldwide climate variations are partly to be ascribed to the exhaust emissions from thermal engines [1]. This has prompted governments to enact stringent emission regulations, forcing car manufacturers in investing to comply the requirements. Over the last years, *Hybrid Electric Vehicles* (HEVs) are becoming increasingly widespread attracting the interest of researchers in this field. HEVs are usually classified on the basis of their architecture [1, 2] or on the degree of hybridization [3]. In HEVs, the traction system is based on the combined adoption of an *Internal Combustion Engine* (ICE) and an *Energy Recovery System* (ERS) made by one or more *Motor Generator Unit* (MGU), an *Energy Storage* (ES), and a *Power Converter* (PC) to link ES and MGU components. These devices can be combined in a different way to achieve different goals such as improved fuel economy, increased power, additional auxiliary power for electronic devices or high performance. Moreover, also different power deployment strategies can be easily implemented in order to help the system to achieve the desired purpose. In general, the power management of the system is entrusted to PC which can be defined as the brain of the whole system. Different typologies of *Power Converters* (PCs) are employed in the industrial field, however, the current study is only focused on the device capable of converting *Direct Current* (DC) power to *Alternating Current* (AC) power and vice versa.

1.2 Context

Nowadays, hybrid solutions are massively taking place in the automotive field: from city-car to super-car. Moreover, hybrid electric vehicles are also taking place in the motorsport framework such as in Formula 1[4]. The present PhD research activity has been performed in partnership with Ferrari S.p.A. In detail, the work has been conducted at the Energy Recovery System Department of Ferrari Gestione Sportiva (Motorsport division). This Department is in charge of developing the ERS system of the Ferrari Formula 1 car. Its architecture is quite complex and a clear description can be found on the Formula 1 website [4].

1.3 Motivations and Purpose

The aim of the present research study is to perform a wide thermal analysis on power conversion systems.

Over the years, a large number of studies focused on PC performance evaluation. Several methods can be found in literature to evaluate PC losses. Experimental tests do not allow a fast investigation and in the preliminary design phase only the total PC losses can be obtained [5]. In general, analytical models are usually adopted to overcome these limitations. For example, in Ref. [6], the power losses are described through polynomial formulations. The computation of losses is very accurate, but the methodology could be complicate to be used in simulation tools. Also in Refs. [7, 8], the implemented schemes are accurate, however the losses calculation requires some computational efforts. In Ref. [9], PC losses prediction are affected by low accuracy when extending the operating conditions range in terms of current and/or voltage.

To overcome these limitations, an electro-thermal simulation tool (which is called "Virtual Test Bench") is developed and presented in order to address the design of power converters. This tool represents a viable way to evaluate power converter systems at limited computational expenses. Any converter configuration can be easily investigated over a wide operational range. The power module characteristics are detailedly represented by look-up tables extracted from datasheet diagrams. The presented tool enables the anticipated identification of designs to be rejected because of their low efficiency and suggests the designs characterized by the low dissipation levels. In this way, only the most promising solutions are selected to be subjected to an experimentation campaign. In detail the global performance evaluation of power converter can be performed both in steady-state and time-dependent conditions. In

addition, a local investigation on power semiconductors helps the designers in the understanding of the heat flux density involved. This is very important for the choice and the study of the cooling system equipping the power module.

Power electronics devices can be cooled by different strategies such as pin fins, mini-channels and impinging jets heat exchangers. Pin fins heat exchangers are massively used in power electronics applications. As reported in Ref. [10], the main advantages of this cooling strategy are given by high wetted surface, low pressure loss and simple geometry. Unfortunately, one of the most important limitation can be due to the encumbrance. Moreover, this cooling strategy do not allow to an optimal distribution of the coolant flow rate on the heat source location. This is an important aspect in power electronics field, since power semiconductors can be distributed onto an electronic board in an irregular arrangement. Different mini-channel heat exchangers are developed over the years. In refs. [11, 12], parallel mini-channels are studied and an high heat transfer coefficient is found since the wetted surface involved is large. However a large pressure drop is ascertained for the specific applications. Also fractal channels, studied in Refs. [13–17], show limitations in terms of pressure drop and geometrical complexity. For this kind of applications, a multi-objective optimization procedure can be taken into account to found the best trade-off among thermal performance, pressure drop and geometrical complexity. In general, mini channels have a good potential but their performance can strongly depend on the specific application. Therefore, arrays of impinging jets might be a promising solution because they efficiently exchange high amounts of heat at an affordable pumping power level [18]. They can be easily used to cool specific hot spot. In this work, arrays of submerged impinging jets are considered.

1.4 Methodologies and Investigations

In the first part of this work, the Virtual Test Bench is used to perform a large simulation campaign. Both *2-Level* (2L) and *3-Level* (3L) PC topologies are considered. Besides the two different topologies, also different devices technologies are examined like Si IGBTs and SiC MOSFETs [19]. In detail, for 2L PC configuration, Infineon IGBT3 [20], Infineon EDT2 [21], and ROHM SiC MOSFET [22] are considered while 3L PC configuration is equipped with Semikron IGBT3 [23]. Prior to the numerical study, the tool is successfully validated against experimental tests and literature results reported in Ref. [6]. The PC input conditions are defined by: MGU torque demand (T_{MGU}), MGU angular speed (n_{MGU}), bus DC voltage (V_{dc}), and PC switching frequency (f_{sw}). Each configuration is investigated over a large steady-state simulation matrix including

260 points and over two drive cycles. PC losses are computed and the operating conditions sensitivity is assessed. The evaluation of the losses and Usage time maps allow to obtain a detailed analysis of the PC behavior through the drive cycles.

This analysis has also allowed to ascertain that power dissipation level which affects power semiconductors are in the order of hundreds of W/cm^2. In the last years, heat removal from power electronic devices is gaining a fundamental importance in many industrial fields, including hybrid traction systems. To tackle this technical problem dedicated cooling systems need to be adopted. Impinging jet cooling technique are becoming quite used in power electronics field. They might be a promising solution because they efficiently exchange high amounts of heat at limited pressure drop level [18]. In this study, array of submerged impinging jets are taken into account. Therefore, the second step of the current research activity is to investigate in detail the thermal behavior of power semiconductor by 3D-*Computational Fluid Dynamics* (CFD) approach. Impinging jet cooling strategies are evaluated by performing conjugated heat transfer simulations. Simulations are performed on a simplified computational domain which involves a single and rectangular chip (representing the heat source) separated from the coolant by a multi-material solid stack. The adopted numerical procedure is validated against experimental data, provided by refs.[24][25]. A detailed parametric study is successively performed and results are compared and discussed in order to obtain the best compromise in terms of cooling efficiency and pumping power required by the feed system. Three nozzle diameters are considered, associated with two different aspect ratios of 1 and 0.5 respectively. Both inline and staggered arrangements are adopted and an increase of nozzles number are taken into account. Heat generation rate of the chip and inlet temperature of the coolant is the same for all the simulated configurations. Moreover, each simulation is performed under a given pressure drop, this is done in view of numerical considerations and following the suggestions reported in Refs. [26][27] and it represents a practical problem, very close to electric traction applications. As compared to more classical solutions, submerged impinging jets represent an efficient technique for the cooling of power electronics. Heat is exchanged also at low pumping power levels. Array of jets are flexible in terms of geometry and can be specifically designed to control temperatures in critical spots.

1.5 Thesis outline

The PhD thesis is arranged as follows:

- Chapter 2 shows a short description of the main *Hybrid Electric Vehicle* (HEV) architectures;
- Chapter 3 shows a description of an energy storage and its basic equations;
- Chapter 4 proposes the basics of a brushless motor, moreover a mathematical description is provided;
- Chapter 5 presents a wide overview of power converters. Moreover, an analytical description of power semiconductors from a thermal point of view is shown;
- Chapter 6 presents the developed electro-thermal simulation tool (Virtual Test Bench). In detail, a literature review on similar topics is firstly provided. Successively, the developed tool validation is presented. Then, a large simulation campaign is performed on four power modules selected. The power converters behavior is investigated by considering a wide range of operating conditions;
- Chapter 7 presents the impinging jets cooling technique for power electronics. After a wide evaluation of the state of the art, a 3D-CFD investigation is performed on single heat source. A deep parametric analysis is proposed and results are summarized in terms of heat transfer effectiveness and pumping power efficiency;
- Chapter 8 shows the conclusions of the presented work.

1.6 Publications

The research presented here are published in:

- *"Comparison between cooling strategies for power electronic devices: fractal minichannels and arrays of impinging submerged jets"*. The work has been presented at the *" 36th UIT Heat Transfer Conference 25-27 June 2018, Catania, Italy"*. On 20th May 2019, the paper has been published on *"Journal of Physics: Conference Series"* [13].
- *"Numerical study of submerged impinging jets for power electronics cooling"*. The paper has been published on *"International Journal of Heat and Mass Transfer"* in October 2019 [18].
- A paper titled: *"A Virtual Test Bench Oriented to Power Module Evaluation"* has been submitted to the Journal *"IEEE Transactions on Power Electronics"*

.

Chapter 2

Hybrid Electric Vehicles

2.1 Overview

Nowadays, the huge amount of oil and gas usage in the world leads to problems like global warming and pollution. In fact, the emission regulations are getting even more stringent and automotive manufacturers are spending many resources to accomplish the requirements. The challenge is to obtain solutions which can be economically and environmentally sustainable. Significant innovations are introduced to face this challenge. As reported by [28–30], the main developed solutions are given by: turbocharges, engine downsize strategy, valve timing variation or cylinders deactivation. These developments allowed to improve fuel efficiency. Moreover, catalytic converters or exhaust gas recirculation allowed to reduce the Nox emission. Despite these innovations, automotive manufacturers needed to focus their efforts on more drastic solutions to accomplish the emission legislation. Therefore, HEVs are taking even more place in the automotive propulsion framework; from city-car to motorsport. Classification and description of HEVs are well explained by Cardoso et al., Prajapati et al. and Govardhan [1–3]. Here, a summary is proposed in order to show a clear HEV description. HEVs combine the benefits of both ICE and *Electric Machine* (EM). An HEV is able to exploit the high-efficiency of EM (MGU) and to recover energy from a brake operations. The connection between the ICE and the EM allows to take advantages of both while minimizing their weakness. For example, an electrical machine is characterized by a much faster dynamic response with respect to an ICE to develop power. Some of the advantages of the electric motors are found in high torque density, robustness and reduced weight. Moreover, an electrical machine can be used both as motor and as generator. Indeed, as mentioned before, an HEV is capable of braking through its electrical motor and recovery energy which would have been wasted

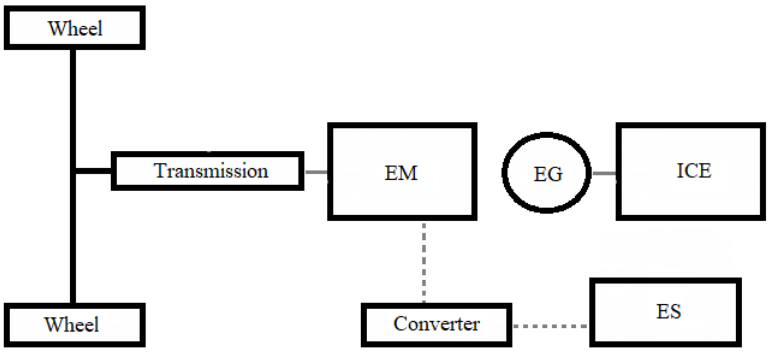

Figure 2.1 Schematic representation of series HEV architecture

by means the brakes. Moreover, an MGU transforms electrical energy into mechanical one with an higher efficiency than the one achieved by a ICE. Finally, an HEV can develop torque with both the engines. Power deployment of an HEV depends by its powertrain architecture. It can be configured to achieve different target such as fuel consumption reduction, increased power or improvement of performance.

2.2 HEVs Classification

An HEV can be basically classified on the basis of its architecture as reported in [1, 2].

2.2.1 Series Hybrid

The ICE is placed in series with an electric generator, producing electric power to drive one or more electric motors. The latter delivers the traction power to the wheels. The excess power is then stored in the energy storage. This architecture does not allow direct mechanical link between the thermal engine and the vehicle wheels. Consequently, the ICE can be controlled independently from the vehicle power requirement and close to its maximum performance condition. Hence, series HEVs tend to have high efficiency engine working condition. This benefit is quickly outweighed by the fact that they often require very powerful and expensive energy storage. The ES is needed because in most cases, the motor may have to produce 50% of the required total power demand [1]. Moreover, the energy provided from the ICE is converted twice before to drive the wheels, As a matter of fact, this lead to undesired energy dissipation. For these reasons, the system is more expensive and complex than the parallel one. In Fig 2.1, a schematic representation is proposed.

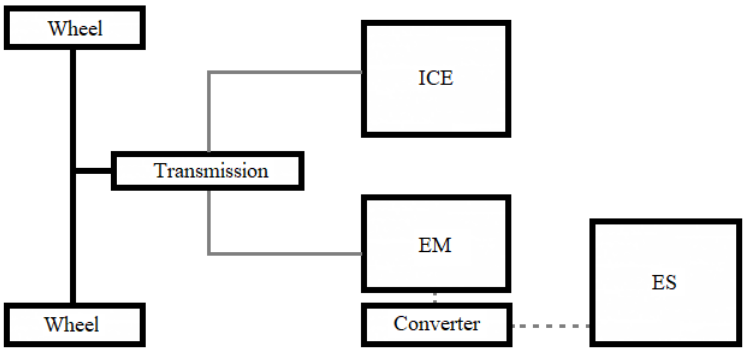

Figure 2.2 Schematic representation of parallel HEV architecture

2.2.2 Parallel Hybrid

As found by Cardoso et al. [2]. On the parallel HEV architecture, both thermal engine and electrical machine can work independently or together to provide torque to the wheels. In this arrangement, the ICE is mechanically coupled to the transmission, while the EM is in charge of helping the ICE during boost event. Depending on the power of the EM, it can be also used as the vehicle's unique source of power at idle and during the starts [2]. The possibility to have direct energy flow from the ICE to the wheels allows the parallel HEV to shift to the most efficient point of operation using the thermal engine. This is allowed by means the parallel connection between the electric machine and the thermal engine, which implies that the capabilities of the ICE and the EM can be changed without modifying vehicle's total driving capacity. In Fig. 2.2, a schematic representation is reported.

2.2.3 Parallel-Series Hybrid

As reported by Cardoso et al. [2], two electric machines are required. One works as generator and the other works as motor. The connection between the generator and the thermal engine is done using a planetary energy splitting device. This device allows the vehicle to operate both as parallel and series HEVs. The series–parallel architecture offers the advantage to have the ICE decoupled from the vehicle transmission, thus making it possible for the vehicle to be driven using only the electric motors. This also allows the ICE to works around its maximum efficiency conditions. In Fig. 2.3, a schematic representation is shown.

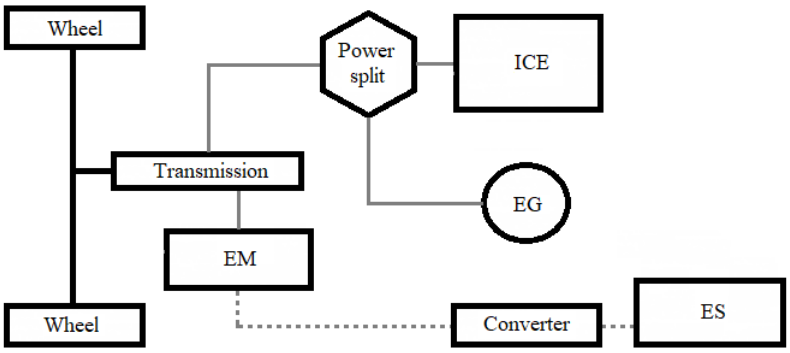

Figure 2.3 Schematic representation of parallel-series HEV architecture

2.3 Degree of Hybridization

As reported by Govardhan [3], HEVs can be classified on the basis of the degree of Hybridization. It depends on the power exhibited by the ICE and the MGU. In detail, in a HEV: the ratio between the power produced by the MGU and the total power delivered by the vehicle is defined as *Degree of Hybridization* (DoH). Its mathematical description is given by the following equation:

$$\text{DoH} = \frac{P_{\text{MGU}}}{P_{\text{MGU}} + P_{\text{ICE}}} 100 \tag{2.1}$$

where P_{MGU} is the power deployed by the electrical machine while P_{ICE} is power developed by the thermal engine. In [3], the HEVs classification on the basis of DoH is reported as follows:

- if DoH $< 5\%$ the HEV is called Micro-Hybrid. The electrical machine works to start or stop the system to automatically shut off the engine while idling. Moreover, the electrical machine is not able to provide additional torque to the vehicle;
- if DoH up to 10% is vehicle is called Mild-Hybrid. The electric machine is capable of providing the 10% of the maximum power of the thermal engine. With respect the previous case, the electrical machine is able to produce additional torque to the wheels;
- if $10\% <$ DoH $< 75\%$ we are facing with Full-Hybrid vehicles. Here, the different architectures described in the previous paragraphs can be found. Therefore, the mentioned advantages can be achieved;

- if DoH = 100% the vehicle is pure electric, no thermal engine is employed.

An HEV is equipped by components such as electric machine, internal combustion engine and energy storage. To ensure an appropriate power flow among these devices, a power management system is required. This task is ensured by the power converter which can be defined as the "brain" of the whole electrical system. In the following sections, a description of the main devices which compose an hybrid system is provided with a particular focus on the power converter.

Chapter 3

Energy Storage

3.1 Overview

The Energy Storage represents the system able to store and to supply electrical energy from/to electrical machines. Every HEV is equipped by an energy storage system and the most common is given by a battery. It is a device which can convert the chemical energy directly into electrical energy through electrochemical processes. The energy storage power density is usually lower than fuel but they can be dimensioned either to store the maximum possible energy or to exchange maximum power or to achieve a trade-off between these two conditions. The battery operating conditions need to be controlled in order to avoid performance degradation. An important parameter which strongly affects the battery performance is the temperature, so an appropriate cooling system needs to be adopted. Moreover, the batteries are subjected to severe safety regulations and they must be treated carefully. In most applications, energy storages make use of Lithium-ion cells since they allow to obtain a good trade-off in terms of energy density, weight and cost. They can be arranged by considering a series or parallel connection. The main characteristics of a battery systems are given by:

- Electrical capacity (C_{el}): it is given by the product between the intensity current and the requested time able to completely discharge the energy storage. It is measured in $Ampere \cdot seconds$;
- Discharge rate (C_{el}/x): it represents the current able to totally discharge the battery in x seconds. The C_{el} can be expressed by the Peukert's law [31] as $C_{\text{el}} = I^{\gamma}t$ where I is the discharge current, t is the discharge time and γ is the Peukert's constant which is greater than 1;

- State of Charge (SoC): it represents the percentage of the residual energy stored in the battery. Its mathematical description is given by following equation:

$$SoC = \frac{C_{\text{el}} - \int_{t_0}^{t_1} I(t)dt}{C_{\text{el}}} \tag{3.1}$$

  With the SoC introduction, it is possible to define the Depth of Discharge (DoD) as $1 - SoC$;

- Specific energy which is the energy deliverable by the ES per unit mass or per unit volume;

- Voltage (V_{dc}): it is the voltage between the positive and the negative terminals;

- Resistance (R): due to the internal components and/or connections of the cell;

- Open Cell Voltage (OCV): it is the potential of the cell ascribable only to the cathod and anode materials. It changes with the value of the SoC;

- Charge/Discharge number of cycles. This parameter expresses the number of cycles which causes an appreciable C_{el} decay. Usually this number is evaluated when the C_{el} reduces till the 50% of its nominal value.

3.2 Basic principles

In order to understand the basic principles of an energy storage, a short description is proposed. In Fig. 3.1, a schematic representation of a cell is reported. This simple schematic does not include dynamic components as capacitance or inductances since transient phenomena are neglected at this stage. The voltage at the terminals is function of OCV and Resistance (R) due to the internal components and/or connections of the cell. As previously said, the OCV depends by the state of charge. In Fig. 3.2, a qualitative OCV dependency with SoC is shown. The link between the two parameters is non linear and this curve are tipically extracted by experimental way. In addition, the OCV curve is different among cells which belong to the same family since the cell characteristics are affected by production dispersion. The OCV characteristic is usually provided by the manufacturers. The voltage drop associated to the cell internal resistance is always present. It mainly depends by several factor. Some of them are given by the cell temperature and SoC. Moreover, when facing with an ES, two working directions are allowed: the charge and discharge phases. The cell resistance varies also

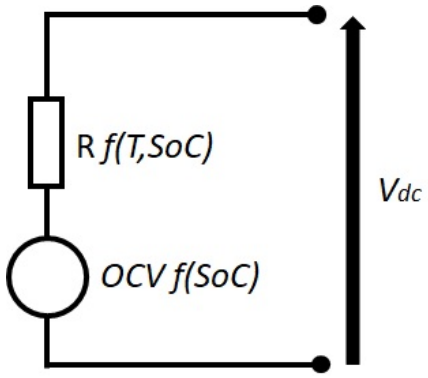

Figure 3.1 Schematic representation of a cell

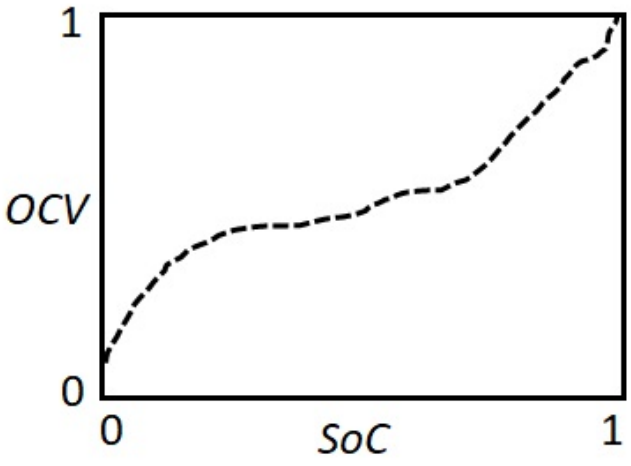

Figure 3.2 Open Cell Voltage as a function of the State of Charge

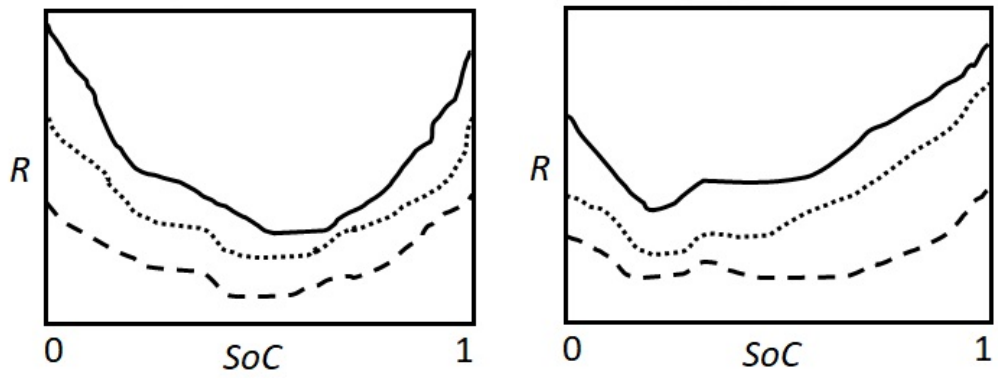

(a) Charge (b) Discharge

Figure 3.3 Open Cell Voltage as a function of State of Charge and temperature: T_1 continuous line, T_2 dotted line, T_3 dashed line ($T_1 < T_2 < T_3$)

by virtue the working direction. In Fig. 3.3, a qualitative representation of the cell resistance in charge and discharge conditions is shown. The cell temperature plays a crucial role. Basically, higher cell temperature is desired to limit the cell resistance and losses as well. However, battery cells are always characterized by a limit temperature which cannot be overcome to avoid high degradation or failure. Furthermore, the minimum cell resistance is basically detected with the SoC included between 0.4 and 0.6. Close the maximum and the minimum SoC, the ohmic dissipation tend to grow. The cell resistance characterization is obtained by experimental way. The voltage between the cell terminals can be expressed as:

$$V_{dc} = OCV - RI \tag{3.2}$$

where I is positive during discharge operations and negative for charge working conditions as well. The deliverable electrical power can thus be obtained as follow:

$$P_{\text{el}} = V_{dc}I = (OCV - RI)I \tag{3.3}$$

and equation 3.3 can be rewritten in the following formulation:

$$RI^2 - OCVI + P_{\text{el}} = 0 \tag{3.4}$$

the equation 3.3 has two solutions, hence two values of I can be assessed. However, only a solution has a physical meaning and it is represented by the following expression:

$$I = \frac{OCV - \sqrt{OCV^2 - 4RP_{\text{el}}}}{2R} \tag{3.5}$$

from equation 3.5, to obtain the maximum P_{el} deliverable, it must be evaluated by imposing the following condition:

$$OCV^2 - 4RP_{\text{el}} \geq 0 \Rightarrow P_{\text{el}} \leq \frac{OCV^2}{4R} = P_{\max} \tag{3.6}$$

it is clear as $P_{\max}$ is a function of the internal resistance and the cell state of charge. It is now possible to write also the current (I) and the voltage (V_{dc}) as a function of P_{max}. For I, it becomes:

$$I = \frac{OCV}{2R}\left(1 - \sqrt{1 - \frac{P_{\text{el}}}{P_{\max}}}\right) \tag{3.7}$$

in the same way, by combining equation 3.14 and 3.7, it can be obtained the V_{dc} expression:

$$V_{dc} = \frac{OCV}{2}\left(1 + \sqrt{1 - \frac{P_{\text{el}}}{P_{\max}}}\right) \tag{3.8}$$

finally, it is possible to calculate the Joule losses ascribable to the internal resistance of the cell. The Joule losses can be written as:

$$P_{\text{Joule}} = RI^2 = R\left[\frac{OCV}{2R}\left(1 - \sqrt{1 - \frac{P_{\text{el}}}{P_{\max}}}\right)\right]^2 = \frac{OCV^2}{4R}\left(1 - \sqrt{1 - \frac{P_{\text{el}}}{P_{\max}}}\right)^2 \tag{3.9}$$

as already said, the battery resistance changes with charge and discharge conditions. This means that two efficiency formulations can be written.

Charge condition

It this case, the current and P_{el} assume negative values which means that an external device delivers power to the battery. The general efficiency formulation is:

$$\eta_c = \frac{P_{\text{el}} + P_{\text{Joule}}}{P_{\text{el}}} \tag{3.10}$$

where P_{el} is the electrical power provided by the external load to the ES and P_{Joule} is the Joule dissipation due to the battery internal resistance. By using equations 3.3,

3.7 and 3.8, η_c becomes:

$$\eta_c = \frac{V_{dc}I + RI^2}{V_{dc}I} = 1 + \frac{1 - \sqrt{1 - \frac{P_{\text{el}}}{P_{\max}}}}{1 + \sqrt{1 - \frac{P_{\text{el}}}{P_{\max}}}} \tag{3.11}$$

For sake of simplicity, all mathematical steps are avoided and equation 3.11 assumes a more compact relationship:

$$\eta_c = \frac{2}{1 + \sqrt{1 - \frac{P_{\text{el}}}{P_{\max}}}} \tag{3.12}$$

If considering the maximum achievable power condition: $|P_{\text{el}}| = P_{\max}$ (in this case P_{el} is negative), the battery efficiency reaches a value above 0.8. If $|P_{\text{el}}|$ is lower than $P_{\max}$, the efficiency tends to noticeably increase.

Discharge condition

During the discharge phase, the current and P_{el} have a positive sign. The efficiency is equal to:

$$\eta_d = \frac{P_{\text{el}}}{P_{\text{el}} + P_{\text{Joule}}} = \frac{1 + \sqrt{1 - \frac{P_{\text{el}}}{P_{\max}}}}{2} \tag{3.13}$$

In this case, all mathematical passages are bypassed for sake of brevity. It can be affirmed that: for the maximum deliverable power $P_{\text{el}} = P_{\max}$, $\eta_d = 0.5$ which is a quite low value. Therefore, it is not suggested to design a battery system which can deploy the same power value of the coupled device.

The dynamic behavior

In the previous paragraph, dynamic elements are not treated since the basic battery principles are evaluated at steady-state conditions. In real applications, ES systems have a dynamic response which cannot be neglected for an accurate understanding. The most simple battery schematic is provided by Fig. 3.4. In this picture, a general description is reported and n resistance-capacitance stages are reported. This number depends by the battery characteristics. The voltage between the two terminals can be represented by the following equation:

$$V_{dc} = OCV - \left[R + R_1\left(1 - e^{t/\tau_1}\right) + ... + R_n\left(1 - e^{t/\tau_n}\right)\right]I \tag{3.14}$$

where τ_i is the the time constant of the i-th stage. It is equal to R_iC_i and C_i is the capacitance of the i-th stage. As a matter of fact, to compute the electrical power or

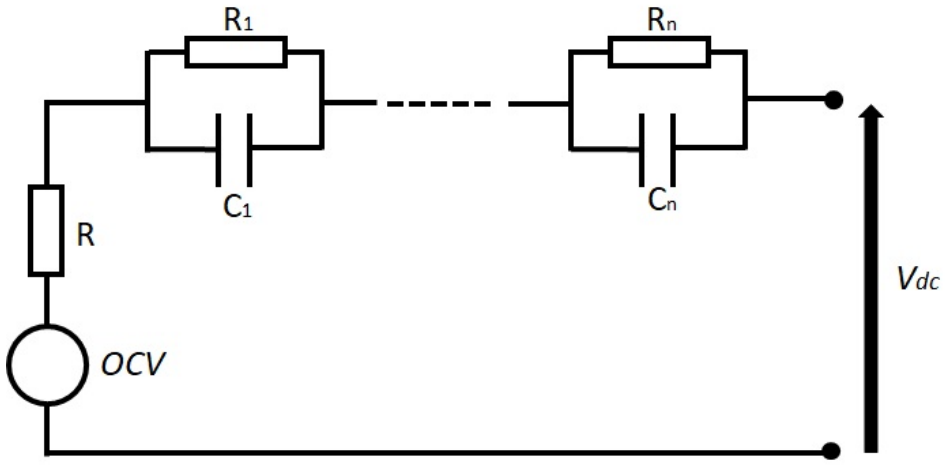

Figure 3.4 Schematic representation of a battery

Joule losses istantaneously, this formulation needs to be adopted. These parameters are usually evaluated by the manufacturers through a complex characterization process. Moreover, these parameters are usually mapped over the various operating conditions. Since this work is not focused on ES device only a basic description is provided, a detailed overview can by found in Ref. [32].

Chapter 4

Permanent Magnet Synchronous Motor

4.1 Overview

In this chapter, a basic description of *Permanent Magnet Synchronous Motors* (PMSMs) is reported. A full description can be found in [33–35]. The Permanent Magnet Synchronous Motors are widely employed in industrial application. The main components of this kind of machine are due by the stator which is the static part of the machine in charge of powering the device, and by the rotor which is the rotating component. The stator is interested by a rotating magnetic field and its amplitude depends by the applied voltage. The rotor is interested by a magnetic field constant in amplitude which depends by the magnet properties. These kind of motors are also named brushless since there are no brushes. This leads some advantages which can be summarized by low maintenance requested, low noise level and high power density. The power density of this electrical machine depends by the magnet properties and the pole pairs number. Brushless motors are synchronous since the frequency of the magnetic field has the same frequency of the electrical quantities feeding the device. The main weak point of these electrical devices is the cost. The main cost factor is given from the permanent magnet type used to generate the magnetic field. The rotor is usually made in Ferrites, Samarium-Cobalt or Neodymium-Iron-Boron materials [36]. Brushless motor can be also classified as isotropic and anisotropic. This is due to the magnetic reluctance developed inside the air gaps. When the magnetic reluctance is constant, the electrical machine is isotropic. The stator auto-inductances do not change with the rotor motion and position. The electrical machine is anisotropic if the magnetic field of

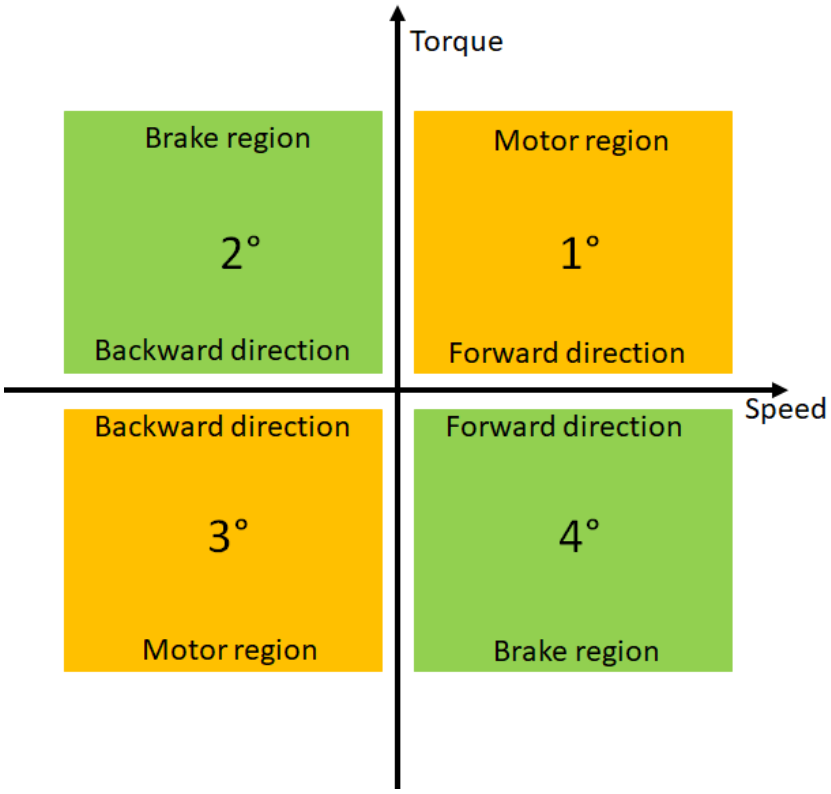

Figure 4.1 Operating quadrant of an electrical machine

the stator changes when the rotor moves and each winding sees a different reluctance value. Hence the stator auto-inductances depend by the rotor position.

The electric motor (EM or MGU) is the machine capable to transform the electrical energy provided from a given power source into the mechanical energy required to drive the shaft of the machine. The MGU can work in AC or DC. In the present work an AC MGU brushless is considered. An EM can be classified accordingly to its capability of working in the different quadrants of the rotor speed versus torque plane as shown in Fig. 4.1:

- In the first quadrant the EM works in forward direction, thus as a motor. Hence the power is transferred from the energy storage to the shaft;
- In the second quadrant, the motor works as generator in backward direction. So, torque and speed are opposite in sign and the power flows from the shaft to the energy storage;
- In the third quadrant the electric engine operates as a motor but in backward direction: power flows from the power source to the shaft;

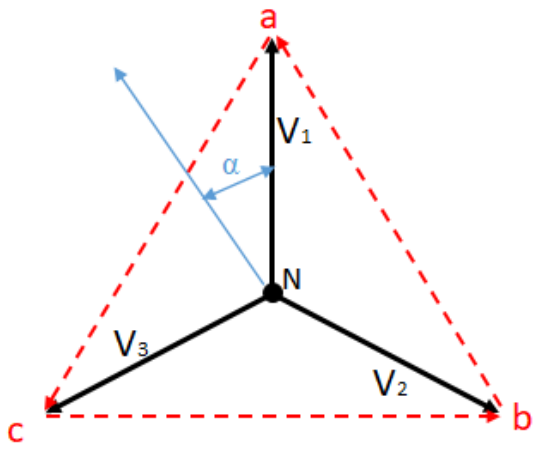

Figure 4.2 Schematic representation of three-phase voltage in star configuration

- Finally, in the fourth quadrant, the machine is braking in forward direction, therefore it operates as a generator. Hence, power flows again from the shaft to the ES.

The choice of the electrical drive depends on the desired goal. An HEV can work in the first and in the fourth quadrants, while a full electric vehicle must be equipped with a drive able to operate in every quadrants [37]. For the present case, the operating quadrants involved will be the first and the fourth.

4.2 Analytical model of a brushless motor

4.2.1 From battery DC voltage to three-phase AC voltage

For the present study, a three-phase machine in a star connection is considered. The Brushless motor is an AC machine, and it can work both as motor and generator. A device which is in charge to provide (store) the power to (from) the electrical machine is requested. It can be a battery which operates in DC power. To link the three-phase AC machine and DC battery a AC/DC three-phase power converter is required. In Fig. 4.2, a star connection is represented, each phase is switched of $2/3\pi$. Basically, the values of phase-to-phase voltages must be computed with respect to the DC electric potential V_{dc} as follows:

$$V_{dc} = V_{ab} = V_1 cos\frac{\pi}{6} + V_2 cos\frac{\pi}{6} \tag{4.1}$$

which means that:

$$V_1 = V_2 = V_3 = V \Rightarrow V_{dc} = 2V cos\frac{\pi}{6} \Rightarrow V = \frac{V_{dc}}{\sqrt{3}} \tag{4.2}$$

4.2.2 Electrical model

Here, the analytical description of a brushless motor is presented. A more complete overview is reported in the following references [37, 33–35]. A brushless motor operates by means the interaction between the stator rotating magnetic field and the rotor magnetic field. The model is described just for the stator since the rotor has no excitation circuit:

$$V_a(t) = R_s I_a + \frac{\partial \phi_a}{\partial t} \tag{4.3}$$

$$V_b(t) = R_s I_b + \frac{\partial \phi_b}{\partial t} \tag{4.4}$$

$$V_c(t) = R_s I_c + \frac{\partial \phi_c}{\partial t} \tag{4.5}$$

Where:

- R_s is the stator resistance;
- ϕ_i is the concatenated flux for $i = a, b, c$;
- V_i is the stator voltage for $i = a, b, c$;
- I_i is the stator current for $i = a, b, c$.

The concatenated magnetic fluxes can be expressed as a function of inductances and permanent magnet fluxes as shown in the following equations:

$$\phi_a = L_a(\omega t)I_a + M_{ab}(\omega t)I_b + M_{ac}(\omega t)I_c + \phi_{ma}(\omega t) \tag{4.6}$$

$$\phi_b = L_b(\omega t)I_b + M_{ba}(\omega t)I_a + M_{bc}(\omega t)I_c + \phi_{mb}(\omega t) \tag{4.7}$$

$$\phi_c = L_c(\omega t)I_c + M_{ca}(\omega t)I_a + M_{cb}(\omega t)I_b + \phi_{mc}(\omega t) \tag{4.8}$$

where:

- ωt is the rotor electrical angular position and it is indicated by θ;
- M_{ij} is the mutual inductance between phases i and j;
- L_i is the $i - phase$ auto-inductance;

- ϕ_{mi} is the magnetic flux produced by the magnet on the $i - phase$.

these equation can be now rewritten in a matrix form:

$$\begin{bmatrix} V_a \\ V_b \\ V_c \end{bmatrix} = \begin{bmatrix} R_s & 0 & 0 \\ 0 & R_s & 0 \\ 0 & 0 & R_s \end{bmatrix} \begin{bmatrix} I_a \\ I_b \\ I_c \end{bmatrix} +$$
$$+\frac{\partial}{\partial t}\left(\begin{bmatrix} L_a(\theta) & M_{ab}(\theta) & M_{ac}(\theta) \\ M_{ba}(\theta) & L_b(\theta) & M_{bc}(\theta) \\ M_{ca}(\theta) & M_{cb}(\theta) & L_c(\theta) \end{bmatrix} \begin{bmatrix} I_a \\ I_b \\ I_c \end{bmatrix} + \begin{bmatrix} \phi_{ma}(\theta) \\ \phi_{mb}(\theta) \\ \phi_{mc}(\theta) \end{bmatrix} \right)$$

in a more compact way, the same equation becomes:

$$\mathbf{V_s} = \mathbf{R_s I_s} + \frac{\partial}{\partial \mathbf{t}}\Big(\mathbf{L}(\theta)\mathbf{I_s}\Big) + \frac{\partial \phi_{\mathbf{m}}(\theta)}{\partial \mathbf{t}} \tag{4.9}$$

and:

$$\mathbf{V_s} = \mathbf{R_s I_s} + \frac{\partial \mathbf{L}(\theta)}{\partial \theta}\frac{\partial \theta}{\partial \mathbf{t}}\mathbf{I_s} + \mathbf{L}(\theta)\frac{\partial \mathbf{I_s}}{\partial \mathbf{t}} + \frac{\partial \phi_{\mathbf{m}}(\theta)}{\partial \mathbf{t}} \tag{4.10}$$

and if the stator currents are equal to 0A:

$$\mathbf{V_s} = \frac{\partial \phi_{\mathbf{m}}(\theta)}{\partial \mathbf{t}} \tag{4.11}$$

it represents the back-electromotive-force (back e.m.f.) developed on the stator circuit by the rotor which is rotating at an electrical angular speed $\omega = \partial\theta/\partial t$. The torque equation can be obtained by writing a power balance equation:

$$\mathbf{I_s^T V_s} = \underbrace{I_s^T R_s I_s}_{\text{A}} + \underbrace{I_s^T \frac{\partial L(\theta)}{\partial \theta}\omega I_s + I_s^T L(\theta)\frac{\partial I_s}{\partial t} + I_s^T \frac{\partial \phi_m(\theta)}{\partial t}}_{\text{B}} \tag{4.12}$$

the left side of the equation represents the instantaneous power provided by the power supply. For the right side, the term A represents the Joule losses. The term B represents the sum of mechanical power (P_{mecc}) provided to the load and the magnetic energy variation ($\frac{dE_m}{dt}$). It is demonstrated that [35]:

$$\frac{\mathbf{dE_m}}{\mathbf{dt}} = \frac{1}{2}\left(2I_s^T L(\theta)\frac{\partial I_s}{\partial t} + I_s^T \frac{\partial L(\theta)}{\partial \theta}\omega I_s\right) \tag{4.13}$$

by subtracting the equation 4.13 to the B term of the equation 4.12, the mechanical power can be written as:

$$\mathbf{P_{mecc}} = \frac{1}{2} I_s^T \frac{\partial}{\partial \theta} L(\theta) \omega I_s + I_s^T \frac{d\phi_m(\theta)}{dt} \omega \tag{4.14}$$

where ω is the electrical angular speed, and it can be related to the rotor mechanical speed as:

$$\omega_m = \frac{\omega}{pp} \tag{4.15}$$

where pp are the number of magnetic pole pairs. Now the torque can be expressed as:

$$\mathbf{T} = pp \left(\underbrace{\frac{1}{2} I_s^T \frac{\partial}{\partial \theta} L(\theta) I_s}_{\text{A}} + \underbrace{I_s^T \frac{d\phi_m(\theta)}{dt}}_{\text{B}} \right) \tag{4.16}$$

the torque is a function of two terms. The term A is the reluctance torque and it is present for anisotropic machine. The other contribution (term B) is always present and it is given by the interaction between rotor and stator magnetic field. For the sake of simplicity, in this paragraph, the full analytical description is not reported. To have a deeper overview of brushless machines, it is recommended to consult literature contributions provided by [33–35, 37].

4.2.3 Park's transformation

To achieve a more compact representation of the physical quantities, the Park's transformation is introduced. A detailed explanation is reported in [38–41]. Let us consider three variables which depends by the time, for example: $I_a(t)$, $I_b(t)$, $I_c(t)$. It is now possible to define a vector $\bar{I}$ and a scalar I_0 such that:

$$\begin{cases} \bar{I} = k \left(I_a + I_b e^{j\frac{2}{3}\pi} + I_c e^{j\frac{4}{3}\pi} \right) = I_d + jI_q \\ I_0 = I_a + I_b + I_c \end{cases} \tag{4.17}$$

The system presented above represents the Park's transformation of the variables $I_a(t)$, $I_b(t)$, $I_c(t)$. Let us consider a system given by three sinusoidal quantities with their amplitude equal to I_m, their average value of I_0 and switched of $2/3\pi$. The Park's transformation can be also expressed by means the following transformation:

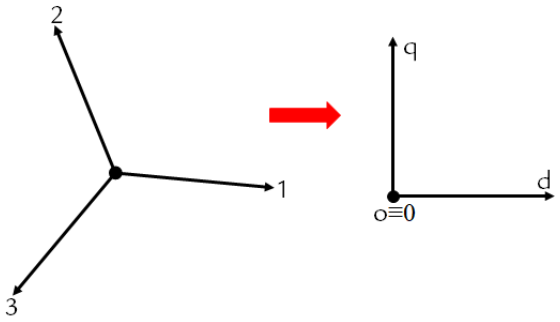

Figure 4.3 Schematic representation of Park's transformation

$$\begin{bmatrix} I_d \\ I_q \\ I_0 \end{bmatrix} = T(\theta) \begin{bmatrix} I_a \\ I_b \\ I_c \end{bmatrix}$$

where:

$$I_a = I_m e^{j\theta} \tag{4.18}$$

$$I_b = I_m e^{j(\theta+\frac{2}{3}\pi)} \tag{4.19}$$

$$I_c = I_m e^{j(\theta+\frac{4}{3}\pi)} \tag{4.20}$$

while the transformation matrix $T(\theta)$ is equal to:

$$T(\theta) = \begin{bmatrix} cos\theta & cos(\theta - \frac{2}{3}\pi) & cos(\theta + \frac{2}{3}\pi) \\ -sin\theta & -sin(\theta - \frac{2}{3}\pi) & sin(\theta + \frac{2}{3}\pi) \\ \frac{1}{\sqrt{2}} & \frac{1}{\sqrt{2}} & \frac{1}{\sqrt{2}} \end{bmatrix}$$

This transformation defines three new coordinates named *direct component*, *quadrature component* and *zero component*. In Fig.4.3, a schematic representation of the Park's transformation is reported. From the physical point of view, the Park's transformation allows to transform three-phase electrical machine in a two-phase equivalent electrical machine. These magnetic axes are coincident with the q and d axes. Moreover they are also orthogonal. For a symmetrical three-phase system the value of a *zero component* is always null.

4.2.4 Park's equations of electrical machines

In this paragraph, the mathematical equations in the Park's domain of an electrical machine are reported. A detailed Park's transformation discussion is reported in

[38, 39]. For sake of brevity, just the final equations are shown. For the stator voltages in the Park's domain, it will be obtained:

$$\begin{cases} V_d = R_s I_d - \omega L_q I_q \\ V_q = R_s I_q + \omega \phi_{PM} + \omega L_d I_d \end{cases} \tag{4.21}$$

where:

- ϕ_{PM} is the permanent magnet flux linkage;
- R_s is the stator resistance;
- L_q and L_d are the stator auto inductances of q and d axes respectively;
- I_q and I_d are the stator currents of q and d axes respectively.

the electrical power can be written as:

$$P_{\text{el}} = \frac{3}{2}\Big(V_q I_q + V_d I_d\Big) \tag{4.22}$$

by inserting eqs. 4.21 in eq. 4.22, the electrical power becomes:

$$P_{\text{el}} = \frac{3}{2}\Big[R_s\Big(I_q^2 + I_d^2\Big) + \omega \phi_{PM} I_q - \Big(L_q - L_d\Big)\omega I_d I_q\Big] \tag{4.23}$$

in this equation, it can be individuated two contributions:

$$\begin{cases} P_{\text{Joule}} = \frac{3}{2}\Big[R_s\Big(I_q^2 + I_d^2\Big)\Big] \\ \mathbf{P}_{\text{mecc}} = \frac{3}{2}\Big[\omega \phi_{PM} I_q - \Big(L_q - L_d\Big)\omega I_d I_q\Big] \end{cases} \tag{4.24}$$

where P_{Joule} represents the dissipative contribution of the electrical power while the term P_{mecc} is the mechanical power written in the Park domain. By dividing the mechanical power by the mechanical angular speed ω_{mecc}, the mechanical torque is expressed as:

$$\mathbf{T} = \frac{3}{2} pp\Big[\phi_{PM} I_q - \Big(L_q - L_d\Big) I_d I_q\Big] \tag{4.25}$$

where the terms $\Big(L_q - L_d\Big) I_d I_q$ is the reluctance torque which is not equal to 0 for anisotropic machine $L_q \neq L_d$.

4.2.5 Electrical machines operating regions

A Permanent Magnet Synchronous Motor has both voltage and current constraints. They depend on both their nominal values set by the manufacturer and on the power supply limits. The machine operating regions will be examined at steady state operating conditions which means that: three-phase voltages and currents are sinusoidal signals and their amplitude and frequency are constant. This is true also for ω and all quantities transformed in the Park's domain. The aforementioned constraints can be described as follow:

- $\sqrt{I_q^2 + I_d^2} \leq I_{\max}$. $I_{\max}$ is the current of the three-phase machine which corresponds to the concatenated nominal current *Root Mean Square* (RMS) value ($I_{\max} = \sqrt{2} I_{\text{nom}}$). This constraint has a circle trajectory in the $d-q$ reference frame;
- $\sqrt{V_q^2 + V_d^2} \leq V_{dc,f}$ where $V_{dc,f}$ is the DC voltage which corresponds to the concatenated stator value.

By introducing the eqs. 4.21 in the voltage constraint equation it is possible to obtain:

$$\left(R_s I_d - \omega L_q I_q\right)^2 + \left(R_s I_q + \omega \phi_{PM} + \omega L_d I_d\right)^2 \leq V_{dc,f}^2 \tag{4.26}$$

Current and voltage constraints involve torque and speed limitations as well. It can be easily represented in the $d-q$ reference frame reported in Fig. 4.4. The current limit is given by the red circumference with its radius equal to $I_{\max}$, while the voltage limit is described by the ellipse equation. This shrinks when the rotor angular speed increases. The center coordinates of the ellipse are:

$$\begin{cases} C_d = \frac{\phi_{PM}}{L_d} \\ C_q = 0 \end{cases} \tag{4.27}$$

while the minor semi-axis and the major semi-axis are respectively:

$$\begin{cases} S_{\min} = \frac{V_{dc,f}}{pp\omega L_q} \\ S_{\max} = \frac{V_{dc,f}}{pp\omega L_d} \end{cases} \tag{4.28}$$

A Permanent Magnet Synchronous Motor operating point, at a given speed, corresponds to a working condition inside both the voltage and the current limits. If the working point corresponds to an operating condition where the rotor angular speed is low with

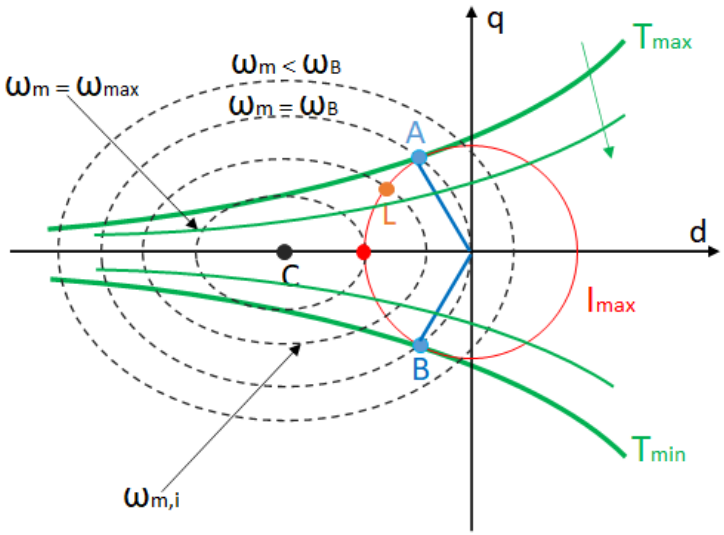

Figure 4.4 Brushless machine operating regions

respect to the maximum achievable, the voltage constraint is large. Therefore, the current limit is the one more limiting. In this case, it appears convenient to follow the AB trajectory which is called *Maximum Torque Per Ampere* (MTPA) curve and a further description can be found in [40, 42] . It represents the set of minimum pairs (I_d, I_q) which allows to achieve the desired torque level. It must be noticed that it corresponds to a set of points such that I_d is negative. Moreover, the MTPA curve represent the maximum efficiency condition for the electrical machine, Joule losses are limited in this case. The MTPA trajectory can be followed if the locus point AB is internal to the voltage limite $\omega_m = \omega_B$, where ω_B is the maximum motor angular speed such that the nominal torque is always available. If the intersection between the torque curve and the MTPA does not lie inside the voltage constraint $\omega_m \geq \omega_B$, the machine works in *Field-Weakening* (FW) condition [43, 41]. The FW operating point condition can be represented by the L point of the Fig. 4.4. In this condition the maximum torque achievable is lower then the nominal torque. Moreover, it decreases with the angular speed of the rotor and becomes equal to 0Nm if $\omega_m \geq \omega_{\max}$; in this case current and voltage constraints intersect on the direct axis.

4.2.6 Maximum Torque Per Ampere trajectory

In Fig. 4.4, the green curves represent the constant torque curves. There exist two asymptotes: the first one is $I_d = 0$ and the other is $I_d = \phi_{PM}/(L_q - L_d)$. As already said, a locus point exist such that it is possible to ensure the desired torque at maximum

efficiency condition. In order to obtain the MTPA [40, 42], some assumption must be done:

- the brushless machine is working as a motor, this is done to perform computations which can reflect the discussion for the generator operating mode;
- It is assumed that I_d is negative. This represents a FW [43, 41] operating mode as well. It corresponds to the working condition in which the rotor is rotating at an angular speed faster than the nominal one.

It is now possible to write I_q as a function of the torque:

$$I_q = \frac{\mathbf{T}}{\frac{3}{2}pp\Big[\phi_{PM} I_q - \Big(L_q - L_d\Big) I_d\Big]} \tag{4.29}$$

by introducing now the current constraint equation:

$$I_{\max} = \sqrt{I_q^2 + I_d^2} \tag{4.30}$$

and considering the derivative of equation 4.30 with respect I_d it is obtained:

$$\frac{dI_{\max}}{dI_d} = \frac{1}{\sqrt{I_q^2 + I_d^2}} \left[I_d + I_q \frac{dI_q}{dI_d} \right] \tag{4.31}$$

in eq. 4.31 the terms dI_q/dI_d can be expressed by showing the derivative of the eq. 4.29 as follow:

$$\frac{dI_q}{dI_d} = \frac{3/2\mathbf{T}pp(L_q - L_d)}{\left\{ 3/2pp\Big[\phi_{PM} - \Big(L_q - L_d\Big) I_d\Big] \right\}^2} = \frac{L_q - L_d}{\phi_{PM} - \Big(L_q - L_d\Big) I_d} I_q \tag{4.32}$$

By introducing eq. 4.32 in eq. 4.31 and imposing that it is equal to 0, it is possible to obtain the MTPA trajectory as:

$$I_q^2 = I_d^2 - I_d \frac{\phi_{PM}}{\Big(L_q - L_d\Big)} \tag{4.33}$$

This is a quadratic polynomial equation which represents a curve, symmetric with respect to the d axis and passing through (0,0). Moreover, this equation describes a curve which lies in the second and third quadrant of the $d-q$ plane. It has been found that the MTPA curve is valid both for motor and for generator working mode.

Chapter 5

Essentials of three-phase Power converters

5.1 Overview

The power converter plays a crucial role in the HEVs [37]. The aim of the PC is the power management between the electrical devices such as energy storage and electrical machine. In other words, the PC transforms the power which comes from the main source to the one needed to drive the motor. Typically, the main power source is usually either the three-phase electrical current or a direct current. In the HEV, the power flux can go from the source to the driven machine and vice versa. Moreover, it is supported by a control system which aims to ensure the desired performance of the whole system. The PC is able to transform the energy characteristics of the available source into the most reasonable form required from the motor. The power conversion process needs to be achieved in the most efficient way. Due to these reasons, a PC is usually made up of static power semiconductors such as power DIODE, *Insulated-Gate Bipolar Transistor* (IGBT), *Bipolar Junction Transistor* (BJT) and, *Metal-Oxide-Semiconductor Field-Effect Transistor* (MOSFET). All of them are semiconductor devices that are connected to each other in different layouts depending on the particular power conversion requested. Description of power semiconductors can be found on the following literature contributions [44–47].

5.1.1 Power converter classifications

Typologies of power converter

The power converter can be classified as follows:

- AC/DC converter: known as *rectifier*, produces a continuous voltage with variable amplitude from an alternate source with constant frequency and amplitude;
- DC/DC converter: known as *chopper*, it provides a continuous voltage with variable amplitude from a continuous and constant source;
- AC/AC converter: known as *frequency converter*, returns a variable voltage, both in frequency and amplitude, from an alternate voltage whose amplitude and frequency are constant;
- DC/AC converter: known as *inverter*, it outputs a variable voltage, both in amplitude and in frequency from a continuous and constant source.

In the automotive applications, the main involved motors are AC three-phase motors. For this kind of EM a three-phase AC voltage power supply is required. Since the ES provide DC power an *inverter* is necessary to allow the energy flow from the energy storage to the AC MGU. When the MGU works also as a generator, a *rectifier* is required. In most cases, the same device is designed to work properly both as *inverter* and *rectifier*.

Number of levels

A PC is capable of managing both the AC output voltages amplitude and frequency with a given value of DC bus input voltage. A variable output AC voltage can be achieved by modifying the inverter gain, defined as the ratio between the AC output voltage and the DC input voltage, by means a *Pulse Width Modulation* (PWM) control process. As found in Ref. [37], the PC allows to obtain a voltage waveform having both variable frequency and amplitude. However, the waveform returned from this device is not sinusoidal but squared, which is generated by pulses whose duty cycle varies over time. The squared voltage waveform is due to the PWM technique applied to control the device. In fact, a PC provides an AC voltage waveform by repeatedly switching between voltage levels defined in relation to the DC voltage supply available. The number of voltage levels must be at least two to feed to the motor with an AC waveform. On the contrary, the outputs waveform would be a continuous line. So,

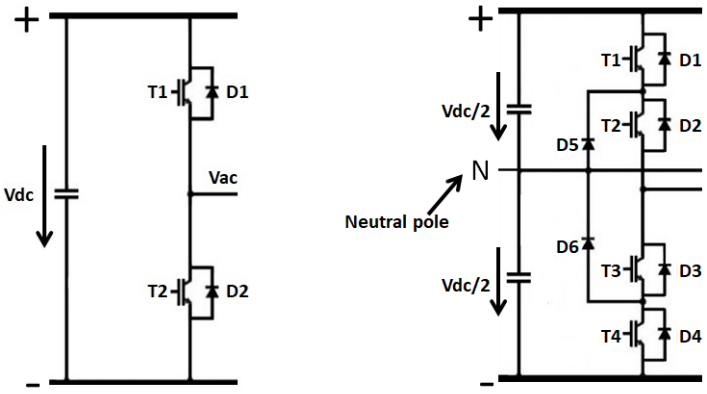

(a) (b)

Figure 5.1 (a) 2L PC phase leg, (b) 3L PC phase leg

the number of levels is an important parameter of PCs. In Figs. 5.1(a) and 5.1(b), schematic representations of a 2L PC phase leg and a 3L PC phase leg are provided. For the 2L case, just the positive and the negative connections are present on the DC side. Instead, for the 3L case, in addition to the positive and negative terminals, also the neutral terminal is present.

PC having more than 2L are called multilevel PC. Multilevel power converters are usually employed to improve the quality of the output signals. However, by increasing the number of levels the device becomes more complex and expensive. In the industrial applications, the most common architectures are the 2L and 3L ones. A 3L PC can be built in a *Neutral-Point Clamped* (NPC) or *T-type Neutral-Point Clamped* (TNPC) topologies [19]. For the sake of simplicity, in the present study, PC performance are investigated on both 2L and 3L in a NPC topologies. In Figs. 5.2(a) and 5.2(b), the squared waveform of 2L and 3L PCs are reported.

5.1.2 The switch combinations

For sake of simplicity, the electric scheme of a traditional 2L three-phase power converter is shown in Fig. 5.3. In the description, the DC bus voltage (V_{dc}) is given by two DC voltage generators (of $V_{dc}/2$) connected in series. The described PC is composed by six switches with six diodes in parallel. These devices are connected to form three legs. The switches are electronic devices controlled both in switching ON and OFF, instead the diodes are passive devices required to give a closing path to the currents at each opening of switch.

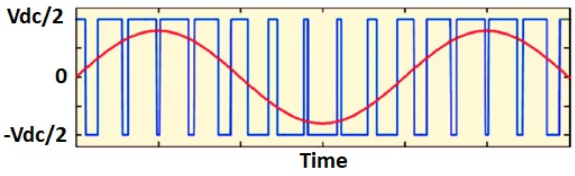

(a)

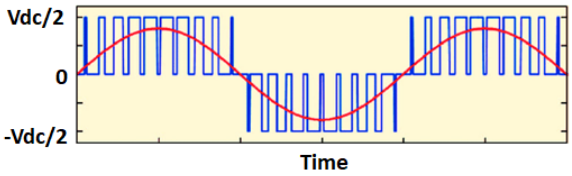

(b)

Figure 5.2 (a) 2L squared voltage waveform, (b) 3L squared voltage waveform

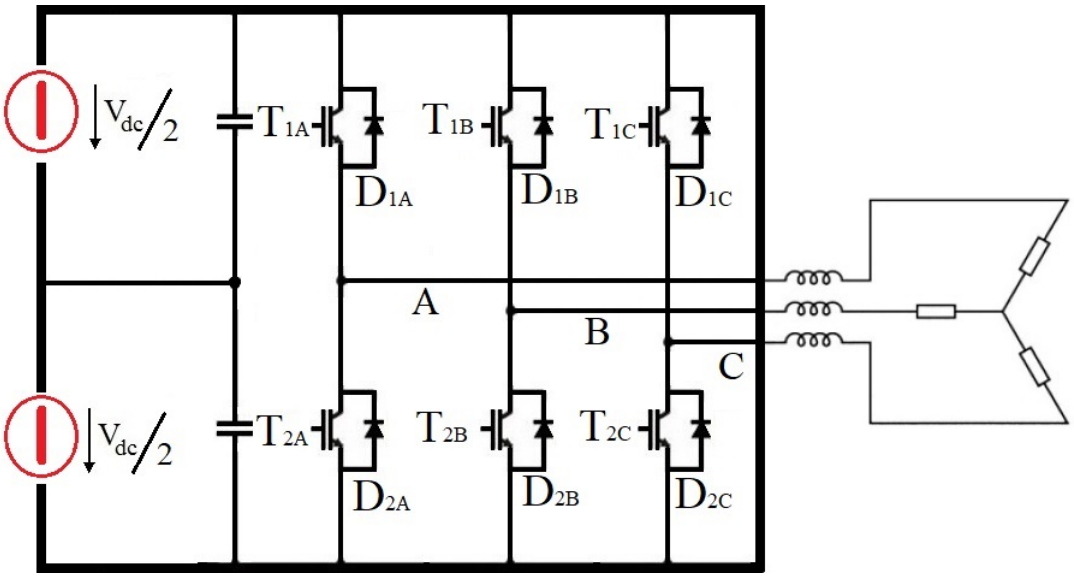

Figure 5.3 Schematic representation of a three-phase 2L PC

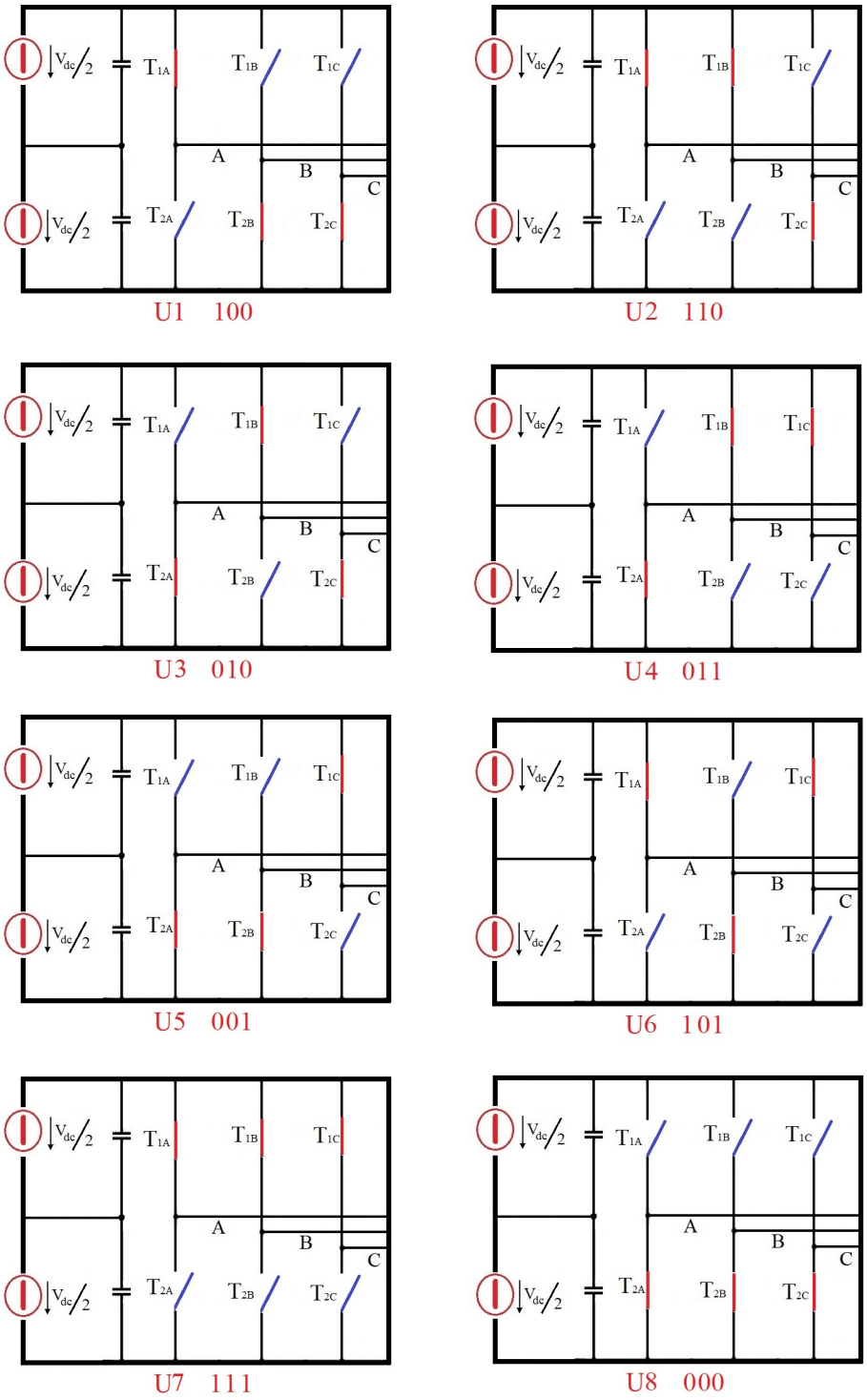

Figure 5.4 The ON and OFF states of the six PC switches

Considering a 2L three-phase PC, the possible switch combinations are only eight as proposed in Fig. 5.4. With the adopted convention, for example, the number 1 indicates the state ON of high side (T1) and state OFF of low side (T2) of the same leg. For example, 100 represents T_{1A} = ON, T_{1B} = OFF, T_{1C} = OFF, T_{2A} = OFF, T_{2B} = ON, and T_{2C} = ON. This description is well explained in ref. [37]. In a three-phase PC, different power semiconductors are employed such as DIODE, IGBT, BJT and MOSFET. They are used fundamentally in switching mode (ON or OFF state). The most used materials for power semiconductors devices are silicon and silicon carbide. A detailed description of such devices can by found in literature [44–47].

5.1.3 Modulation techniques

Over the years, several types of PWM modulation techniques are developed such as square wave (six-step), carrier-based PWM and *Space Vector Modulation* (SVM) [37]. The aims of such techniques are: simple implementation, high max inverter gain, lower switching losses, and lower Total Harmonic Distortion of waveform. In this chapter a short description of the carrier-based PWM is given.

Carrier-based PWM

In the current industrial applications, the most used technique is *Sinusoidal Pulse Width Modulation* (SPWM) technique. This modulation technique is given by a sinusoidal reference signal of amplitude V_m and a triangular carrier of amplitude V_Δ. The frequency of the reference signal (f_m) determines the fundamental frequency of output voltage, while the carrier wave frequency (f_{sw}) represents the switching frequency of the power converter. In Fig. 5.5 (taken from [37]), a representation of 2L inverter carrier-based PWM is shown. The ratio between V_m and V_Δ is known as modulation index and is expressed in Eq. 5.1:

$$M = \frac{V_m}{V_\Delta} \tag{5.1}$$

Eq. 5.2 shows another important index which is typically higher than 30. It is the given by the ratio between f_m andf_{sw}:

$$Y = \frac{f_{sw}}{f_m} \tag{5.2}$$

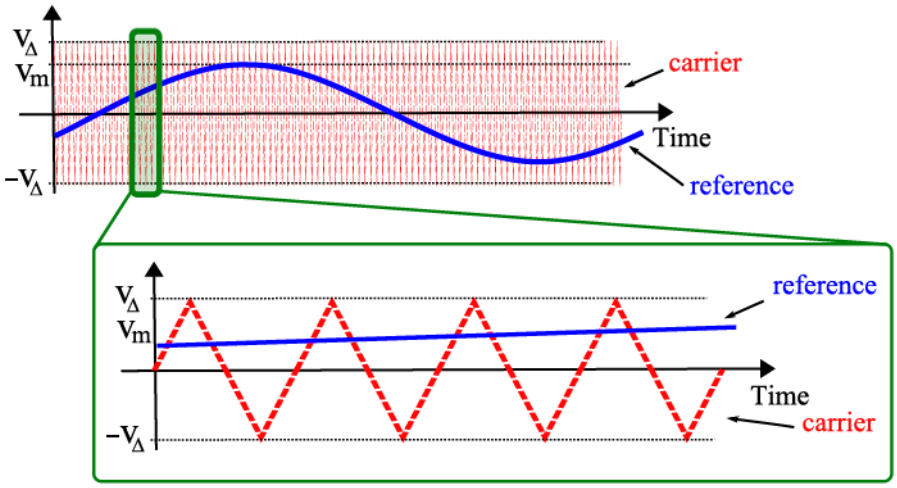

Figure 5.5 2L inverter carrier-based PWM. Reprinted from [37]

The strongest point of this modulation techinque is given by the low number of commutations and by the fact that it is easy to implement. When an higher output voltage is required, the modulation index needs to be increased above 1. The region with $M > 1$ is called *over-modulation*. To increase the limit of the output voltage of SPWM different strategies are taken into account. The most common is given by third harmonic PWM injection. For sake of brevity, literature contributions are suggested to have an overview on this topic [37, 48, 49].

5.2 Power dissipation

During PC operations, all power semiconductors are interested by ON and OFF mode. The switching phases are not instantaneous and energy losses occur in these operations. Moreover, power dissipation of PC are also due to the non-ideality of power semiconductors mentioned previously. There are two main dissipation typologies:

- Conduction losses;
- Commutation or switching losses.

5.2.1 Conduction losses

This kind of dissipation occur during the on-state of power semiconductors and they are also called Joule losses. The involved parameters that allows to quantify power dissipation are:

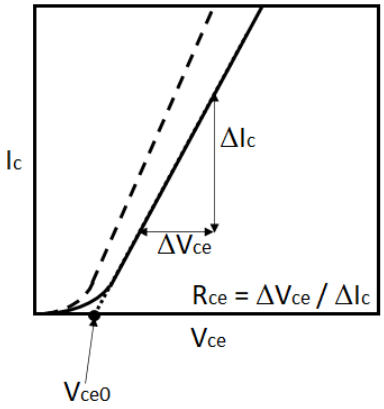

Figure 5.6 V_{ce} as a function of electric current and temperature ($Tj = 25$°C dashed line, $Tj = 150$°C continuous line)

- the collector-emitter voltage (V_{ce}) if we are facing with an IGBT, in case of DIODE the analogous parameters is the forward voltage (V_f). It represents the threshold value which allows to device to work;
- the internal resistance of the device which is called collector emitter resistance (r_{ce}) for a IGBT, forward resistance (r_f) for a DIODE and on-state drain source resistance (r_{ds}) for a MOSFET.

The mentioned physical magnitudes are detailed described in [44–47]. These parameters are characterized and provided by power modules manufacturers: in the datasheet, it is presented power semiconductor behavior as a function of their operating conditions. They basically depend by the operating temperature, current and voltage. To quantify conduction losses, it is possible to take into consideration an IGBT and to consider the V_{ce} characteristics as seen in Fig. 5.6. It is possible to observe that when the semiconductor is working, the collector-emitter voltage can be written as:

$$V_{ce} = V_{ce0} + r_{ce} I_c(t) \tag{5.3}$$

with I_c the current value involved when the semiconductor circuit is closed. To obtain the conduction losses, eq. 5.3 needs to be multiplied by I_c as written below:

$$P_{\mathrm{c,IGBT}}(t) = V_{ce0} I_c(t) + r_{ce} I_c^2(t) \tag{5.4}$$

Let us suppose that the current $I_c(t)$ is a periodical function and its period is Θ. In order to compute an average value of conduction dissipation over the period, it can be

written:

$$P_{\mathrm{c,IGBT}} = \frac{1}{\Theta}\int_0^{\Theta}\left[V_{ce0}I_c(t) + r_{ce}I_c^2(t)\right]dt \; = \frac{V_{ce0}}{\Theta}\int_0^{\Theta} I_c(t)\,dt \; + \frac{r_{ce}}{\Theta}\int_0^{\Theta} I_c^2(t)\,dt \tag{5.5}$$

and from eq. 5.6 it is possible to define the average current and the square of the effective current value as:

$$\begin{cases} I_{\mathrm{avg}} = \frac{1}{\Theta}\int_0^{\Theta} I_c(t)\,dt \\ I_{\mathrm{eff}}^2 = \frac{1}{\Theta}\int_0^{\Theta} I_c^2(t)\,dt \end{cases} \tag{5.6}$$

therefore, eq. 5.6 assumes the following formulation:

$$P_{c,IGBT} = V_{ce0}I_{\mathrm{avg}} + r_{ce}I_{\mathrm{eff}}^2 \tag{5.7}$$

if we extend the same analysis to a diode, the eq. 5.7 would be:

$$P_{c,DIODE} = V_{f0}I_{\mathrm{avg}} + r_f I_{\mathrm{eff}}^2 \tag{5.8}$$

while for a MOSFET the equation becomes:

$$P_{c,MOSFET} = r_{ds}I_{\mathrm{eff}}^2 \tag{5.9}$$

since only the resistive contribution is included [46]. These formulations are written in the general form. I_{avg} and I_{eff} assume a different formulation on the basis PC topology. In the following chapter, the conduction losses will be presented in their final form for 2L and 3L NPC power converters.

5.2.2 Switching losses

Switching or commutation losses occur at any power semiconductor commutation event. They can be quantified in three different contributions as discussed below:

- E_{on} is the energy lost by an IGBT or MOSFET during the activation phase;
- E_{off} is the energy lost by an IGBT or MOSFET during the deactivation phase;
- E_{rr} is the reverse recovery energy stored by a DIODE during the transistor deactivation operations.

In Fig. 5.7, a picture of the mentioned parameters as a function of electric current and voltage is presented. It is worth to say that these parameters are also a function of the temperature. Their dependency is usually described in the power module datasheet

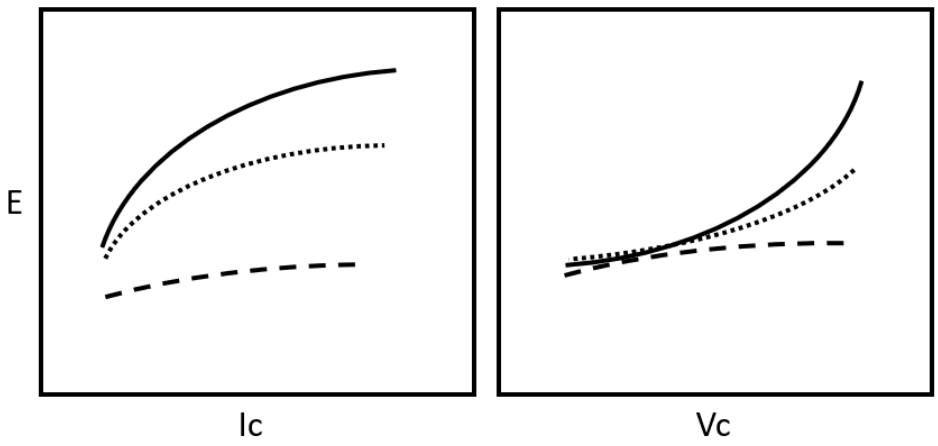

Figure 5.7 E_{on} dotted line, E_{off} continuous line, E_{rr} dashed line

provided by the manufacturers. To quantify the switching losses, the switching energy needs to be multiplied by the switching frequency f_{sw}. In the next section, switching dissipation will be presented in their final form for 2L and 3L power converters.

5.2.3 Operating conditions dependencies

In general, the operating condition of the power converter could change dynamically during its operations in terms of current, voltage, and temperature. For this reason, to have an accurate power losses estimation, compensation based on environmental conditions to any parameter must be introduced. Temperature, current and voltage dependencies of both conduction and switching parameters are usually reported on datasheet diagrams. To have an idea of power semiconductor dependencies by their operating conditions, a representation of V_{ce} and E_{off} of an IGBT device is shown in Fig. 5.8. As a matter of fact, both conduction (V_{ce}, V_f, r_{ce}, r_f, and r_{ds}) and switching parameters (E_{on}, E_{off}, and E_{rr}) must be modeled by taking into account their dependencies over different operating conditions. Researches explored different model to describe the power semiconductors behavior. In Ref. [9], a linear approximation of switching parameters has been taken into account. Power module manufacturers suggest to model these parameters by following a look-up table approach or by scaling them by means the introduction of coefficients [6]. As a matter of fact, coefficients are provided by power module suppliers and change by virtue of the power module considered. In Refs. [6] and [7] conduction and switching losses are modeled by considering a polynomial description.

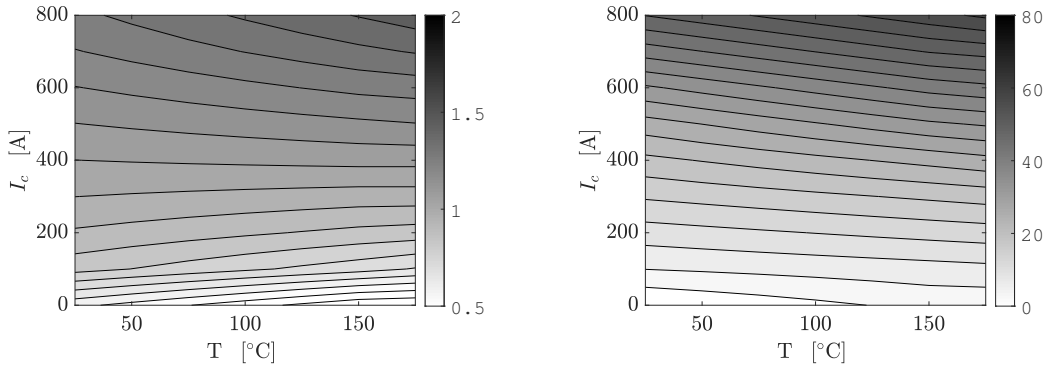

(a) (b)

Figure 5.8 (a) V_{ce} [V] as a function of electric current and temperature, (b) E_{off} [mJ] as a function of electric current and temperature

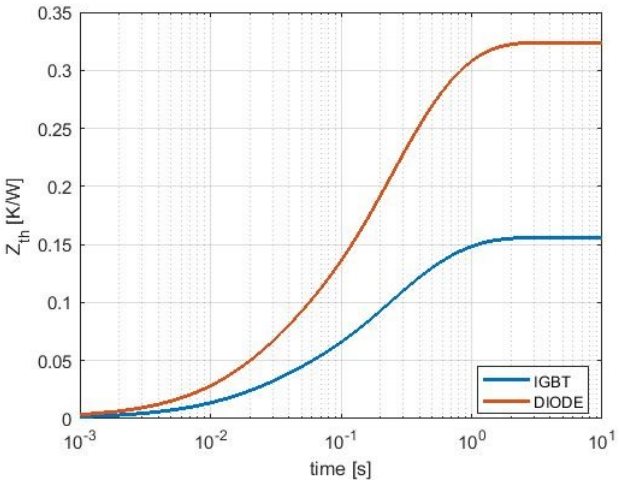

Figure 5.9 Example of thermal impedance of a power DIODE and an IGBT

As previously described, power electronic devices are interested by dissipation during the working conditions. Therefore, these devices must be equipped by an heat sink. It is employed to maintain the chip temperature below the limit value to prevent failure. Usually, power semiconductor limit temperature can be found on datasheet provided by the manufacturers. Thermal management plays an important role in the reliability of power electronic devices. Thermal properties of DIODEs, IGBTs and other power switches are basically reported by taking into account the thermal impedance (Z_{th}). The power semiconductor temperature is known as junction temperature (T_j). As found in many manuals drawn up by suppliers [19, 50], the power device thermal impedance can be schematized by considering a Resistance-Capacitance (RC) network [7]. Different models are found in literature and the most common are

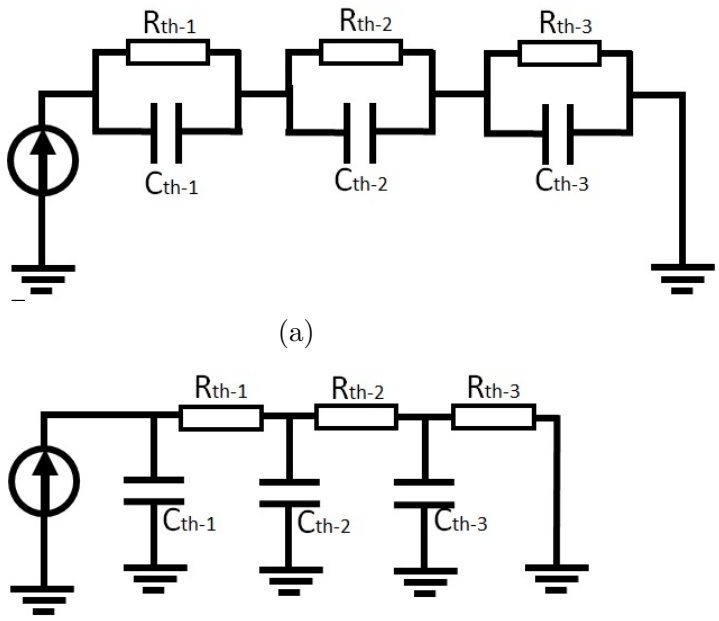

Figure 5.10 (a) Foster network , (b) Cauer network

the socalled *Foster Network* [51] and the *Cauer Network* [52]. Both of network models are represented by multi-stage *RC* network. They link the chip junction to the power module heat sink. In Figs 5.10(a) and 5.10(b), a representation of *Foster Network* and *Cauer Network* is respectively reported. Therefore, the thermal response of a power device can be described through the mentioned networks. A mathematical description of Z_{th} for a Foster network is reported in the following equation:

$$Z_{\text{th}} = \sum_{i=1}^{N} R_{\text{th,i}}\left(1 - e^{t/\tau_i}\right) \tag{5.10}$$

where:

$$\tau_i = R_{\text{th,i}} C_{\text{th,i}} \tag{5.11}$$

$R_{\text{th,i}}$ and $C_{\text{th,i}}$ are the thermal resistance and capacitance respectively at the i-th stage. The time constant (τ_i) is obtained by means the multiplication of these magnitudes.

Chapter 6

Power converter losses evaluation: the Virtual Test Bench

6.1 Overview

Over the years, a large number of studies focused on PC performance evaluation. Several methods can be found in literature to evaluate PC losses. Experimental tests do not allow a fast investigation and in the preliminary design phase only the total PC losses can be obtained [5]. In general, analytical models are usually adopted to overcome these limitations. For example, in Ref. [6], the power losses are described through polynomial formulations. The computation of switching and conduction losses is very accurate, but the methodology could be complicate to be used in simulation tools. Also in Ref. [7], power losses are based on polynomial fitting curves based on datasheet values and/or experimental results. The implemented scheme is accurate but only pulse test condition is explored for the specific case. Schweizer et al. [8] performed a per chip losses characterization, their methodology is useful to address the design of a custom module, however the losses calculation requires some computational efforts. In Ref. [9], PC losses are averaged across a switching cycle. Switching energy parameters are linearly approximated with current and voltage while no current and/or temperature dependencies are included for conduction parameters. This could lead to low accuracy when extending the operating conditions range in terms of current and/or voltage. Some interesting studies investigate PC behavior in dynamic conditions: in Ref. [53], PC losses are calculated at each operating point of the cycle, however the implemented procedure does not completely allow to split the losses in switching and conduction contributions. Bryant et al. [54] have considered a dynamic load cycle to perform an optimization of semiconductor devices in terms of switching condition.

However, the conduction losses are not treated. Asus et al. [55] developed a model able to predict hybrid car performance over a race cycle but PC behavior is not treated in detail.

All of the mentioned works are very interesting, however some shortcomings are present in the existing methods. The aim of this part of the work is to present an electro-thermal simulation tool able to accurately address the design of PCs at low computational cost. Any converter configuration can be easily investigated over a wide operational range, in both steady-state and time-dependent conditions. Moreover, the method allows to split the power losses in switching and conduction contributions. The power module characteristics are detailedly represented by look-up tables extracted from datasheet diagrams [56]. The proposed tool enables the anticipated identification of designs to be rejected because of their low efficiency. In this way, only the most promising solutions are selected to be subjected to an experimental evaluation.

In this work, a large simulation campaign is performed. Both 2L and 3L PC topologies are considered. Besides the two different topologies, also different technologies are examined like Si IGBTs and SiC MOSFETs [19]. In detail, for 2L PC configuration, Infineon IGBT3 [20], Infineon EDT2 [21], and ROHM SiC MOSFET [22] power modules are considered while 3L PC configuration is equipped with Semikron IGBT3 [23] power module. Prior to the numerical study, the tool is successfully validated against experimental tests and literature results reported in Ref. [6]. The PC input conditions are defined by: MGU torque demand (T_{MGU}), MGU angular speed (n_{MGU}), bus DC voltage (V_{dc}), and PC switching frequency (f_{sw}). Each configuration is investigated over a large steady-state simulation matrix including 260 points and over two drive cycles. PC losses are computed and the operating conditions sensitivity is assessed. The introduction of the Power losses and Usage time maps allow to obtain a detailed analysis of the PC behavior through the drive cycles. Moreover, the impact of the drive cycle on PC performance is quantified by means the introduction of $P_{d,cycle}$. Finally, also an evaluation which takes into consideration the power dissipation of single chips is conducted. This is important to study the cooling strategy of the power module. The method is deemed promising and can be recommended for the use in the preliminary design of PCs. Simulation time is very short, less than 80s are required to detect all steady-state simulation matrix points. Potentially critical operating conditions can be individuated and avoided to ensure reliability of such devices. In addition, the methodology offers a potential in numerical optimization.

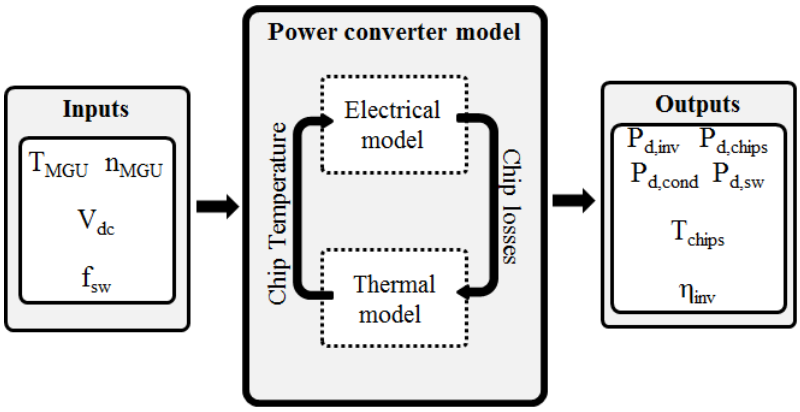

Figure 6.1 Schematic representation of tool operations

6.2 Methods and Materials

To numerically emulate the behavior of a PC, a detailed lumped model is created on MATLAB/Simulink platform [57]. The proposed PC model is split into three main areas (Fig. 6.1):

- Input block to feed the simulation with the needed data sources: T_{MGU}, n_{MGU}, V_{dc}, and f_{sw}. As a matter of fact, also MGU parameters such as flux linkage, pole pairs number, inductances and resistance must be defined;
- PC model is made by two main blocks: electrical model and thermal model. The first allows to calculate the electrical magnitudes in the Park's domain [38] requested from MGU (both FW [43] and MTPA [42] algorithms are included) on the basis of the operating conditions. The second allows to evaluate the power module dissipation and temperature by using the *RC* Foster network method. Electrical and thermal models are connected each other;
- Output block to collect all the output data desired to evaluate power module performance.

6.2.1 The analytical model of power converter

The currents generation algorithm

The equations, employed for computing the MGU electrical magnitude, have been shown in Chapter 4. Currents and voltages, computed in Park's domain, are function of operating conditions and MGU properties. Here, a description of the implemented

algorithm is presented. The block needs to be fed by n_{MGU}, T_{MGU} and V_{dc} signals. Since in Chapter 4, the torque of the motor has been indicated by **T**, it is worth to say that it is equal to T_{MGU} aforementioned. Moreover, the mechanical motor speed is indicated by n_{MGU} which its unit of measurement is in revolution per minute. It is worth to remember the link between ω_m and n_{MGU} as follows: $\omega_m = (2\pi n_{MGU})/60$. Magnitudes on quadrature and direct axes are computed either by finding the intersection of torque curve with the MTPA trajectory or by following FW working mode. MTPA control strategy ensures that for a required torque level the minimum stator current magnitude is provided. This leads to a Jolue losses reduction. The FW condition is while enabled when the the speed increases and the machine voltage constraint shrinks. In order to obtain the appropriate current target trajectories, the torque equation needs to be combined with the electrical constraints:

- the first step is to find the intersection between the torque curve and the MTPA trajectory, equations 4.33 and 4.25 must be considered. The system becomes:

$$\begin{cases} I_q^2 = I_d^2 - I_d \frac{\phi_{PM}}{\left(L_q - L_d\right)} \\ T_{MGU} = \frac{3}{2} pp \left[\phi_{PM} I_q - \left(L_q - L_d\right) I_d I_q\right] \end{cases}$$

  The combination of the system leads to a cubic polynomial: 2 real and an imaginary solutions are found. The interesting real solution corresponds to the smallest I_d value.

- the second step aims to find the intersection point between the demanded torque and the voltage constraint. Hence, in case of FW operation mode, the following system of two equations needs to be solved:

$$\begin{cases} \left(R_s I_d - \omega L_q I_q\right)^2 + \left(R_s I_q + \omega \phi_{PM} + \omega L_d I_d\right)^2 \leq V_{dc,f}^2 \\ T_{MGU} = \frac{3}{2} pp \left[\phi_{PM} I_q - \left(L_q - L_d\right) I_d I_q\right] \end{cases}$$

  this system has four solutions of the pair (I_d, I_q), two of them are reals while the others are found in the complex domain. Of course, just one solution is physically admitted. Again, it is found by checking the smallest I_d value corresponding of real polynomial solution.

Finally, I_d and I_q need to be chosen between the two algorithms. By considering the picture reported in Fig. 4.4, it can be understood that if the first solution lies within the voltage constraint, it will be selected. However, when the angular speed increases

it could happen that the first solution is not feasible anymore. Therefore, the pair resulting from the second algorithm is chosen. It is worth to say that ϕ_{PM}, pp, R_s, L_q and L_d are provided by the electrical machine manufacturers. Since I_d and I_q are defined, also V_d and V_q can be found by using the system of equations 4.21. In this way, the power factor ($cos(\varphi)$) can be found as:

$$cos(\varphi) = \frac{P_a}{\sqrt{P_a^2 + P_r^2}} \tag{6.1}$$

since the active power P_a and the reactive power P_r are expressed as:

$$\begin{cases} P_a = \frac{3}{2}\Big(V_d \cdot I_d + V_q I_q\Big) \\ P_r = \frac{3}{2}\Big(V_d \cdot I_d - V_q I_q\Big) \end{cases} \tag{6.2}$$

Power losses evaluation

A general PC losses description are reported in Chapter 5. In this section, the power dissipation are averaged across a switching cycle and reported in their final form, see Ref. [9] for details. Therefore, PCs dissipation assume a different formulation on the basis of the involved topology. In the current work, both 2L and 3L NPC topologies are considered. 2L is tested by using both Si IGBTs and SiC MOSFETs while 3L is tested by considering only Si IGBTs. Fig. 6.2 shows a single leg for each considered power module topology. Moreover, in the current study, a look-up table approach has been adopted to take into account the power semiconductor operating condition dependencies. SPWM is considered to control the power module activation and deactivation phases. Each converter leg is characterized by specific conduction and switching losses. In detail, referring to the 2L IGBT configuration, conduction losses are calculated for transistors and diodes as follow equation 6.3 and equation 6.4:

$$P_{c,T1T2} = \frac{V_{ce}\hat{I}}{2\pi}\left[1 + \frac{M\pi}{4}cos(\varphi)\right] + \frac{r_{ce}\hat{I}^2}{2\pi}\left[\frac{\pi}{4} + \frac{2M}{3}cos(\varphi)\right] \tag{6.3}$$

$$P_{c,D1D2} = \frac{V_f\hat{I}}{2\pi}\left[1 - \frac{M\pi}{4}cos(\varphi)\right] + \frac{r_f\hat{I}^2}{2\pi}\left[\frac{\pi}{4} - \frac{2M}{3}cos(\varphi)\right] \tag{6.4}$$

As previously said, V_{ce} and r_{ce} are the collector-emitter voltage and resistance respectively, while V_f and r_f are the forward voltage and resistance respectively. The current phase angle is given by φ while M is the modulation index. $\hat{I}$ (equation 6.5) is the

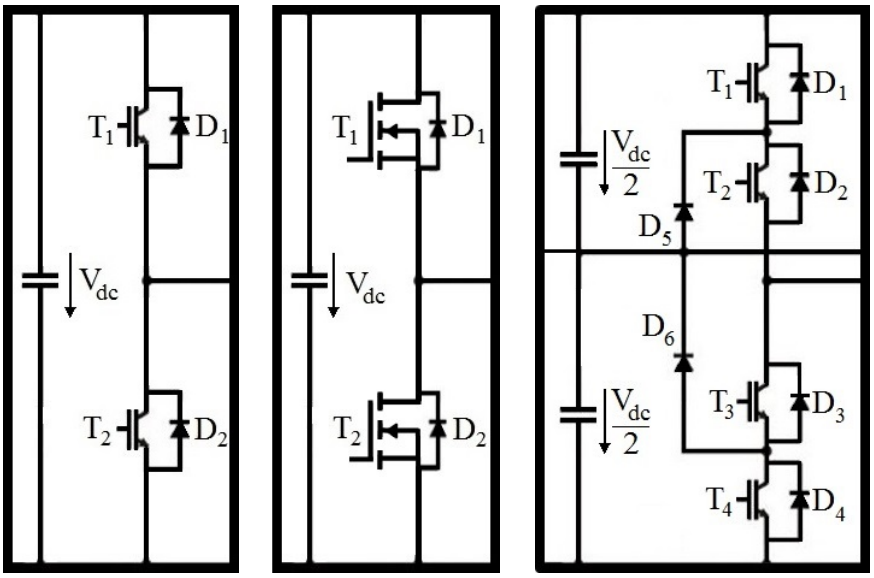

(a) (b) (c)

Figure 6.2 Single phase leg PC: (a) 2L topology - IGBTs, (b) 2L topology - MOSFETs, (c) 3L NPC topology - IGBTs

peak current defined as a function of direct-quadrature (I_q,I_d) currents calculated in Park's domain [38].

$$\hat{I} = \sqrt{I_q^2 + I_d^2} \tag{6.5}$$

About converter leg switching losses, they are calculated for transistors and diodes as follow:

$$P_{sw,T1T2} = \frac{f_{sw}}{\pi}\Big(E_{on} + E_{off}\Big) \tag{6.6}$$

$$P_{sw,D1D2} = \frac{f_{sw}}{\pi}E_{rr} \tag{6.7}$$

where E_{on}/E_{off} are activation/deactivation energy contributions and E_{rr} is the reverse recovery energy. In case of 2-Level topology equipped by MOSFET devices, the conduction losses of the transistor can be modeled as shown below:

$$P_{c,T1T2,\text{inv}} = \frac{r_{ds}\hat{I}^2}{2\pi}\left[\frac{\pi}{4} + \frac{2M}{3}cos(\varphi)\right] \tag{6.8}$$

$$P_{c,T1T2,\text{rec}} = \frac{r_{ds}\hat{I}^2}{2\pi}\left[\frac{\pi}{4} - \frac{2M}{3}cos(\varphi)\right] \tag{6.9}$$

where "inv" indicates that the PC works as inverter, "rec" indicates that the PC operates as rectifier. For commutation losses:

$$P_{sw,T1T2} = \frac{f_{sw}}{\pi}\Big(E_{on} + E_{off}\Big) \tag{6.10}$$

In this work, the chosen power module is not equipped with an external free-wheeling diode, but they exploit the one integrated into the MOSFET structure. Typically body diodes are poor in quality with respect to external ones. About switching losses, some researchers proposed formulations of E_{rr} [58–60] to take into consideration the losses of the body diode. Looking at conduction losses, instead, it is worth to say that the considered converter will use synchronous rectification, when the DIODE has to conduct, the antiparallel MOSFET will be switched on to reduce resistive path and hence overall power dissipation. For these reasons, it is reasonable to neglect them in this modeling. For power *Metal-Oxide-Semiconductor Field-Effect Transistors* (MOSFETs), the only resistive (r_{ds}) path formed by the drain-source channel is present. In case of 3L configuration, conduction losses are evaluated by using the following equations:

$$P_{c,T1T4} = \frac{V_{ce}\hat{I}M}{4\pi}\Big[sin(\varphi) + (\pi - \varphi)cos(\varphi)\Big] + \frac{r_{ce}\hat{I}^2M}{4\pi}\left[\frac{8}{3}cos^4\left(\frac{\varphi}{2}\right)\right] \tag{6.11}$$

$$P_{c,D1D4} = \frac{V_f\hat{I}M}{4\pi}\Big[sin(\varphi) - \varphi cos(\varphi)\Big] + \frac{r_f\hat{I}^2M}{2}\left[\frac{4}{3\pi}sin^4\left(\frac{\varphi}{2}\right)\right] \tag{6.12}$$

$$P_{c,T2T3} = \frac{V_{ce}\hat{I}}{\pi}\left[1 - \frac{M}{4}(sin(\varphi) - \varphi cos(\varphi))\right] + \frac{r_{ce}\hat{I}^2}{4}\left[1 - \frac{8M}{3\pi}sin^4\left(\frac{\varphi}{2}\right)\right] \tag{6.13}$$

$$P_{c,D2D3} = \frac{V_f\hat{I}M}{4\pi}\Big[sin(\varphi) - \varphi cos(\varphi)\Big] + \frac{r_f\hat{I}^2M}{2}\left[\frac{4}{3\pi}sin^4\left(\frac{\varphi}{2}\right)\right] \tag{6.14}$$

$$P_{c,D5D6} = \frac{V_f\hat{I}}{\pi}\left[1 - \frac{M}{4}(2sin(\varphi) - (2\varphi - \pi)cos(\varphi))\right] + \frac{r_f\hat{I}^2}{4}\left[1 - \frac{4M}{3\pi}(1 + cos^2(\varphi))\right] \tag{6.15}$$

Switching losses in 3-Level PC are evaluated by using the following formulae:

$$P_{sw,T1T4} = \frac{f_{sw}}{2\pi}\Big(E_{on} + E_{off}\Big) \cdot \frac{1 + cos(\varphi)}{2} \tag{6.16}$$

$$P_{sw,D1D4} = \frac{f_{sw}}{2\pi} E_{rr} \cdot \frac{1 - cos(\varphi)}{2} \tag{6.17}$$

$$P_{sw,T2T3} = \frac{f_{sw}}{2\pi}\Big(E_{on} + E_{off}\Big) \cdot \frac{1 - cos(\varphi)}{2} \tag{6.18}$$

$$P_{sw,D2D3} = 0 \tag{6.19}$$

$$P_{sw,D5D6} = \frac{f_{sw}}{2\pi} E_{rr} \cdot \frac{1 + cos(\varphi)}{2} \tag{6.20}$$

Thanks to these equations, converter power losses (P_d) and efficiency (η) can be evaluated as:

$$P_d = NF \cdot \left[\sum_{i=1}^{n}\Big(P_{c,Ti} + P_{sw,Ti}\Big) + \sum_{i=1}^{m}\Big(P_{c,Di} + P_{sw,Di}\Big)\right] \tag{6.21}$$

$$\eta = \frac{P_{\text{out}}}{P_{\text{in}}} = \frac{P_{\text{out}}}{P_{\text{out}} + P_d} \tag{6.22}$$

NF is the phase leg number which is equal to three for the current case, n and m are the number of the IGBTs/MOSFETs and DIODEs respectively. From eq. 6.22 it is clear that losses caused by *Gate Drive Board* (GDB) circuitry are not included in the described model. P_{in} and P_{out} are the input and output power of the PC. In the present study, the current is represented in RMS form (I_A) and it is defined as follows:

$$I_A = \frac{\sqrt{I_q^2 + I_d^2}}{\sqrt{2}} sign(I_q) \tag{6.23}$$

6.3 Validation

6.3.1 Steady-state conditions

To validate the proposed simulation tool, numerical data must be compared to experimental ones. The first validation step is performed in steady-state operating conditions. A 3L-NPC topology equipped with IGBT3 power modules [61] is considered. In Fig. 6.3, the considered experimental set-up is represented: the available PC is connected to a battery emulator to provide the bus DC voltage and to a MGU in a star connection configuration. Moreover, the power measurements of the PC at DC and AC sides are performed with WT1800 High Performance Power Analyzer [62]. The schematic representation of this device is reported in Fig. 6.3. To measure the AC power, the 3V3A measurement procedure has been followed. Three ammeters (A1, A2, A3) and three voltmeters (U1, U2, U3) are involved in the power measurements. In order to measure the DC power, the 1P2W measurement procedure has been considered. Moreover only an ammeter (A) and a voltmeter (U) are required. For the mentioned measurement procedures, a clear description is reported in the user's manual [63]. The WT1800 High Performance Power Analyzer is a high-performance power analyzer that guarantees has achieved a power-factor error (0.1%), in addition to a high basic power accuracy of ±0.1%. Direct input of measurement signals makes it possible to measure very small current that can hardly be measured with a current sensor. The WT1800 provides a direct input voltage range from 1.5V to 1000V (12 ranges) and a direct input current range from 10mA to 5A (9 ranges) or from 1A to 50A (6 ranges). The frequency lower limit has been reduced to 0.1Hz from the previous 0.5Hz (5-fold lower than the previous model) to meet the requirement for power measurements at a low speed. Furthermore, high-speed data collection at a data update rate of up to 50ms has been inherited. In addition to normal measurement data, up to the 500th order harmonic data can be measured and saved simultaneously. The data update rate can be selected from nine options from 50ms to 20s. The perspective of the efficient use of energy is boosting demand for inverters to convert 50Hz or 60Hz AC power to DC power, grid connection controllers to control reverse power flow occurring due to excess power, and battery chargers/dischargers. The WT1800 is capable of simultaneously measuring the harmonic distortion of the input and output current of these devices. Challenging the common wisdom that "harmonic measurement is limited to a single line," the WT1800 is capable of performing two-line simultaneous harmonic measurements. The WT1800 is also capable of measuring up to the 500th order harmonic even at high fundamental frequencies such as a 400Hz frequency. This device is the ideal tool for engineers to ac-

curately measure power characteristics and efficiency of electrical devices. All the data are presented in a non-dimensional form and technical data of the battery emulator, power converter and the electrical machine cannot be provided because of confidential reasons. The operating conditions are defined by V_{dc} of the battery emulator, n_{MGU}, T_{MGU} of the MGU and f_{sw} of the power converter. The experimental power converter dissipation are obtained by subtracting the power measured at the AC side to the one obtained at the DC side. In the plots, the * is used as superscript to indicate that the aforementioned magnitudes are represented in a non-dimensional form. Fig.6.4(a)

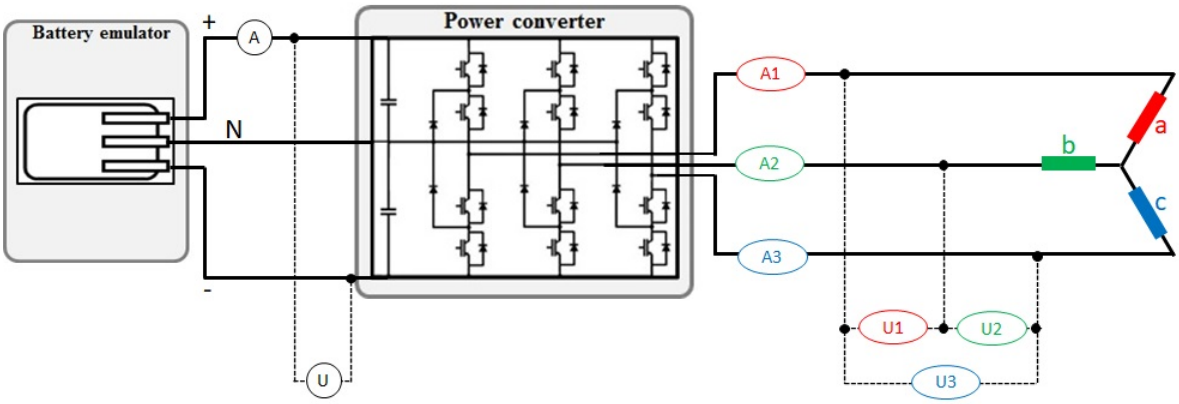

Figure 6.3 Schematic representation of the experimental set-up

shows the variation in PC power losses versus the current (i.e. T_{MGU}) at fixed V_{dc} and n_{MGU}. As expected, the power losses is strongly affected by activation current values. In detail, the difference between numerical and experimental data is minimal in both boost phase ($I_A > 0$A, $T_{MGU} > 0$Nm) and recharge phase ($I_A < 0$A, $T_{MGU} < 0$Nm). In Fig. 6.4(b), f_{sw} sensitivity is presented. It is appreciable as the numerical tool is able to reproduce the PC behavior for boost and recharge operations. Moreover, the power losses are evaluated also as a function of V_{dc} and n_{MGU}. Fig. 6.5 shows the variation of PC losses versus V_{dc} and n_{MGU} at fixed current value. As expected, the power losses are slightly affected by V_{dc} increase and are almost constant as a function of n_{MGU} ($n_{MGU,1} < n_{MGU,2} < n_{MGU,3}$). Numerical and experimental data are in good agreement in both boost and recharge phases. In general, the differences between numerical and experimental data remained into a range of $\pm$ 5% and they can be partially ascribed to error measurements and devices characteristics production dispersion. Moreover the analytical model is also affected by uncertainty due to the fact that the losses caused by GDB any passive components such as DC link capacitors are neglected. A representation of the percentage error between numerical and experimental data are reported in Figs. 6.6 and 6.7. In particular, Fig. 6.6(a) reports the percentage error

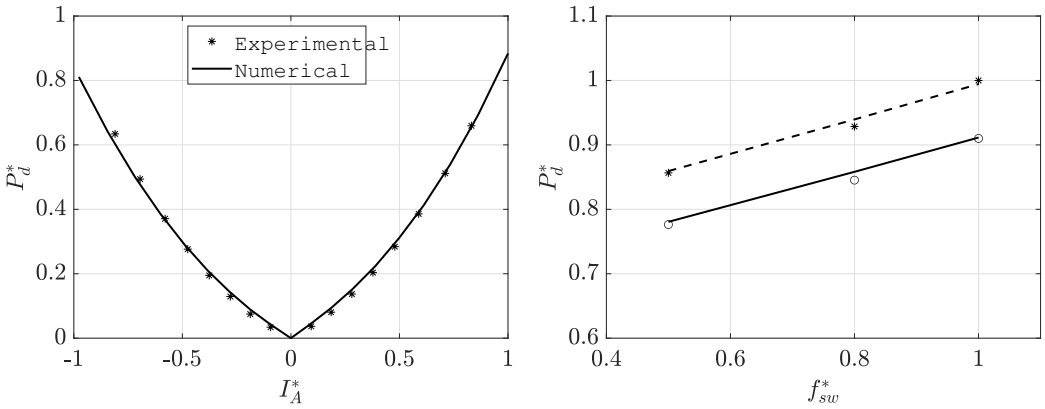

Figure 6.4 Power losses comparison: (a) effect of the electric current on the power losses, (b) effect of switching frequency on the power losses: the continuous line represents the numerical data in boost conditions, the circles represent the experimental data in boost conditions, the dashed line represents the numerical data in recharge conditions and the stars represent the experimental data in recharge conditions

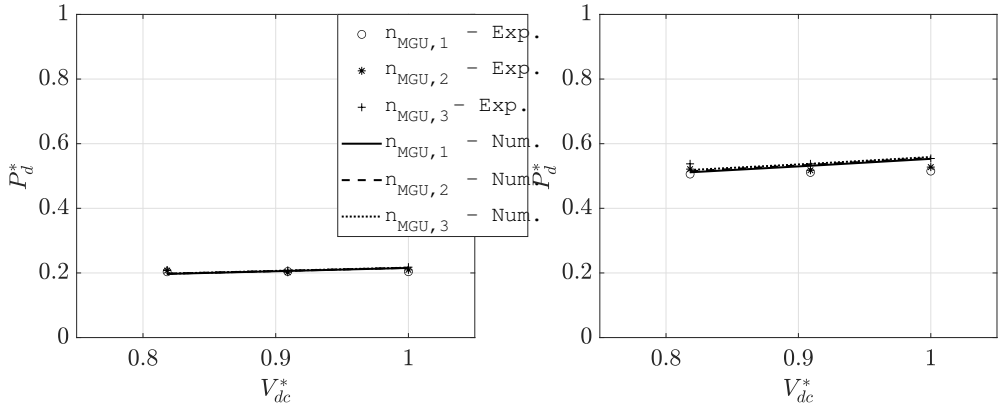

Figure 6.5 Power losses as a function of V_{dc} and n_{MGU}: in the left picture, boost conditions are reported, while in the right picture, recharge conditions are reported

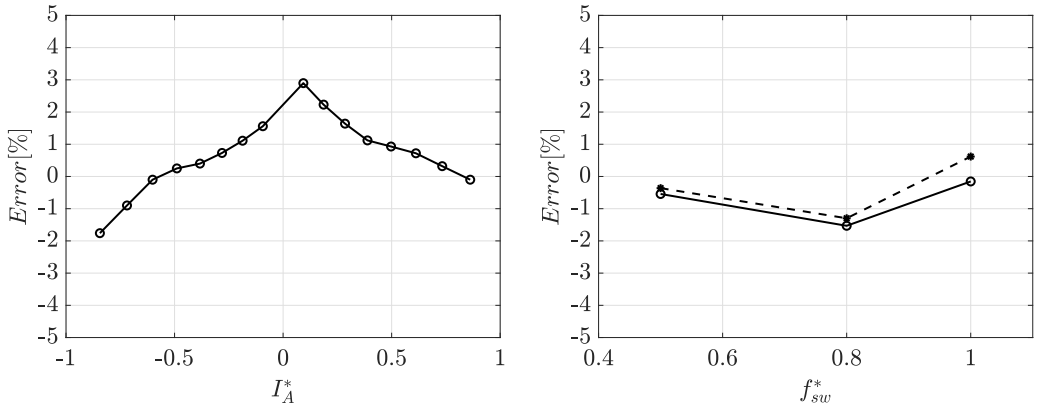

(a) (b)

Figure 6.6 (a) percentage error of the power losses as a function of the electric current, (b) percentage error of the power losses as a function of the switching frequency: the continuous line represents the error in boost conditions and the dashed line represents the error in recharge conditions

between numerical and experimental power dissipation as a function of the electric current. Fig. 6.6(b) shows the percentage error as a function of the switching frequency in boost and recharge conditions. Finally, 6.7 provides the percentage error evolution as a function of V_{dc} and speed. On the basis of the results summarized above, the simulation tool showed a good capability in reproducing the overall PC behavior. To complete the validation, also literature power losses model is considered. Hafezi et al. [6] proposed a numerical model based on polynomial approximation. The simulation results are compared also against Semisel [64] simulations. The analysis is performed on SEMIKRON "SKM400GB12T4" power module. To compare the losses calculation methods, a single-phase DC to AC inverter model is used. The PC is controlled at f_{sw} = 5kHz, the AC voltage generator to supply 230V with a power factor of 0.9. The present simulation tool based on look-up table approach shows similar results to the ones obtained by [6] and by Semisel simulations. Switching and conduction losses comparison among models are reported in Tables 6.1 and 6.2. In the first column, the test conditions are reported in terms of bus DC voltage and load RMS current.

6.3.2 Time-dependent conditions

The developed tool is validated also by considering time dependent conditions. In Fig. 6.8, V_{dc}, T_{MGU}, and n_{MGU} input profiles are reported in non-dimensional form for confidential reason. During the test, f_{sw} is kept constant. The analysis is conducted on

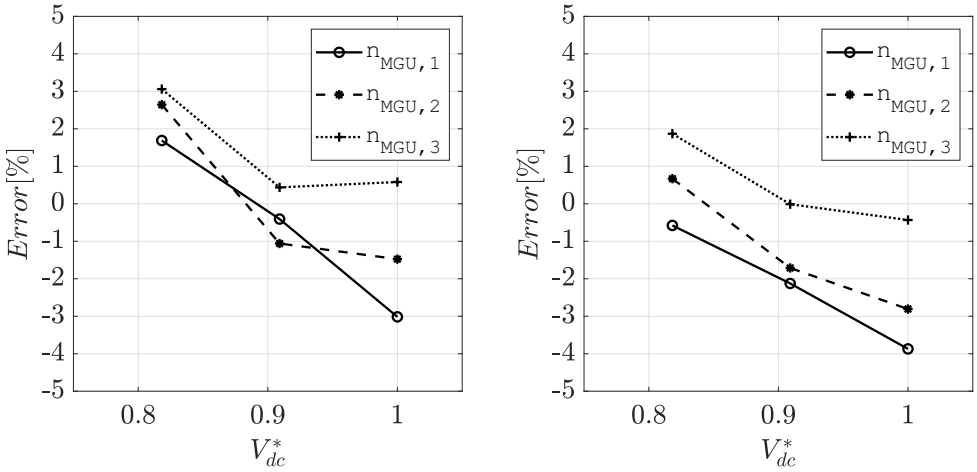

Figure 6.7 The percentage error of the power losses are plotted as a function of V_{dc} and n_{MGU}: in the left picture, boost conditions are reported, while in the right picture, recharge conditions are reported

Table 6.1 Switching losses comparison

IGBT-DIODE	Semisel [6] [64]	Hafezi et al. [6]	Tool	
500V, 100A	20.00-5.96	22.30-7.81	24.50-7.77	W
500V, 300A	71.00-22.00	63.28-26.76	68.60-20.60	W
700V, 100A	32.00-7.76	31.93-8.93	36.29-9.10	W
700V, 300A	118.00-31.00	92.55-32.34	110.50-27.60	W

Table 6.2 Conduction losses comparison

IGBT-DIODE	Semisel [6] [64]	Hafezi et al. [6]	Tool	
500V, 100A	40.00-21.00	38.89-18.02	40.50-19.40	W
500V, 300A	193.00-82.00	179.90-74.42	196.60-74.01	W
700V, 100A	36.00-26.00	35.34-22.64	35.90-28.90	W
700V, 300A	177.00-102.00	164.40-94.25	173.90-110.90	W

the same set-up configuration described previously. Both boost and recharge conditions are considered, and power losses comparison is shown in Fig.6.9. The numerical data appears well correlated against the experimental ones. The electro-thermal tool show a good reproduction of the power losses evolution through a dynamic drive cycle. Some mismatches between numerical and experimental data are ascertained when both n_{MGU} and T_{MGU} are interested by a drop. In HEV application, the electrical

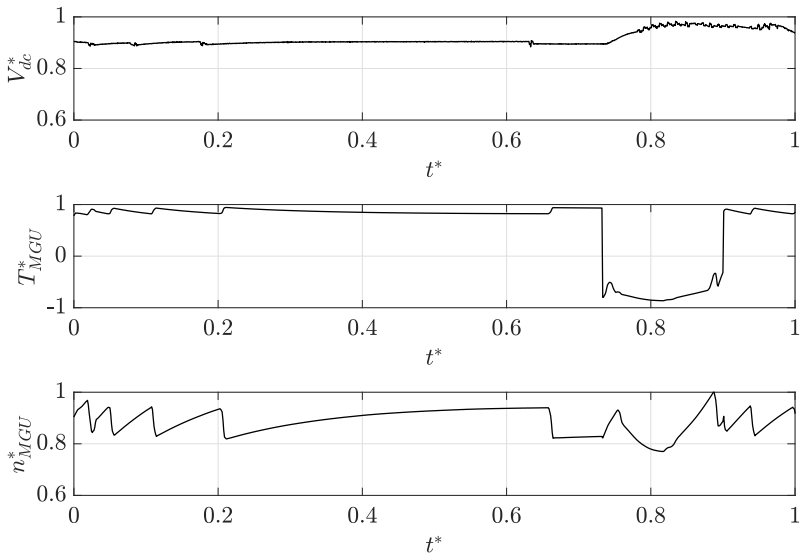

Figure 6.8 V_{dc}, T_{MGU}, and n_{MGU} dynamic profiles

machine is coupled with an internal combustion engine. Therefore, also the speed and the torque of the MGU are affected by gearshifts. It is also clear that the power losses experimental profile is affected by noise, but this is due to measuring instruments and environmental conditions. With this analysis, the accuracy of the electro-thermal tool is assessed.

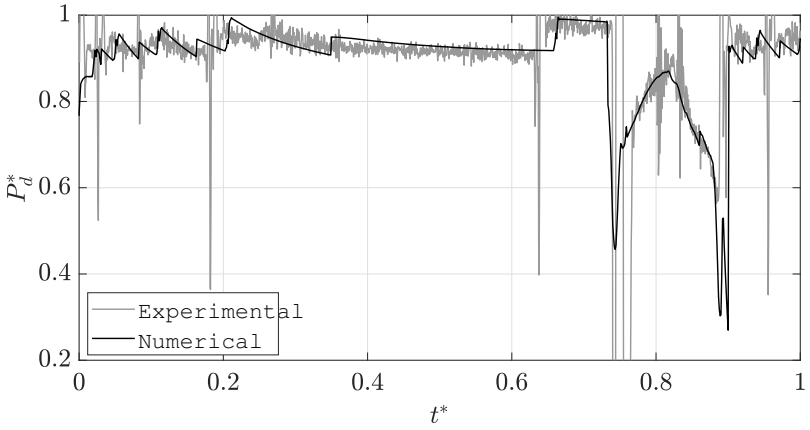

Figure 6.9 Comparison between experimental and numerical power losses

6.4 Power Modules presentation

In the present study, the proposed simulation approach is used to study three-phase PC configurations equipped by different power module typologies. In detail, four different PCs configurations are considered: 2L Si IGBT3, 3L Si IGBT3, 2L Si-EDT2, and 2L SiC MOSFET:

- 2L Si-IGBT3 configuration [50] is equipped by Infineon FS400R07A1E3 [20] power module. It accommodates a 3-phase Six-Pack configuration of Trench-Field-Stop IGBT3 and matching emitter controlled diodes;
- 3L Si-IGBT3 [61, 19] is equipped by Semikron SKiM401MLI07E4 [23] power module. It has similar properties respecting to the previous Infineon module helping authors in evaluating the difference in inverter topology (2L versus 3L) on PC overall performance;
- 2L Si-EDT2 [65, 50] is equipped with Infineon FS820R08A6P2B [21] power module. It is an automotive Micro-Pattern Trench-Field-Stop cell design optimized for electric drive train applications;
- 2L SiC MOSFET is equipped with ROHM S4103 [22] power module. It is used in advanced power electronics circuits to achieve significantly higher levels of energy efficiency not achievable by conventional Si devices. SiC MOSFET is characterized by a low drain-source resistance.

Table 6.3 summarizes the main characteristics of the considered power modules. It is worth to say that other power modules and/or PC topologies can be selected to be investigated with the presented tool. For the ROHM S4103 power module, the nominal current is much lower than the other power modules. Therefore, more parallel devices need to be adopted respecting to the other considered devices. For the current case, 8 parallel chips are adopted.

6.5 Steady-state simulations

In general, PC operating conditions are defined by the V_{dc}, T_{MGU}, n_{MGU}, and f_{sw}. Table 6.4 summarizes the steady-state operating conditions investigated. All of these points form a $13 \times 5 \times 4$ simulation matrix, hence 260 points are investigated for all power modules considered. One of the strongest point of the developed test bench is the short execution time, since only ≈ 0.3s are needed for each detected point. In this way,

Table 6.3 Power modules

	Configuration	V_{CE} V	I_{CE} A
Infineon FS400R07A1E3_S7 [20]	2L Si-IGBT3	700	400
Semikron SKiM401MLI07E4 [23]	3L Si-IGBT3	650	400
Infineon FS820R08A6P2B [21]	2L Si-EDT2	750	820
		V_{DSS} V	I_D A
ROHM S4103 [22]	2L SiC MOSFET	1200	95

the whole simulation matrix is simulated in 0.3s $\times$ 260 $\approx$ 78s. Similarly, to extend the simulation activity to all power modules, the execution time is around 312s. Moreover, this allows to perform the investigation without performing costly experimentation activities. Fig. 6.10(a) shows the MGU mechanical power map, the power limit is of 80kW. MGU boost/recovery phases are associated to positive/negative torque values respectively. Fig. 6.10(b) shows the current map associated to the MGU mechanical power map. For the considered simulation matrix, there is no dependency of the current by the speed, this means that MGU work only by following MTPA control [42]. For the MGU adopted, the electrical parameters cannot be provided to preserve confidentiality. Moreover, also heat sink and thermal model information cannot be provided for confidential reasons.

Table 6.4 Simulation matrix

V_{dc} V	T_{MGU} Nm	n_{MGU} kRPM	f_{sw} kHz
500	0, $\pm$5,$\pm$10,$\pm$15,$\pm$20,$\pm$25,$\pm$30	15,20,25,30,35	10,20,30,40

6.5.1 Results

In this section, the results of the four power modules are presented in terms of power losses. In detail, results are firstly presented at fixed switching frequency (20kHz) and secondly at variable switching frequency. Finally, an investigation on single power semiconductor behavior is presented.

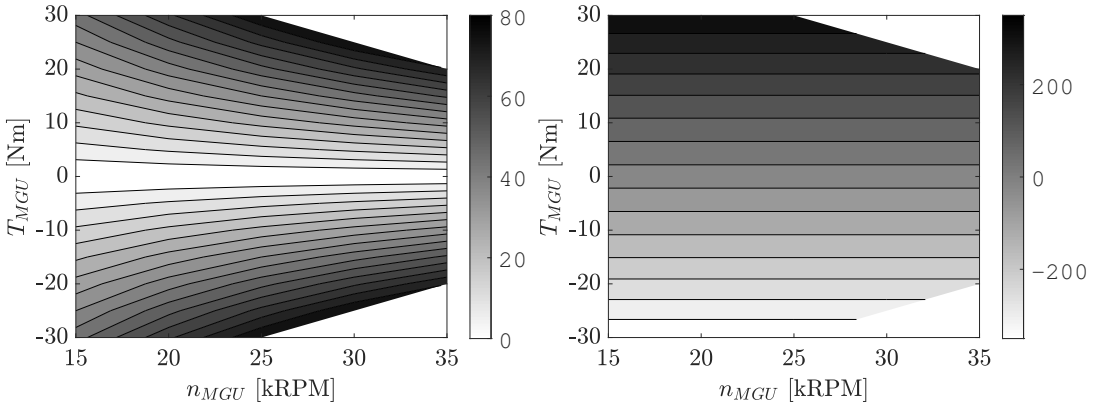

(a) (b)

Figure 6.10 (a) Mechanical power map [kW], (b) I_A map [A]

Power losses at f_{sw} = 20kHz

Figs. 6.11 shows the power losses obtained for the four considered power modules at constant switching frequency equal to 20kHz. Figs. 6.11(a) and 6.11(b) show the power module losses as a function of the torque at 25kRPM and 30kRPM respectively. In both cases, 3L IGBT3 [23] is characterized by the highest power dissipation at maximum and minimum torque values. It is due of the highest number of power semiconductors characterizing this scheme respecting to 2L solution. As a matter of fact, this is not true for each switching frequency level. 2L IGBT3 [20] and 2L EDT2 [21] show a very similar behavior in terms of power losses. Exploring their datasheets, 2L IGBT3 [20] shows better performance in terms of switching losses than 2L EDT2 [21], but higher conduction losses. For the specific case, the two effects cancel each other and the 2L EDT2 total power module losses, resulted almost equal to the 2L IGBT3 module. About the 2L SiC [22], this technology outperforms all the other configurations. It is possible thanks to the presence of chips in parallel (8 for the current case). The paralleling of multiple devices provides a reduction of the total conduction losses. At fixed speed, the losses increase with the MGU torque because it resulted in an increased current flowing throughout the semiconductors. About MGU speed influence (for a given torque) on the power losses budget, it is negligible because the electric current varies only with the torque as seen in Fig. 6.10(b).

Switching frequency sensitivity

The switching frequency sensitivity is here discussed. The results are plotted as a function of I_A, and only the case of n_{MGU} equal to 25kRPM is proposed. As expected,

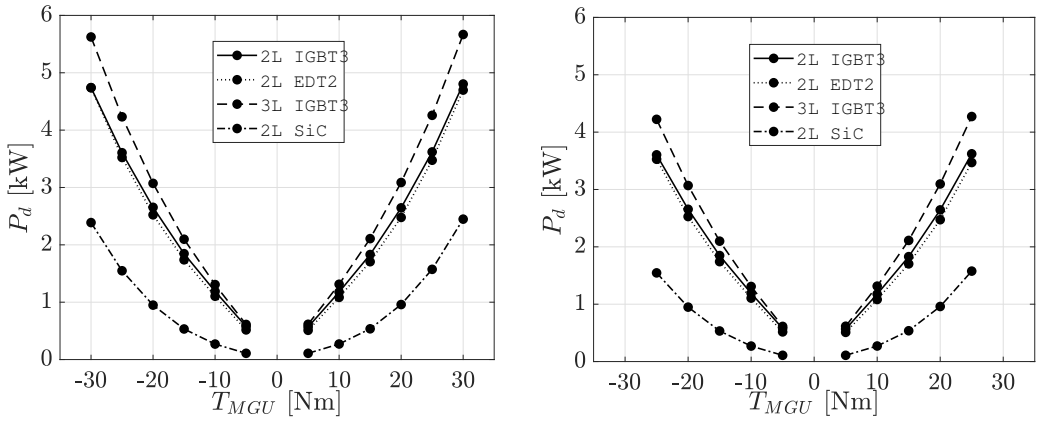

Figure 6.11 Power losses evaluated at f_{sw} = 20kHz: (a) n_{MGU}= 25kRPM, (b) n_{MGU} = 30kRPM

the growing switching frequency leads to an efficiency reduction of PC. In Fig. 6.12(a), the 2L IGBT3 technology results are presented. The power losses ranges from ≈ 3.5kW (f_{sw} = 10kHz) to 7.5kW (f_{sw} = 40kHz) at I_A equal to 350A. The EDT2 technology (Fig. 6.12(b)) results to be more sensitive to the f_{sw}: the power losses is around 3kW for f_{sw} = 10kHz and above 8kW at f_{sw} = 40kHz. This effect is associated to the higher E_{on}, E_{off} and E_{rr} for the EDT2 than the IGBT3 technology. The 3L power converter (Fig. 6.12(c)) is more dissipative than 2L IGBT3 and 2L EDT2 at low switching frequency. As the switching frequency increases, the performance of the 3L configuration tends to be better than the 2L IGBT configuration. The main benefit of the 3L topology came from the reduced switching losses since the commutation voltage is $V_{dc}/2$ [66]. Finally, the 2L SiC (Fig. 6.12(d)) power converter shows the lowest dissipation level for the whole range of switching frequency. The main reasons can be ascribed to the presence of chips in parallel which significantly reduced the power losses. The parallel chips modeling are well explained by Nishizawa et al. [67]. For the specific case, the body diode commutation losses are already taken into account in the power MOSFET as reported directly in the datasheet [22]. A detailed study on the switching losses modeling based on datasheet parameters is poposed by Christen and Biela [60]. Further studies on SiC MOSFETs losses characterization are presented in [58, 59]. To provide a clear comparison among the PC configurations, a representation of P_d for a fixed point is reported in Fig. 6.13 both for boost and recharge conditions. The results are below discussed:

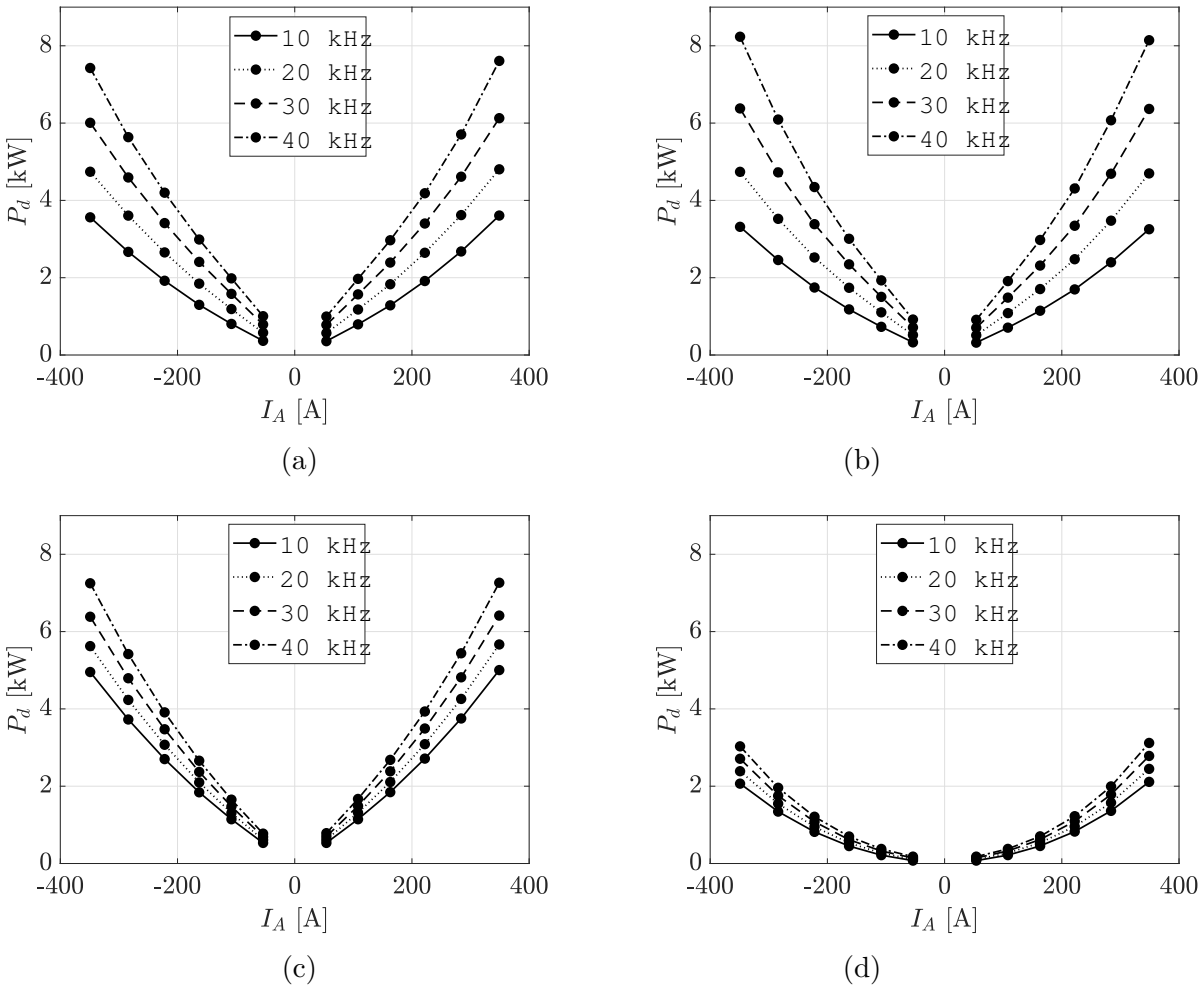

Figure 6.12 Power losses as a function of f_{sw} at 25kRPM: (a) 2L IGBT3, (b) 2L EDT2, (c) 3L IGBT3, (d) 2L SiC

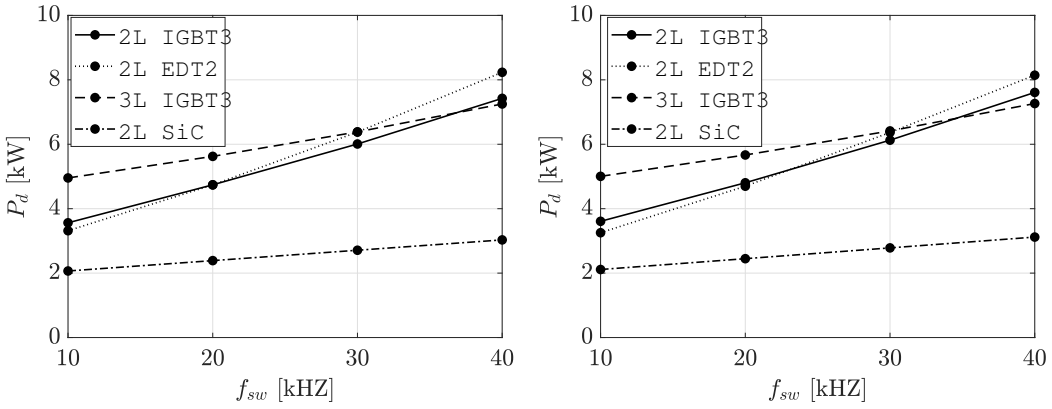

Figure 6.13 Power losses, n_{MGU} = 25kRPM: (a) Recharge condition: I_A= -350A, T_{MGU} = -30Nm, (b) Boost condition: I_A = 350A, T_{MGU} = 30Nm

- *Recharge* (I_A = -350A, T_{MGU} = -30Nm): In Fig. 6.13(a), it is shown that the EDT2 curve has the largest slope than other configurations. The 2L IGBT3 and the 3L IGBT3 slopes are lower. Below 20kHz, the 2L IGBT3 power module losses are superior than the 2L EDT2. At 30kHz, the 3L IGBT3 efficiency overtakes the 2L EDT2. Moreover, the 2L IGBT3 and 3L IGBT3 curves cross between 30kHz and 40kHz. The 2L SiC shows the highest effciency for the whole range.
- *Boost* (I_A = 350A, T_{MGU} = 30Nm): In Fig. 6.13(b) is shown that the 2L IGBT3 and 2L EDT2 curves intersect at 20kHz. Above this f_{sw}, the 2L IGBT3 technology outperforms the 2L EDT2. Moreover, between 30kHz and 40kHz the 2L topology becomes less efficient than the 3L architecture. The 2L SiC configuration results to be the most efficient solution.

Finally, differences between IGBT3 and EDT2 in a 2L topology are very small. It is suggested to prefer the EDT2 solution with respect the IGBT3 for low switching frequency application. 3L topology deserves to be considered when f_{sw} reaches high values, but SiC MOSFETs are preferred to easily manage power converter losses.

Power losses on power semiconductors

This paragraph aims to investigate separately the conduction and switching dissipation affecting power semiconductors. Firstly, the chip dissipation are compared just for the 2L topology converter. In Fig. 6.14, an evaluation of the transistor T1 (T2) for boost condition, where T_{MGU} is of 30Nm, n_{MGU} is equal to 25kRPM and the I_A is of 350A,

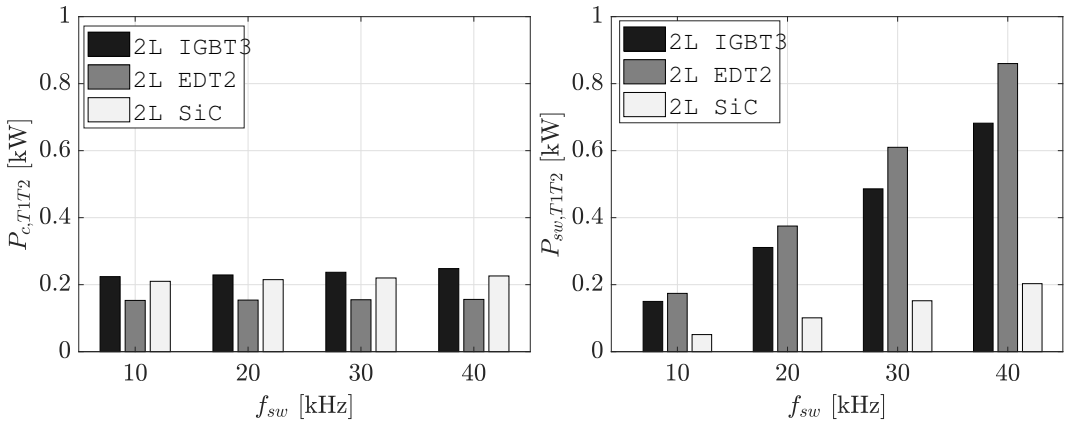

Figure 6.14 T_{MGU} = 30Nm, n_{MGU} = 25kRPM, I_A = 350A: (a) Conduction losses, (b) Switching losses

is proposed. It is clear that the EDT2 technology performs better than the IGBT3 in terms of conduction losses (Fig. 6.14(a)). Furthermore, the EDT2 performance are more strongly affected by the switching losses (Fig. 6.14(b)). Moreover, the SiC switching losses are significantly lower with respect other technologies. As expected, the increase in switching frequency does not affect significantly the conduction losses. In Fig. 6.15, an evaluation of the diodes D1 (D2) for recharge condition, where T_{MGU} is equal to -30Nm, n_{MGU} is equal to 25kRPM and the I_A is of -350A, is provided. Since the SiC power module is equipped by a power MOSFET with its body diode, only the EDT2 and IGBT3 technologies are compared. Basically, body diode losses are not easy to predict by numerical simulation, and most times they are neglected. As expected, the conduction dissipation are larger for the IGBT3 power diodes (Fig. 6.15(a)). The impact of switching losses is more evident on EDT2 configuration (Fig. 6.15(b)). As already stated, EDT2 technology is preferable at lower switching losses ($f_{sw} < 20$kHz). Above $f_{sw} > 20$kHz, the IGBT3 solution can be taken into consideration.

Since the 3L NPC configuration has a different chips number than the 2L, it needs to be treated separately. The power semiconductor devices are investigated during inverter and rectifier operations as shown in Fig. 6.16. During inverter operations (Fig. 6.16(a)), only the transistors and the clamping diode are affected by power losses. Moreover, it is appreciable that the transistor T1 (T4) is the most sensitive power semiconductor to the switching frequency. During recharge phase (Fig. 6.16(b)), D1 (D4) and D2 (D3) show dissipation as expected. The transistor losses of T1 (T4) are

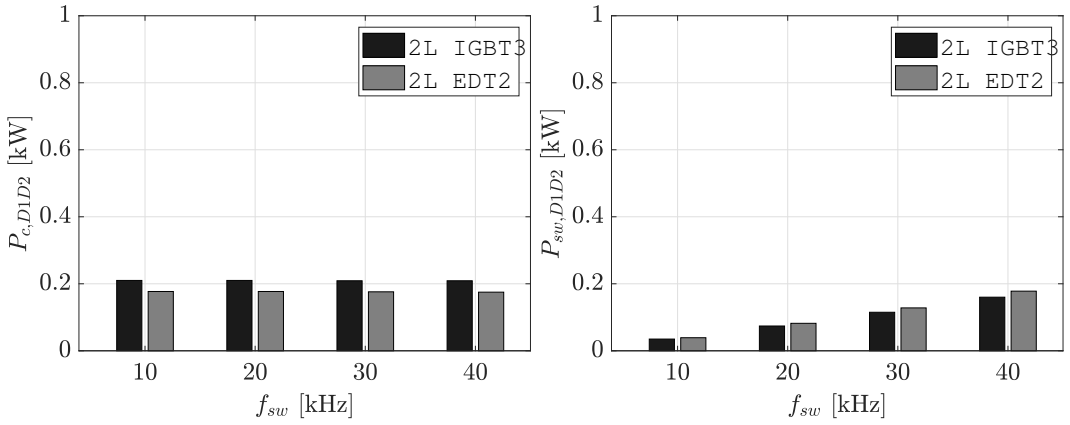

Figure 6.15 T_{MGU} = -30Nm, n_{MGU} = 25kRPM, I_A = -350A: (a) Conduction losses, (b) Switching losses

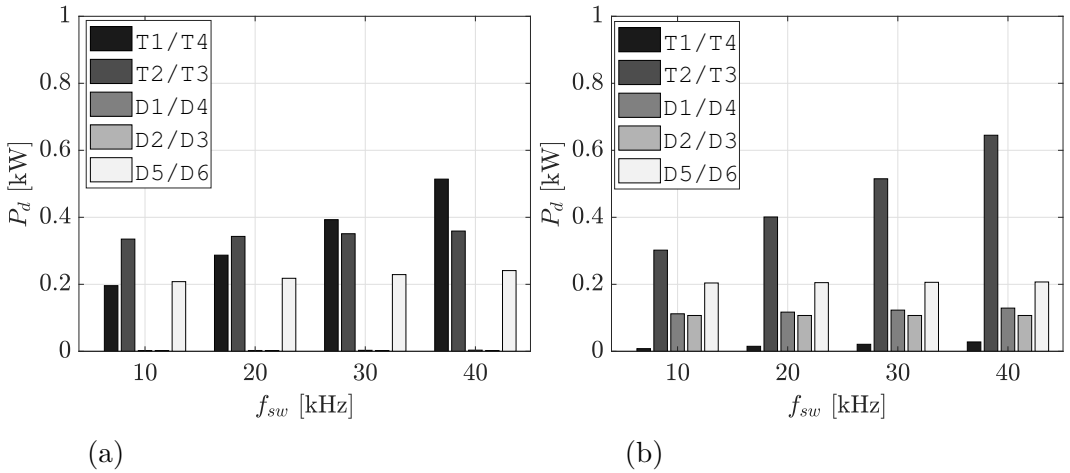

Figure 6.16 Semiconductor power losses: (a) T_{MGU} = 30Nm, n_{MGU} = 25kRPM, I_A = 350A, (b) T_{MGU} = -30Nm, n_{MGU} = 25kRPM, I_A = -350A

negligible with respect to T2 (T3) and they show an evident dependency with f_{sw}. In general, the transistors are more sensitive to the f_{sw} than the power diodes. This is due to the higher switching energy (E_{on}+E_{off} $\approx$ 50mJ) for the transistors than the diodes (E_{rr} $\approx$ 3mJ).

On the basis of the presented results, it can be easily individuated the power semiconductor which is affected by the highest power dissipation. However, in order to have a wider idea of the thermal flux involved, also the chip area needs to be taken into account. Since the chips area is usually in the order of cm^2, and power losses are in the order of the hundred of W, the heat flux interesting the semiconductor is generally very high. This is an important information for the study of the power module cooling system. It plays an important role, in fact it is necessary to ensure reliability and high performance of such devices. In the following chapter, the cooling of power semiconductor is accurately treated.

6.6 Time-dependent simulations

Power modules performance are assessed also by considering dynamic conditions. Two drive cycles characterized by T_{MGU}, and n_{MGU} profiles are considered and reported in Fig. 6.17. For sake of simplicity the V_{dc} is constant and equal to 500V. In terms of f_{sw}, the same values reported in Table 6.4 are considered. T_{MGU}-n_{MGU} maps of the

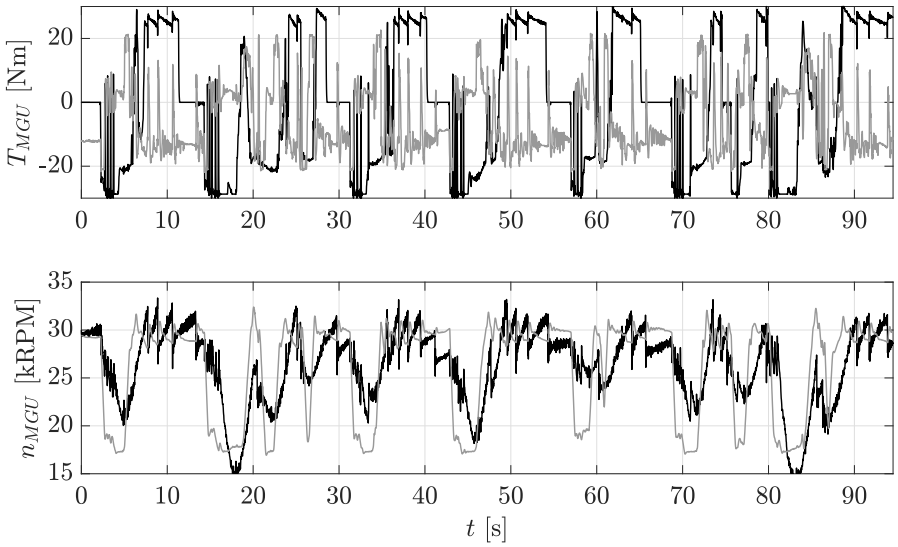

Figure 6.17 The black profiles of T_{MGU} and n_{MGU} refers to the Cycle 1, while the gray ones refers to the Cycle 2

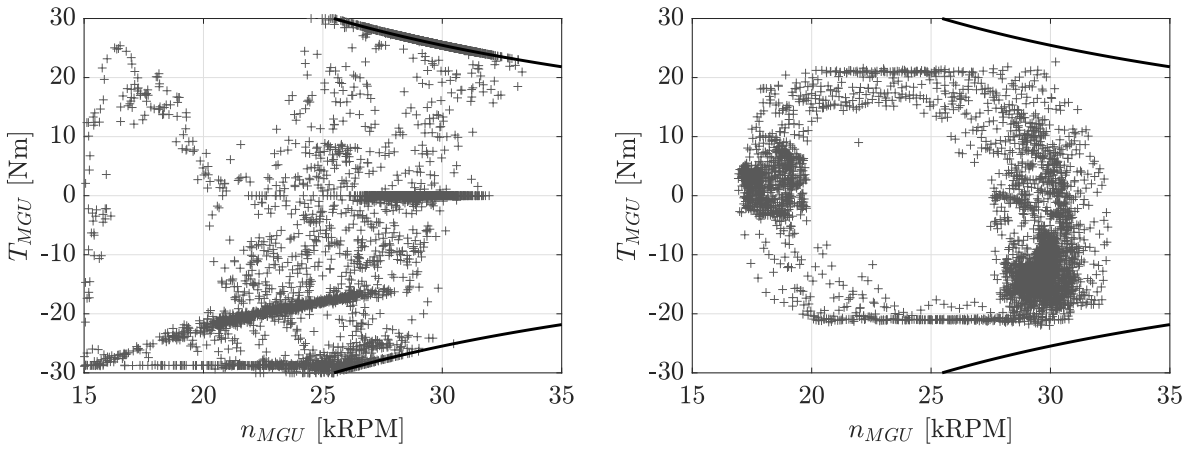

Figure 6.18 Torque-Speed map: (a) Cycle 1, (b) Cycle 2

involved cycles are reported in Figs. 6.18(a) and 6.18(b). To quantify the impact of the drive cycle on the PC behavior, an innovative procedure is proposed and discussed. To obtain a detailed analysis of the time spent in a given range of T_{MGU} and n_{MGU}, the Usage time is defined and introduced. Let us introduce ψ and δ:

$$\psi = [\psi_1, ..., \psi_{i-1}, \psi_i, \psi_{i+1}, ..., \psi_\alpha] \tag{6.24}$$

$$\delta = [\delta_1, ..., \delta_{j-1}, \delta_j, \delta_{j+1}, ..., \delta_\beta] \tag{6.25}$$

They define the discretisation of T_{MGU} and n_{MGU}. T_{MGU} ranges from -30Nm (ψ_1) to 30Nm (ψ_α) while n_{MGU} ranges from 15kRPM (δ_1) to 35kRPM (δ_β), see Table 6.4. The length of ψ is $\alpha = 31$ and the difference between ψ_i and ψ_{i+1} is of 2Nm, for i = 1,...,α-1. For δ, its length is $\beta = 21$ and the difference between δ_j and δ_{j+1} is of 1kRPM, for j = 1,...,β-1. For the current simulation, the step time adopted is $\Delta t = 0.01$s and the period of each drive cycle is $\Theta = 94.5$s. Therefore, the length of vectors t, T_{MGU} and n_{MGU} is $s = \Theta/\Delta t + 1$. Hence, it can be written:

$$t = [t_1, ..., t_k, ..., t_s] \tag{6.26}$$

$$T_{MGU} = [T_{MGU,1}, ..., T_{MGU,k}, ..., T_{MGU,s}] \tag{6.27}$$

$$n_{MGU} = [n_{MGU,1}, ..., n_{MGU,k}, ..., n_{MGU,s}] \tag{6.28}$$

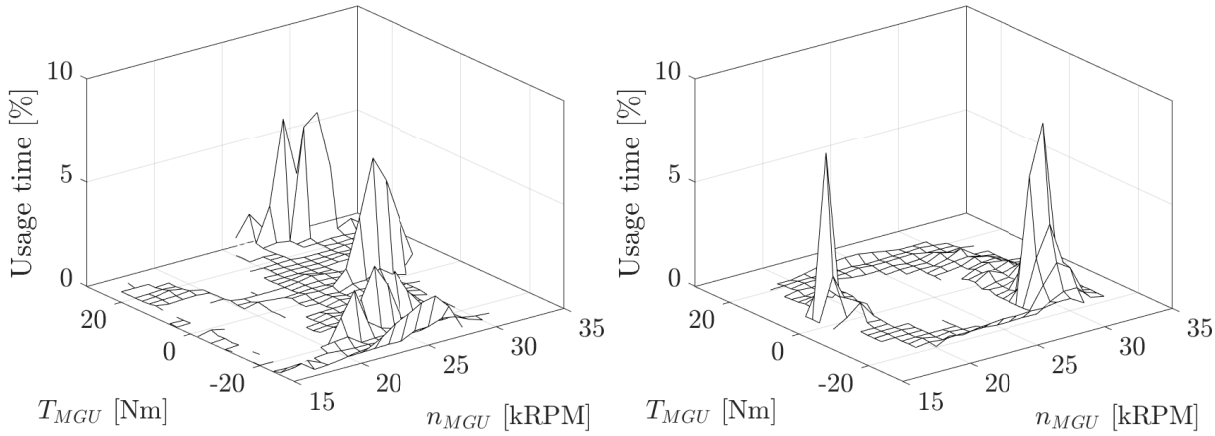

Figure 6.19 Usage time map: (a) Cycle 1, (b) Cycle 2

It is now possible to define the Usage time (U_{ij}) as follows:

$$U_{ij} = \frac{\sum_{k=1}^{s-1}(t_{k+1} - t_k)}{\Theta} \tag{6.29}$$

if $\psi_i \leq T_{MGU,k} < \psi_{i+1}$ and $\delta_j \leq n_{MGU,k} < \delta_{j+1}$. On the contrary $U_{ij} = 0$. It is easy to image as $\Delta t = t_{k+1} - t_k$ for $k = 1, ..., s-1$. U_{ij} is a useful index which quantifies the percentage of time spent by the PC in a given region of torque and speed. Since U_{ij} must be computed for i = 1,...,$\alpha - 1$ and j = 1,...,$\beta - 1$, a $(\alpha - 1) \times (\beta - 1)$ matrix can be defined. This matrix is defined as Usage time map. In Figs. 6.19(a) and 6.19(b), a Usage time map representation for both cycles is reported. It represents the distribution of the Usage time in detail. In the plots, each point such that $U_{ij} = 0$ is removed since it does not represent a working condition. The sum of all elements of the Usage time map matrix must be equal to 1. The Usage time map shows the region with the highest and lowest usage level. In this way, potentially critical operating conditions can be easily individuated in terms of duration. For Cycle 1, the highest Usage time concentration is located on the power limit trajectory. For Cycle 2, the highest usage conditions are assessed in recovery region above the minimum power achievable. In terms of execution time, less than 20s are employed to simulate each drive cycle.

6.6.1 Results

Power losses at f_{sw} = 20kHz

To evaluate the drive cycles impact on the power converter behavior, the Usage time must to be linked with the PC losses. To do that, let us define P_{ij} as follow:

$$P_{ij} = \frac{\sum_{k=1}^{s} P_{d,k}}{\mathbf{K}} \tag{6.30}$$

if $\psi_i \leq T_{MGU,k} < \psi_{i+1}$ and $\delta_j \leq n_{MGU,k} < \delta_{j+1}$. On the contrary $P_{ij} = 0$. $P_{d,k}$ represents the k-th element of the power dissipation vector. $\mathbf{K}$ is the number of the element found in the considered interval. P_{ij} is computed for $i = 1, ..., \alpha - 1$ and $j = 1, ..., \beta - 1$, so a $(\alpha - 1) \times (\beta - 1)$ P_d matrix can be defined. P_{ij} is the average value of the power converter losses at the i-th, j-th position of the introduced matrix. In Figs. 6.20(a), 6.20(b), 6.20(c) and 6.20(d) the power losses distribution for Cycle 1 of 2L IGBT3, 2L EDT2, 3L IGBT3 and 2L SiC configurations are respectively represented. Also in this case, the points where $P_{ij} = 0$ is true are removed from the graphs. This representation allows to obtain a clear overview of the PC behavior over the cycle. The P_{ij} distribution confirms that 2L IGBT3 and 2L EDT2 behave similarly. Both configurations are less dissipative than the 3L IGBT3 solutions. The 2L SiC results to be clearly the most efficient solution for each point covered in the involved cycle. As a matter of fact, for each configuration, it is possible to detect an increase of power dissipation for high torque level. In order to obtain a clear quantification of PC performance on the basis of the considered drive cycles, a link between the Usage time and P_d matrix is introduced. Let us define $P_{d,cycle}$ as reported by the following formula:

$$P_{d,cycle} = \sum_{i=1}^{\alpha-1} \sum_{j=1}^{\beta-1} P_{ij} \cdot U_{ij} \tag{6.31}$$

It represents the weighted average of PC losses over the given drive cycle. In Table 6.5, $P_{d,cycle}$ for the two cycles involved are reported. It is clear that the cycle affects the power losses. In general, Cycle 1 leads an higher dissipation level with respect Cycle 2. This can be ascribed to the higher Usage time at higher torque level. $P_{d,cycle}$ allows to obtain an averaged losses value for the load cycle involved. The Power losses and Usage time maps consent a detailed investigation of power modules behavior. Critical working conditions can be easily detected in terms of losses and duration. This methodology allows to avoid undesired events and to preserve PC lifetime and performance.

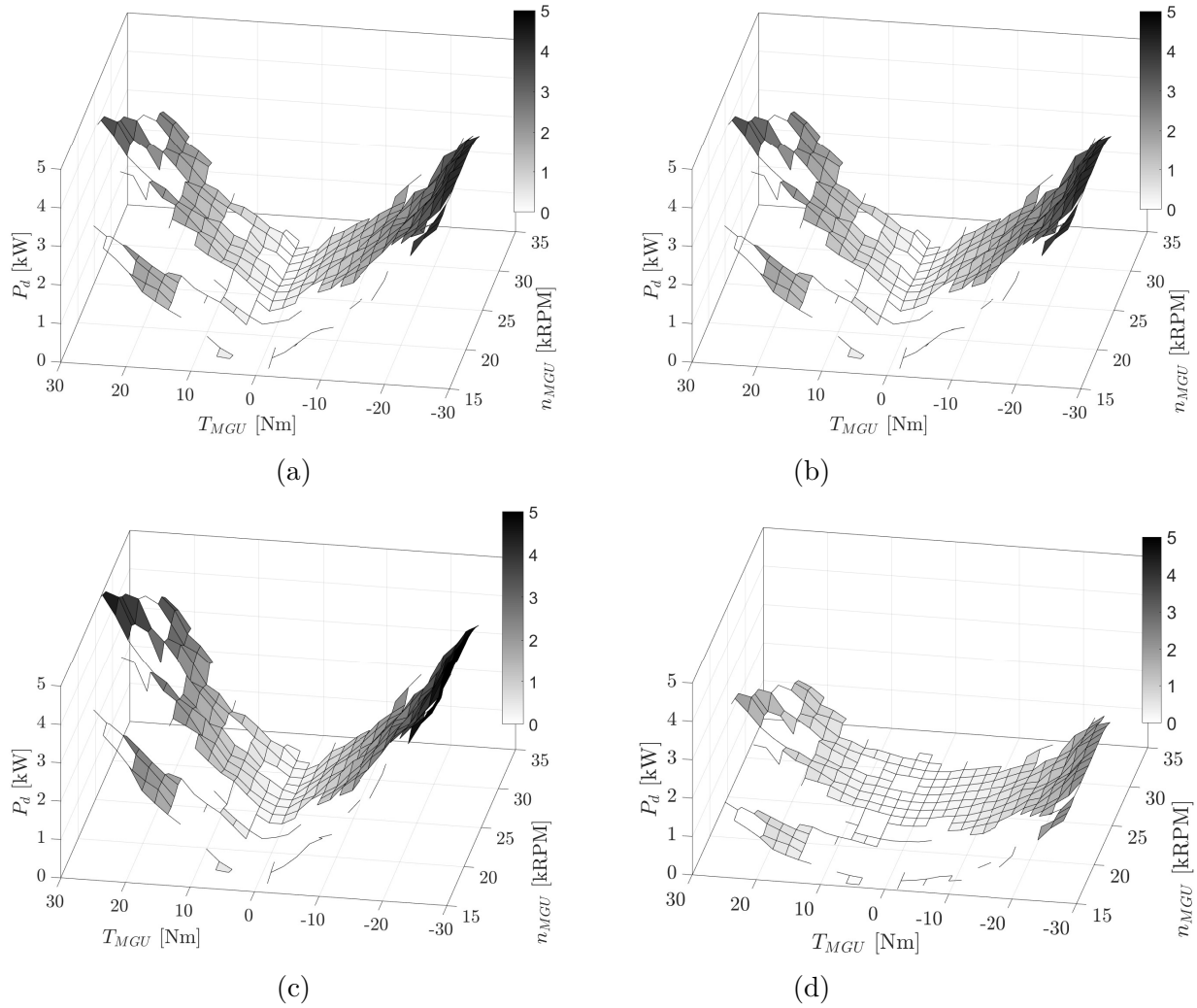

Figure 6.20 Power losses at f_{sw} = 20kHz: (a) 2L IGBT3, (b) 2L EDT2, (c) 3L IGBT3, (d) 2L SiC

Table 6.5 $P_{d,cycle}$

Configuration	2L IGBT3	2L EDT2	3L IGBT3	2L SiC
$P_{d,cycle}$	kW	kW	kW	kW
Cycle 1	2.31	2.22	2.80	1.08
Cycle 2	1.15	1.10	1.34	0.71

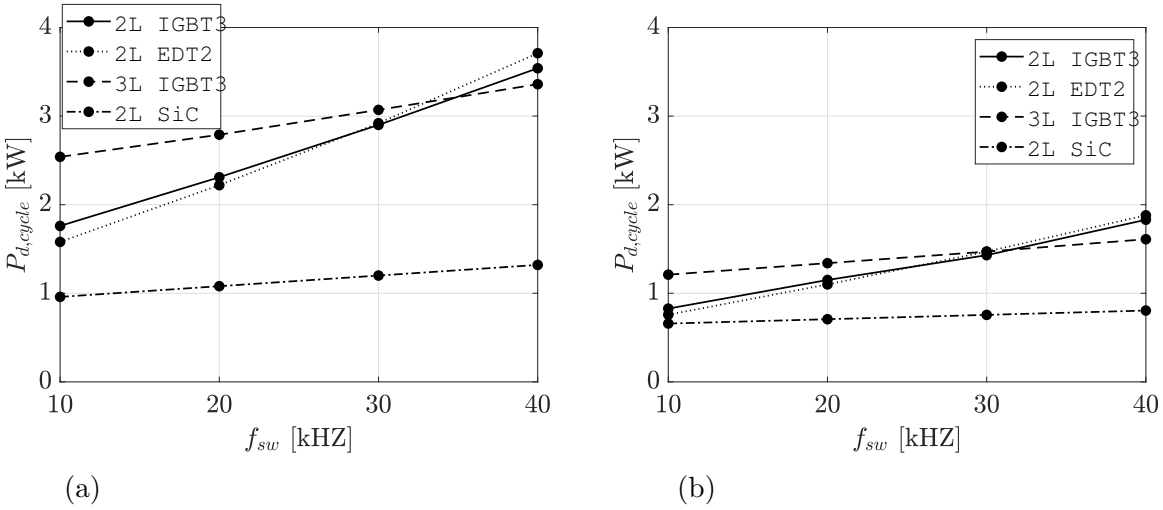

Figure 6.21 $P_{d,cycle}$ as a function of the switching frequency: (a) Cycle 1, (b) Cycle 2

Switching frequency sensitivity

The f_{sw} effect is explored also for the current case. Figs. 6.21(a) and 6.21(b) summarize $P_{d,cycle}$ as a function of f_{sw} for both cycles considered. The pictures show difference between the two cycles. The f_{sw} effect is stronger for Cycle 1: the torque level is globally higher with respect to the Cycle 2 torque level (for Cycle 1, MGU power limit curve is also covered). A similar behavior of the investigated configuration has been already obtained in Figs. 6.13(a) and 6.13(b). This confirms that the tool is capable of reproducing the PC behavior for a large range of operating condition. This makes the tool capable of driving the PC design process.

6.7 Discussion

In this chapter, an electro-thermal simulation tool is presented. It allows to accurately evaluate the performance of any PC configuration at low computational cost. Its accuracy is assessed through a validation procedure: experiments and literature results are considered. A detailed numerical study is performed by considering the following PC configurations: 2L IGBT3, 2L EDT2, 2L SiC and 3L IGBT3 technologies. Each of the above configurations are tested in 260 different steady-state conditions. In addition the power modules are also investigated over two dynamic drive cycles. The main results are summarized as follows:

- Power losses at f_{sw} = 20kHz: 2L IGBT3 and 2L EDT2 configurations behave in a very similar way. The 3L IGBT3 power converter is the most dissipative solution while the 2L SiC case showed the lowest dissipation level;

- Switching frequency sensitivity: considering the 2L IGBT3 and 2L EDT2 configurations, the conduction dissipation are larger for the IGBT3 power module while the switching losses are higher for the EDT2 configuration. The efficiency of the 3L IGBT3 solution is better than 2L IGBT3 and 2L EDT2 configurations at high f_{sw}. This is due to the reduced switching losses because the commutation voltage is $V_{dc}/2$. Finally, the 2L SiC power converter achieves the best performance. The main reason can be ascribed to the employment of parallel chips.

- Power losses on power semiconductor: The EDT2 technology performed better than the IGBT3 in terms of conduction losses. Furthermore, the EDT2 performance are more significantly affected by the switching losses. EDT2 technology is preferable at lower switching losses (f_{sw} below 20kHz). Above f_{sw} = 20kHz, the IGBT3 solution could be taken into consideration. SiC semiconductors show the best behavior for the whole f_{sw} range investigated.

- When considering the two real drive cycles, the introduction of Usage time maps allows to quantify the time spent in a given operational range. Moreover, the impact of any drive cycle on PC performance can be easily quantified by introducing $P_{d,cycle}$. Critical working conditions can be easily detected in terms of losses and duration. This methodology allows to avoid undesired events and to preserve PC lifetime and performance.

The presented numerical tool is very effective in the design procedure of PCs. A very wide operating conditions range can be investigated in a short time and detailed evaluation of PC behavior is provided bypassing costly experimentation campaign. Moreover, the presented methodology allows to identify potentially critical operating conditions. The tool can be furthermore developed to allow a multi-objective optimization of such devices with the aim to improve the PC behavior for determinate operating conditions or load cycles. Moreover, the performed analysis on single power semiconductor allows to detect which is the power density level involved. This information plays an important role in the choice of the cooling strategy of power electronics devices.

As previously said, the power semiconductor surface is in the order of cm^2. In paragraph 6.5.1, it is ascertained the power dissipation involving the chips for a number of operating conditions and a focus on the switching frequency sensitivity is clearly

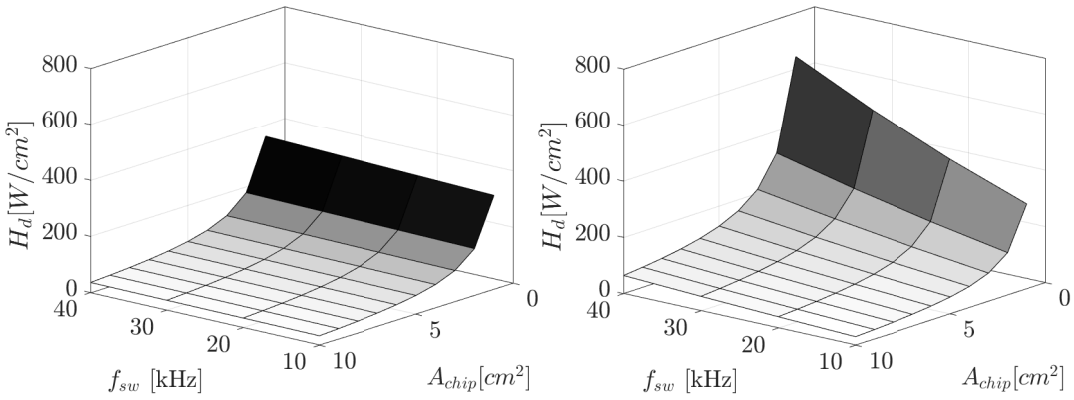

Figure 6.22 H_d distribution of T2 (T3) as a function of A_{chip} and f_{sw}: (a) T_{MGU} = 30Nm, n_{MGU} = 25kRPM, I_A = 350A (Boost), (b) T_{MGU} = -30Nm, n_{MGU} = 25kRPM, I_A = -350A (Recharge)

proposed. Let us focus on the 3L IGBT3 configuration. The semiconductor dissipation are reported in Figs. 6.16(a) and 6.16(b) for boost and recharge condition respectively. It is interesting to take into consideration just a transistor T2 (T3) and a diode D5 (D6) for example. As already seen, the T2 semiconductor is the most dissipative device in a 3L NPC PC topology, in addition it is also sensitive to the switching frequency. To obtain a representation of the heat flux density (H_d) which involves the power semiconductor, the power losses ($P_{d,T2T3}$) must be divided by its area. In this way, a clear evaluation of H_d can be provided. In Figs. 6.22(a) and 6.22(b), the H_d distribution as a function of chip area and switching frequency is proposed, in boost and recharge conditions respectively. It is clear as the chip area plays a crucial role for the thermal behavior of such devices. For $A_{chip} < 5\text{cm}^2$, H_d is high and an effectiveness cooling strategy must be adopted to ensure performance and reliability of semiconductors. Moreover, to reduce encumbrance of power electronic devices, chips will become even smaller during the next years. Therefore, a special effort on the heat sink equipping power conversion system will be necessary. In Figs. 6.23(a) and 6.23(b), the H_d distribution of D5 (D6) is presented. H_d is globally lower than the previous case, however the order of magnitude is the same. The same evaluation can be performed for any power semiconductor involved and for the different operating conditions explored. On the basis of these considerations, a thermal management system plays a very important role for the power semiconductors. It ensures performance and reliability of such devices. In the next chapter, a cooling strategy for power converter device is deeply treated.

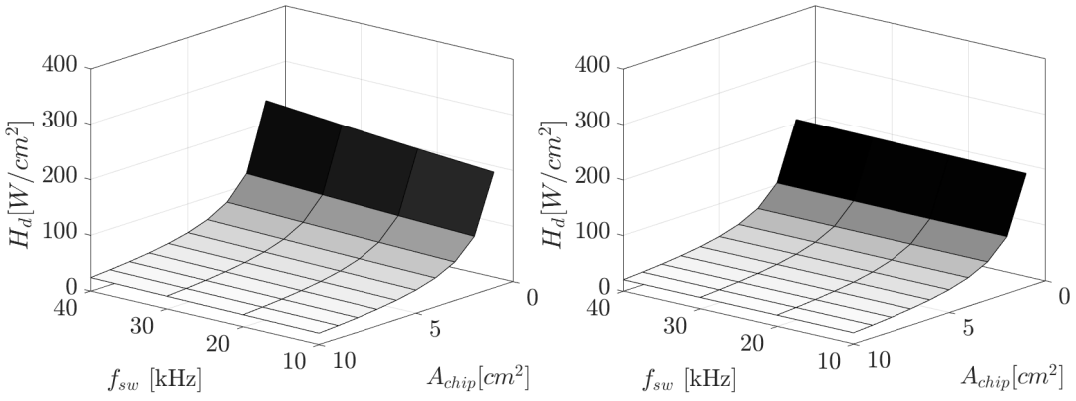

Figure 6.23 H_d distribution of D5 (D6) as a function of A_{chip} and f_{sw}: (a) T_{MGU} = 30Nm, n_{MGU} = 25kRPM, I_A = 350A (Boost), (b) T_{MGU} = -30Nm, n_{MGU} = 25kRPM, I_A = -350A (Recharge)

Chapter 7

Thermal management: Submerged Impinging Jets

7.1 Overview

Advancements in power electronic technologies require devices which are small, reliable and capable to handle always increasing amounts of power. As already said in the previous section, power semiconductors are interested by power dissipation in the order of hundreds of W. This leads to high heat flux densities since power DIODEs, *Insulated-Gate Bipolar Transistors* (IGBTs) and MOSFETs areas is in the order of cm^2. Heat removal from power electronic devices is gaining a fundamental importance in many industrial fields, including the recent application of power electronics in hybrid and electric traction systems. To tackle this technical problem dedicated cooling systems need to be adopted. Different cooling strategies are adopted in industrial applications and the most common are given by pin fins, mini-channels (in a different configuration), and impinging jets heat exchangers.

Pin fins heat exchangers are massively used in power electronics applications. As reported in Ref. [10], the main advantages of this cooling strategy are given by high wetted surface, low pressure loss and simple geometry. Unfortunately, one of the most important limitation can be due to the encumbrance. Moreover, this cooling strategy do not allow to an optimal distribution of the coolant flow rate on the heat source location. This is an important aspect in power electronics field, since power semiconductors can be distributed onto an electronic board in an irregular way. Encumbrance and flow rate distribution can represent a limitations also for mini-channel cooling strategy. Different mini-channel heat exchangers are developed over the years. In Ref. [11], parallel mini-channels are studied and an high heat transfer coefficient is found since the wetted

surface involved is large. However a large pressure drop is ascertained for the specific application because of the flow separation close to the inlet and outlet locations. In Ref. [12] a three-shaped micro-channel heat exchanger is studied. Also in this case, the pressure losses are considerable, but the heat transfer coefficient can grow by working on the geometrical characteristics of the channel. It can also lead to an increase in geometry complexity. Also fractal channels, studied in Refs. [13–17], show limitations in terms of pressure drop and geometrical complexity. For this kind of applications, a multi-objective optimization procedure can be taken into account to found the best trade-off among thermal performance, pressure drop and geometrical complexity. In general, mini channels have a good potential but their performance can strongly depend on the specific application. Arrays of impinging jets might be a promising solution because they efficiently exchange high amounts of heat at an affordable pumping power level [18]. On the other hand, impinging jets are satisfactorily used from decades in several applications such as gas turbine cooling, glass plate tempering and in deicing systems of aircrafts. As shown in Figure 7.1, fluid jets are typically discharged into a quiescent ambient from a nozzle of diameter d_n. As explained in [68], the jet is typically turbulent and, at the nozzle exit, is characterized by a uniform velocity profile. However, with increasing distance from the exit, momentum exchange between the jet and the ambient causes the free boundary of the jet to broaden and the potential core, within which the uniform exit velocity is retained, to contract. Downstream of the potential core the velocity profile is nonuniform over the entire jet cross section and the maximum (center) velocity decreases with increasing distance from the nozzle exit. The region of the flow over which conditions are unaffected by the impingement (target) surface is named the free jet. Within the impingement zone, flow is influenced by the target surface and is decelerated and accelerated in the normal (z) and transverse (x) directions, respectively. Hence, with increasing x, velocity components parallel to the surface increase from a value of zero to some maximum and subsequently decay to zero. Velocity profiles within the wall jet are characterized by zero velocity at both the impingement and free surfaces. If the target wall temperature is higher than the jet temperature, convection heat transfer occurs in the impingement and wall jet regions [68]. In addition, when considering array of jets, the secondary stagnation zones might result from the interaction of adjoining wall jets. In many such schemes the jets are discharged into a restricted volume bounded by the target surface and the nozzle plate from which the jets originate. Array of jets involves more complex flow structure since the jet from one hole is affected by neighbouring jets. They can be positioned either inline or staggered.

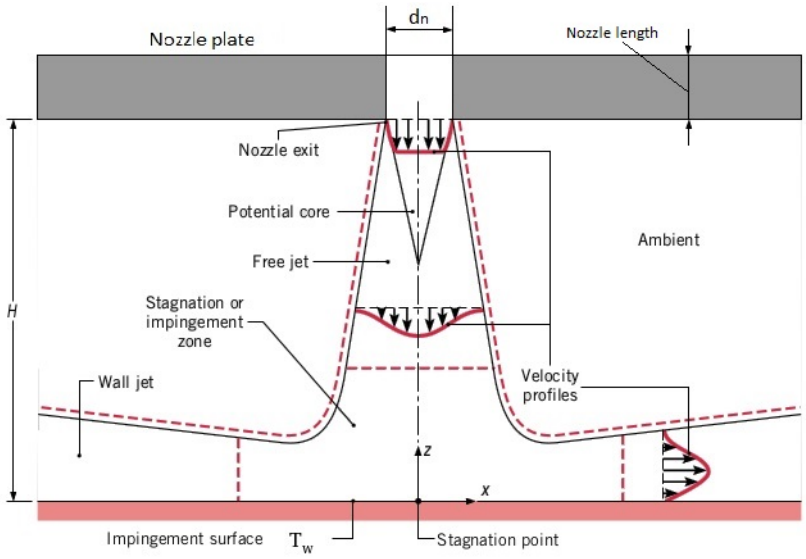

Figure 7.1 Surface impingement of a single round jet [68]

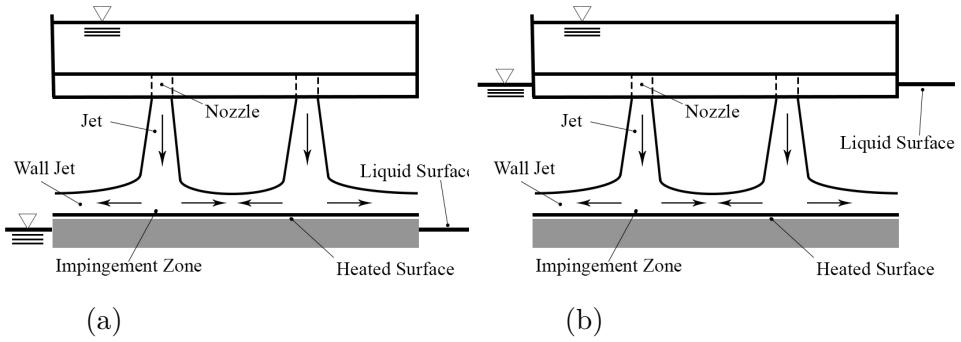

Figure 7.2 Impinging jets categories: (a) free-surface jet impingement, (b) submerged jet impingement

Moreover, liquid impinging jets are divided in two categories: free-surface impinging jets and submerged impinging jets, see figures 7.2(a) and 7.2(b). In the free-surface configuration liquid jets are discharged into a gaseous environment, while in the submerged configuration they are completely surrounded by the same fluid. However, in both cases the fluid is discharged across a plate where the nozzle orifices are manufactured and impinge normally on the heated surface. As reported in many papers, the cooling performance of jet impingements strongly depends on geometrical properties such as: nozzle diameter, nozzle arrangement, nozzle number, aspect ratio and nozzle shape. Diameter effect are widely investigated by Garimella and Nenaydykh[24]: for a given Reynolds number the turbulence intensity near the jet centerline is higher for larger diameter nozzles, with all other parameters kept constant. Similar results

are found by Kataoka et al.[69]. Womac et al.[70] found that for a given flow rate, the heat transfer improved with the increase in jet velocity. A deep investigation involving the aspect ratio effect is also performed by Garimella and Nenaydykh [24], for aspect ratios (the ratio between the nozzle diameter and the nozzle length) smaller than 1 the heat transfer coefficients are the highest. As the aspect ratio growes to values of [1÷4], the heat transfer coefficients drop sharply, but with further increases in aspect ratio of up to [8÷12], the heat transfer coefficients gradually increase. This behaviour can be ascribed to the flow separation and reattachment in the nozzle, and its effect on exit velocity profiles. Several researchers have investigated the effect of the jet-to-target spacing. As proposed by Churchill and Usagi [71], the heat transfer coefficient progressively grows with H/d_n and the peak has been detected for $H/d_n = 5$. H is the distance between the nozzle plate and the target surface while d_n indicates the nozzle diameter as previously said. Gardon and Akfirat [72] explains that the enhancement of heat transfer with nozzle-jet spacing is due to an increase of the turbulence generated by the jet itself. Hollworth et al. [73] found that the potential core length changes with the nozzle shape for turbulent jet. However, Garimella et al.[24] observed as the stagnation Nusselt number has been observed to increase slightly, or remain constant, as H/d_n increases from 1 to about 4, for a wide range of Reynolds numbers. Accorrding to [24], analogous considerations are reported in refs. [25][74][75]. In this H/d_n range, the axial velocity of the jet remains constant explaining the relative constancy of the stagnation Nusselt number. At larger H/d_n, where impingement occurs beyond the potential core, the axial velocity decreases with increasing distance and the level of turbulence begins to increase due to the large-scale structures in the mixing region. The decreasing axial velocity results in decreasing stagnation heat transfer coefficients. The nozzle shape effect is widely investigated by Ronye and Dey [76]: nozzles which presents chamfer at the inlet location provides higher average heat transfer coefficient than straight geometry. Furthermore, the chamfered design lead a lower pressure drop if the flow rate is kept constant. This agrees with Whelan and Robinson [77]. Numerical study of a single impinging jet considering heat transfer and flow field are carefully investigated by Morris et al. [26][27]. The results are compared with experimental data proposed in refs. [24][25][74][75]. A similar work will be presented in this study considering the latter papers for a numerical validation of a CFD code used for the current investigation. Finally, a detailed study is performed by Fitzgerald and Garimella [78] in order to capture the main features of the flow field. In the current study, impinging jet arrays in cooling electronic devices have been evaluated by performing 3D-CFD conjugated heat transfer simulations. The adopted

numerical procedure is validated against experimental data, provided by ref.[24] and [25], to ascertain the accuracy of adopted model. Therefore, a detailed analysis is successively performed and results are compared and discussed in order to obtain the best compromise in terms of cooling efficency and pumping power required by the feed system. Three nozzle diameters are considered, associated with two different aspect ratios of 1 and 0.5 respectively. Both inline and staggered arrangements are adopted and an increase of nozzles number are taken into account. Heat generation rate of the chip and inlet temperature of the coolant is the same for all the simulated configurations. Moreover, every analysis are computed under a given pressure drop, this is done in view of numerical considerations and following the suggestions reported in refs. [26][27] and it represents a practical problem, very close to electric traction applications.

7.2 Methods and Materials

7.2.1 Computational method

In the present work, a numerical simulations are performed by the open source software OpenFOAM®. The specific solver employed is the *chtMultiRegionSimpleFoam*, a steady-state solver which imposes mass conservation through the SIMPLE algorithm and allows for the simulation of conjugate heat transfer cases. A second order central scheme is used for spatial discretisation of the diffusive term, while a first order upwind scheme is employed for advection. Turbulent stresses and turbulent heat fluxes are represented by an eddy viscosity approach in a RANS context. As the Reynolds number based on the jet velocity and the jet diameter is transitional in all cases considered, a turbulence model is employed relying on the fact that in regions of low turbulence level the computed eddy viscosity is close to zero. The specific turbulence model employed in the present work is selected according to the results of a validation test performed on a single-jet configuration and reported in the following paragraphs. Comparison of the single jet results obtained using the SST $k-\omega$ and the $k-\varepsilon$ turbulence models suggests that SST $k-\omega$ model is more accurate, while the $k-\varepsilon$ model overestimates heat transfer rates in the impingement and reattachment regions. Thus, in this work, turbulence is represented by the SST $k-\omega$ model.

A structured, hexahedral mesh is employed in all the simulations. To avoid the use of wall functions, meshes used are built so that the maximum distance between the centroid of the first computational cell and the wall is less than 3 wall units ($y^+_{w,\max} < 3$),

while the average distance $y^+_{w,\mathrm{avg}} \leq 1$ for each simulation. The size of control volumes in solid regions is larger than in the fluid region because of the smooth behaviour of temperature in solids. However the interfaces between different regions are conformal in order to avoid interpolation errors.

In this work viscous dissipation and buoyancy effects are neglected. These hypotheses are confirmed by appropriate, preliminary analyses.

7.2.2 Data reduction

The Performance Evaluation Criteria (PEC) used to assess the performances of the jet configurations are the following:

- overall heat transfer coefficient $\overline{h}$;
- thermal resistance R_{th};
- pumping power P_p.

The overall heat transfer coefficient $\overline{h}$ is defined as

$$\overline{h} = \frac{\dot{Q}}{A_w \left([T_w] - T_{b,\mathrm{in}} \right)} \tag{7.1}$$

where $\dot{Q}$ is the heat transferred from the chip to the coolant in the time unit, A_w is the surface extension of the solid-liquid interface, $[T_w]$ is the average temperature of this interface, and $T_{b,\mathrm{in}}$ is the bulk temperature of the coolant at the inlet. In addition, distributions of local heat transfer coefficient

$$h = \frac{\dot{Q}}{A_w \left(T_w - T_{b,\mathrm{in}} \right)} \tag{7.2}$$

are computed on the impingement plates in order to provide maps of heat transfer rates. Maps are presented by normalising the local heat transfer coefficient for easier comparison

$$h^* = \frac{h - h_{\min}}{h_{\max} - h_{\min}} \tag{7.3}$$

In equation (7.3) $h_{\max}$ and $h_{\min}$ represent the maximum and minimum values of h among all the configurations studied.

The overall thermal resistance R_{th} between chip and coolant is defined using the temperature difference between the maximum chip temperature $T_{\max}$ and the coolant

inlet bulk temperature, as in ref. [79].

$$R_{\text{th}} = \frac{T_{\max} - T_{b,\text{in}}}{\dot{Q}} \tag{7.4}$$

The mechanical energy per time unit required for maintaining the flow of the coolant is calculated as

$$P_p = \dot{V}\,\Delta p \tag{7.5}$$

where $\dot{V}$ is the volumetric flow rate and Δp is the pressure drop between the inlet and the outlet sections, $\Delta p = p_{in} - p_{out}$.

To preserve confidentiality of configurations and conditions, data are presented in a normalised form (indicated by $*$) using reference quantities defined as follows. The reference length is

$$l_{\text{ref}} = \sqrt{l_1\, l_2} \tag{7.6}$$

where $l_1\, l_2 = A$ is the chip plan area. The reference velocity definition is based upon the imposed pressure drop Δp and the fluid density $\rho = \rho_{\text{ref}} = 978$ kg/m^3

$$u_{\text{ref}} = \sqrt{2\,\Delta p/\rho} \tag{7.7}$$

while the reference temperature is

$$T_{\text{ref}} = \frac{P_0}{\rho\, u_{\text{ref}}\, l_{\text{ref}}^2\, c} \tag{7.8}$$

In this equation P_0 is the heat generation rate of the chip and $c = c_{\text{ref}} = 4187$ J/(kg K) is the specific heat. Both P_0 and c are kept constant in this study.

Configurations are compared using the normalised form of thermal resistance, overall heat transfer coefficient and pumping power

$$R^*_{\text{th}} = \frac{R_{\text{th}}}{R_{\text{th,ref}}} \qquad \overline{h}^{\,*} = \frac{\overline{h}}{\overline{h}_{\text{ref}}} \qquad P^*_p = \frac{P_p}{P_{\text{ref}}} \tag{7.9}$$

Reference quantities in equation (7.9) are defined from those in equations (7.6), (7.7) and (7.8)

$$R_{th,\text{ref}} = \frac{T_{\text{ref}}}{P_{\text{ref}}} \qquad \overline{h}_{\text{ref}} = \frac{P_{\text{ref}}}{T_{\text{ref}}\, l_{\text{ref}}^2} \qquad P_{\text{ref}} = \rho\, l_{\text{ref}}^2\, u_{\text{ref}}^3 \tag{7.10}$$

Table 7.1 Comparison between results obtained with $k-\varepsilon$ and SST $k-\omega$ turbulence models. Reference experimental and numerical data are taken from paper [27].

	$k-\varepsilon$	SST $k-\omega$	Experiment [27]	Simulation [27]
Pressure drop (Pa)	7116	7116	7116	7500
Mass flow rate (kg/s)	0.0288	0.0310	0.0326	0.0326
Discharge coefficient	0.713	0.768	0.806	-
Reattachment length	-	0.92 d_n	-	0.80 d_n

7.3 Test Case validation

Prior to the study of jet arrays, the numerical procedure has been assessed and tuned. Validation is performed by comparing results on a single axisymmetric jet case against experimental and numerical results reported in refs. [26] and [27]. The validation case involves a jet of diameter $d_n = 3.18$ mm impinging on a flat plate heated uniformly by a constant heat flux equal to $\dot{q} = 25\,\mathrm{W/cm^2}$. Simulations are conducted resorting to an axisymmetric model. Details on domain dimensions and boundary conditions can be found in ref. [27].

Two turbulence models are compared, the $k-\varepsilon$ and the SST $k-\omega$, in both cases no specific wall treatment is included. The average and maximum distance of the first computational point from the wall are respectively $y^+_{w,\mathrm{avg}} = 0.9$ and $y^+_{w,\mathrm{max}} = 2.9$. The radial profiles of the local heat transfer coefficient on the impingement plate are reported in figure 7.3, where they are compared with experimental results in ref. [26]. It appears that the SST $k-\omega$ model reproduces experimental data more accurately than the $k-\varepsilon$ model. The comparison between present results and data from ref. [27] is summarised in table 7.1. Mass flow rate, reattachment point position and discharge coefficient are predicted by the SST $k-\omega$ model more accurately than by the $k-\varepsilon$ model. The discharge coefficient is calculated by

$$C_d = \frac{\dot{m}_r}{\dot{m}_{\mathrm{id}}} = \frac{\dot{m}_r}{N\pi d_n^2}\sqrt{\frac{8}{\rho\,\Delta p}} \tag{7.11}$$

where $\dot{m}_r$ represents the computed mass flow rate and $\dot{m}_{\mathrm{id}}$ is the mass flow rate after Bernoulli. N and d_n are the number of jets and their diameter, Δp is the imposed pressure drop between inlet and outlet and ρ is the fluid density.

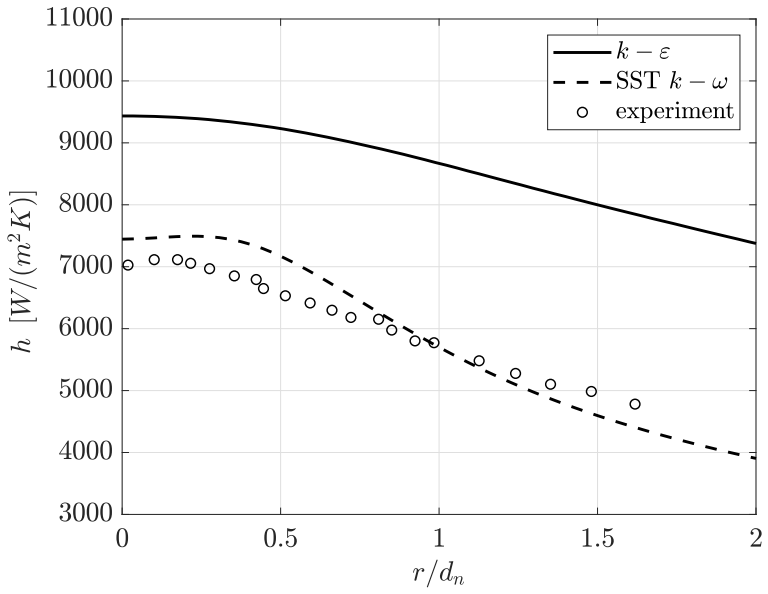

Figure 7.3 Radial profiles of local heat transfer coefficient on the impingement plate in the axisymmetric jet simulation: comparison between present results obtained with k $-\ \varepsilon$ and SST k $-\ \omega$ turbulence models and experimental data from ref. [26].

Tests are performed also to check that previous results are independent of the computational grid and for assessing the influence of a fillet at the nozzle entrance. These analyses are both carried out employing the SST k $-\ \omega$ turbulence model.

The grid sensitivity analysis involves three meshes of increasing mesh density: $\mathcal{G}_1$, $\mathcal{G}_2$ (used to obtain results presented above) and $\mathcal{G}_3$, which respectively include 8×10^3, 40×10^3 and 80×10^3 control volumes.

In figure 7.4 the profiles of heat transfer coefficient obtained with different computational grids are compared, together with experimental data from ref. [26]. The profile computed on the coarse grid $\mathcal{G}_1$ is closer to experimental results than $\mathcal{G}_2$ and $\mathcal{G}_3$ but it shows to be grid-dependent. Instead grids $\mathcal{G}_2$ and $\mathcal{G}_3$ provide essentially the same results, and these are deemed to be non-dependent upon the spatial discretisation. The same outcome arises from the comparison of fluid dynamic parameters reported in table 7.2, where the reattachment length for coarse simulation is not reported since the wall-normal derivative of the streamwise velocity component does not display a clear behaviour in the nozzle.

The influence of a fillet at the nozzle entrance is also assessed. The selected fillet radius is $R_{\text{fillet}} = 0.04\,\text{mm}$, this value being typical for holes obtained by laser drilling. Figures 7.5(a) and 7.5(b) show the computational grids around the nozzle for the configurations with and without fillet. Results obtained in the two configurations

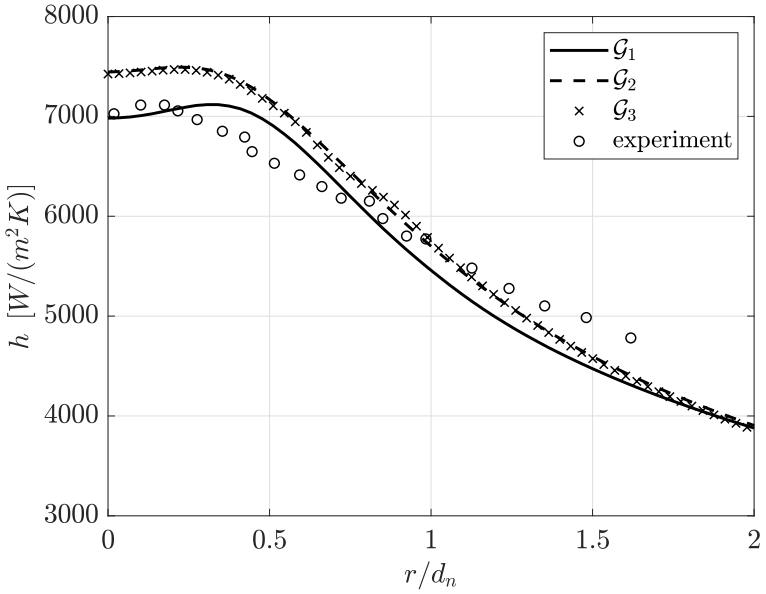

Figure 7.4 Radial profiles of local heat transfer coefficient on the impingement plate in the axisymmetric jet simulation: comparison between results obtained with different computational grids and experimental data from ref. [26].

Table 7.2 Comparison between fluid dynamic parameters obtained with different computational grids.

	$\mathcal{G}_1$	$\mathcal{G}_2$	$\mathcal{G}_3$
Pressure drop (Pa)	7116	7116	7116
Mass flow rate (kg/s)	0.0318	0.0310	0.0311
Discharge coefficient	0.787	0.768	0.770
Reattachment length	-	0.92 d_n	0.91 d_n

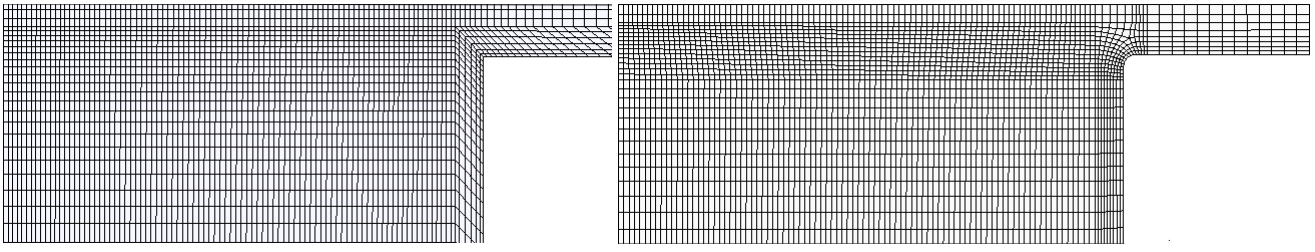

(a) (b)

Figure 7.5 Computational grids in the nozzle region of the axisymmetric jet simulation: (a) sharp-edge nozzle, (b) filleted nozzle.

Table 7.3 Comparison between results on the sharp-edge and filleted nozzle configurations, with reference data from paper [27].

	Sharp-edge	Filleted	Experiment [27]	Simulation [27]
Pressure drop (Pa)	7116	7116	7116	7500
Mass flow rate (kg/s)	0.0310	0.0323	0.0326	0.0326
Discharge coefficient	0.768	0.800	0.806	-
Reattachment length	0.92 d_n	0.75 d_n	-	0.80 d_n

are reported in figure 7.6 and table 7.3, where these are also compared against data reported in papers [26] and [27]. The filleted configuration provides results closer to the experiment than the sharp-edged nozzle, both in terms of heat transfer and fluid dynamic parameters. The mass flow rate increase and the different discharge coefficient are to be ascribed to the reduction in adverse pressure gradient. This effect motivates also the shorter separation length.

Furthermore, a flow field representation is shown in Fig 7.7, where a smaller separation bubble has been observed for the fillet configuration (shorter separation length). According to the other literature contribution [80–82], for every case the separation length is lower than 1 diameter.

7.4 Numerical investigation

7.4.1 Description of simulated cases

The simulation campaign is conducted to investigate the behavior of cooling performance and pumping power over a range of geometrical parameters. The arrangement and number of jets N, their diameter d_n^*, and the ratio between nozzle length L and diameter $AR = L/d_n$ are assigned as shown in table 7.4, which summarises all configurations investigated. Suggestions on promising configurations are taken from refs. [24, 76, 77, 25, 74, 75]. The configuration name, in the first column of table 7.4, is descriptive of the main geometric features. The capital letter indicates the nozzle diameter, L stands for “large” diameter, A for “average” and S for “small”, while the number corresponds to the total number of jets. When present, "s" indicates that jets are staggered and "b" marks the AR = 0.5 geometries. The inline and staggered configurations are indicated by $N \times N$ and $N \times N\_M \times M$ respectively, where $M = N - 1$ because each staggered configuration is obtained by addition of a $M \times M$ array to the initial, coarser $N \times N$

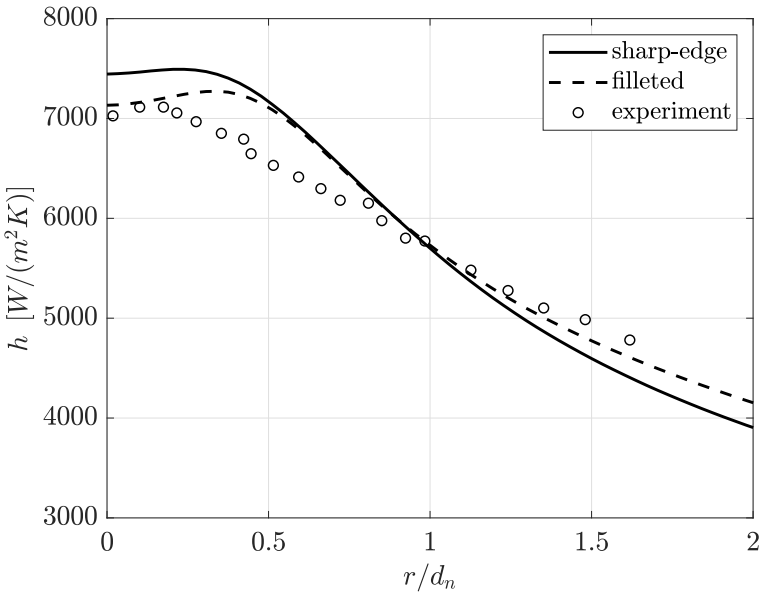

Figure 7.6 Radial profiles of local heat transfer coefficient on the impingement plate in the axisymmetric jet simulation: comparison between results obtained on the sharp-edge and filleted configurations and experimental data from ref. [26].

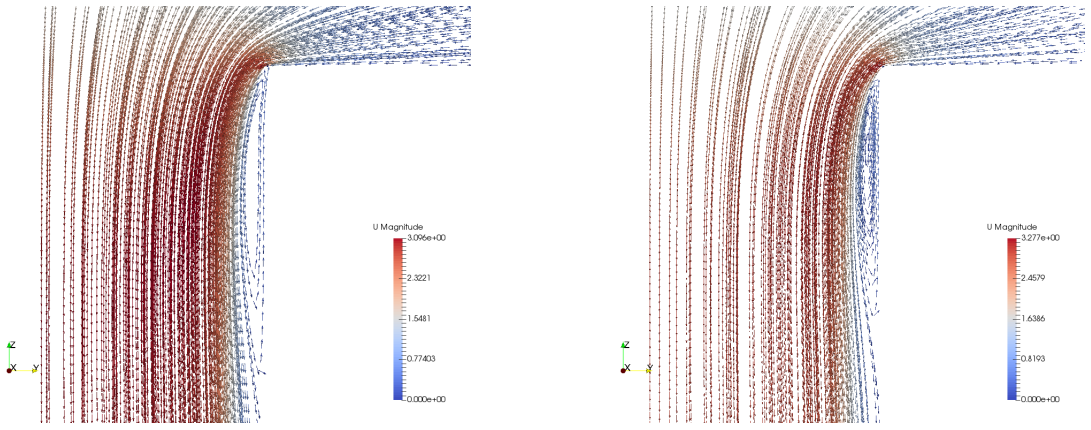

(a) (b)

Figure 7.7 Flow field representation at the nozzle locations: (a) Sharp-edge configuration; (b) Filleted configuration

Table 7.4 Summary of configurations investigated. The nozzle diameter d_n is made non-dimensional using the reference length l_{ref}, defined in equation (7.6).

Test	d_n^*	disposition	N	arrangement	AR	H/d_n
L9	0.100	3×3	9	inline	1	3
L9b	0.100	3×3	9	inline	0.5	3
L13s	0.100	$3 \times 3\_2 \times 2$	13	staggered	1	3
L13sb	0.100	$3 \times 3\_2 \times 2$	13	staggered	0.5	3
A16	0.050	4×4	16	inline	1	3
A25s	0.050	$4 \times 4\_3 \times 3$	25	staggered	1	3
A36	0.050	6×6	36	inline	1	3
A49	0.050	7×7	49	inline	1	3
A61s	0.050	$6 \times 6\_5 \times 5$	61	staggered	1	3
A85s	0.050	$7 \times 7\_6 \times 6$	85	staggered	1	3
S64	0.030	8×8	64	inline	1	3
S81	0.030	9×9	81	inline	1	3
S100	0.030	10×10	100	inline	1	3

array. Notice that the nozzle-to-target distance H is set to 3 times the nozzle diameter in all cases. This is done in order to reduce the degrees of freedom of impinging-jet configurations and because the ratio $H/d_n = 3$ is deemed near optimal, as reported in refs. [24], [83] and [77].

The computational domain is depicted in figure 7.8(a), it is composed by a stack of different solid and fluid regions: a chip (which is the volumetric heat source), two layers of copper and ceramic, an aluminium plate and the coolant region, which includes an inlet plenum, the nozzles and a discharge zone. The copper, ceramic, and aluminium layers oppose a conductive thermal resistance to the heat flux per unit area of $R'_{co} = 8.44 \times 10^{-4}\ R'_{\text{ref}}$, $R'_{ce} = 3.66 \times 10^{-3}\ R'_{\text{ref}}$ and $R'_{al} = 1.55 \times 10^{-2}\ R'_{\text{ref}}$ respectively, where R'_{ref} is the reference thermal resistance for the heat flux per unit area, $R'_{\text{ref}} = (T_{\text{ref}}\, l^2_{\text{ref}})/P_{\text{ref}}$. Geometrical and thermal properties of solid regions are held constant among all the configurations studied for keeping the same thermal conditions at the solid-liquid interface, see ref. [84] about this topic.

As shown in figure 7.8(a), the configuration is symmetric about two planes, and only one quarter of the geometry considered is actually simulated. A (x, y) section of the nozzle plate is displayed in figure 7.8(b).

The coolant enters the domain by the lateral boundaries of the inlet plenum at the fixed temperature $T^*_{in} = 857$, passes through the nozzles, exchanges heat from the aluminium plate and exits through the lateral boundaries of the discharge zone. The

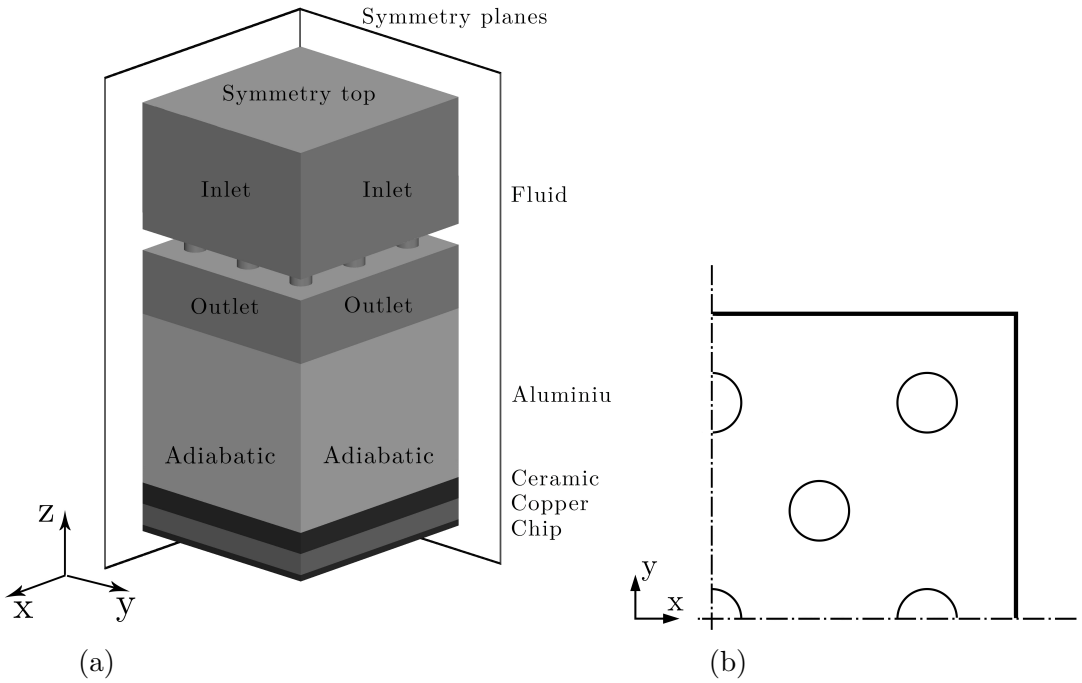

Figure 7.8 (a) Computational domain and boundary conditions employed in simulations, (b) (x, y) section of the nozzle plate for configurations L13s and L13sb.

mechanical energy per unit time for maintaining the flow is provided by imposing a relative pressure Δp at the inlet and ambient pressure at the outlet. At the top of the inlet plenum as well as at the symmetry planes, symmetric boundary conditions are applied, while no-slip conditions are imposed at the other boundaries of the fluid region. Figure 7.8(a) shows boundary conditions on a sketch of the computational domain. The thermal input relative to the entire chip is $P_0^* = 0.025$ and is provided by setting a volumetric heat source in the chip. Heat transfer occurs exclusively in the z direction through the solid regions, and finally to the coolant; no heat is transferred through the x- or y-normal boundaries of the solid regions because these are set to adiabatic or symmetric, which at second order accuracy corresponds to the adiabatic condition.

Computational domains of the different simulations are discretised with topologically structured grids and involve from 2 to 4 million hexahedral cells. At the solid-liquid interface the mesh is conformal and a Low-Reynolds approach is adopted and checked *a posteriori*. Simulations are considered converged when the mass-flow rate and the outlet bulk temperature display a flat behaviour and residuals are below the threshold $\mathcal{R}_t = 10^{-4}$.

Table 7.5 Comparison between results obtain with different computational grids on configuration L9b. PEC reported are defined in equations (7.9) and (7.11).

PEC	coarse	intermediate	fine
R^*_{th}	0.060	0.058	0.058
$\overline{h}^*$	25.42	25.25	25.21
P^*_p	0.0236	0.0250	0.0248
C_d	0.66	0.71	0.70

Heat transfer characteristics of configurations tested are analysed in section 7.5. Results are grouped in paragraphs by fixing the jet diameter and for variable jet configurations. An overview of heat transfer performance is provided in section 7.6, where two summarising figures are also displayed.

7.5 Results

7.5.1 Grid sensitivity analysis

In order to check that results are not grid-dependent, a grid sensitivity analysis is performed on configuration L9b using three meshes of increasing mesh density. The coarse mesh is composed by ~ 0.4 millions cells overall and each jet is discretised using 27, 28 and 50 control volumes respectively along the axial, radial and circumferential directions. The intermediate mesh is obtained by doubling the number of cells in each direction thus counting ~ 3.2 millions cells, while the fine grid is obtained by a further refinement by a factor 1.5 along the impingement direction.

Table 7.5 compares the PEC computed with different meshes. While on the intermediate and fine meshes almost the same results are obtained, PEC computed on the coarse mesh are somewhat different. As a consequence, configurations presented hereafter are tested using computational grids comparable with intermediate mesh.

7.5.2 Aspect ratio effect

Simulations L13s and L13sb share the same configuration but have different aspect ratio: $AR = 1$ and $AR = 0.5$ respectively. These are compared in order to assess the effect of the aspect ratio. The nozzle arrangement is displayed in figure 7.8, where only the simulated quarter of geometry is depicted. Figures 7.9(a) and 7.9(b) display the distributions of the local heat transfer coefficient on the impingement plate of the two

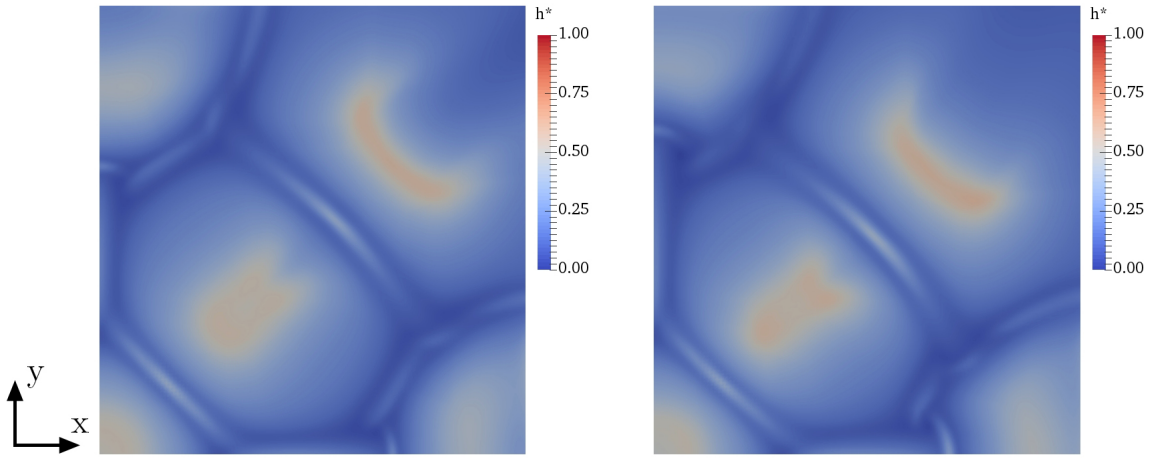

(a) (b)

Figure 7.9 Normalised heat transfer coefficient on the impingement plate: (a) case L13s ($AR = 1$), (b) case L13sb ($AR = 0.5$).

cases considered, where qualitatively no substantial differences can be observed. Note that these pictures display the non-dimensional heat transfer coefficient h^* only in the simulated portion of the impingement plate. Due to impingement, h^* reaches a local maximum under each jet and these regions share almost the same shape in the two cases considered. In addition, from the skewed regions of high h^* in figures 7.9(a) and 7.9(b), it can be observed that the flow toward the lateral outlet boundaries imposes a larger deviation to the peripheral jets with respect to the central ones, as also observed in paper [85]. More local heat transfer coefficient maxima are observed in the regions where the boundary layers on the impingement plate relative to different jets interact and give place to an increase in turbulent kinetic energy, see also ref. [86]. Table 7.6 compares the PEC and shows that the $AR = 1$ configuration achieves a slightly higher overall heat transfer coefficient. Also the cost in terms of pumping power is about 2% higher, which indicates that the $AR = 1$ case is characterised by a slightly higher mass flow rate. Moreover, the higher discharge coefficient in the $AR = 1$ configuration denotes a better fluid dynamic efficiency.

Results presented are in agreement with refs. [76] and [77] which report of smaller pressure drops for higher aspect-ratio nozzles, which in turn lead to higher mass flow rates and higher global heat transfer coefficients when pressure is fixed at the inlet and outlet boundaries, as in present simulations. On the other hand, Garimella and Nenaydykh [24] found lower heat transfer coefficients for $AR > 1$. This is only apparently in contrast with present results because in paper [24] experiments are

Table 7.6 Comparison between performances of configurations L13s ($AR = 1$) and L13sb ($AR = 0.5$). PEC reported are defined in equations (7.9) and (7.11).

PEC	$AR = 0.5$	$AR = 1$
R^*_{th}	0.056	0.055
$\overline{h}^*$	28.37	29.23
P^*_p	0.0369	0.0377
C_d	0.72	0.74

performed with a fixed mass flow rate and the higher $\overline{h}^*$ of the present $AR = 1$ configuration can be ascribed to a mass flow rate increase. These results together with data reported in papers [76], [77] and [24] suggest that configurations with $AR = 1$ allows to achieve better thermal performances with respect to $AR = 0.5$. Then in the following only unitary aspect ratios will be considered.

7.5.3 Large diameter

In this section results of configuration L9 (figure 7.10(a)) and the corresponding staggered configuration L13s (figure 7.8(b)) are compared. Figure 7.10(b) displays the distribution of local heat transfer coefficient for the L9 configuration. It can be observed that the impingement regions of the corner jets are mainly deviated along y, while in the L13s configuration deviation is almost diagonal, see figure 7.9(a). This behaviour can be ascribed to a different interaction of the jets and a predominant direction of the flow close to the outlet sections.

As reported in table 7.7 the overall heat transfer coefficient of the L13s configuration is around 10% higher than L9. Accordingly, lower chip temperature and lower thermal resistance are achieved by the staggered configuration, but a 34% larger pumping power is required. Performances of L13s configuration are associated with its higher mass flow rate.

7.5.4 Average diameter

All the configurations whose code starts with A have been designed considering the work by Womac *et al.* [70], where it is argued that a reduction in nozzles diameter improves the thermal performances of impinging jets.

The A16 configuration and the corresponding staggered one (A25s) are depicted in figures 7.11(a) and 7.11(b), while the respective fields of local heat transfer coefficient

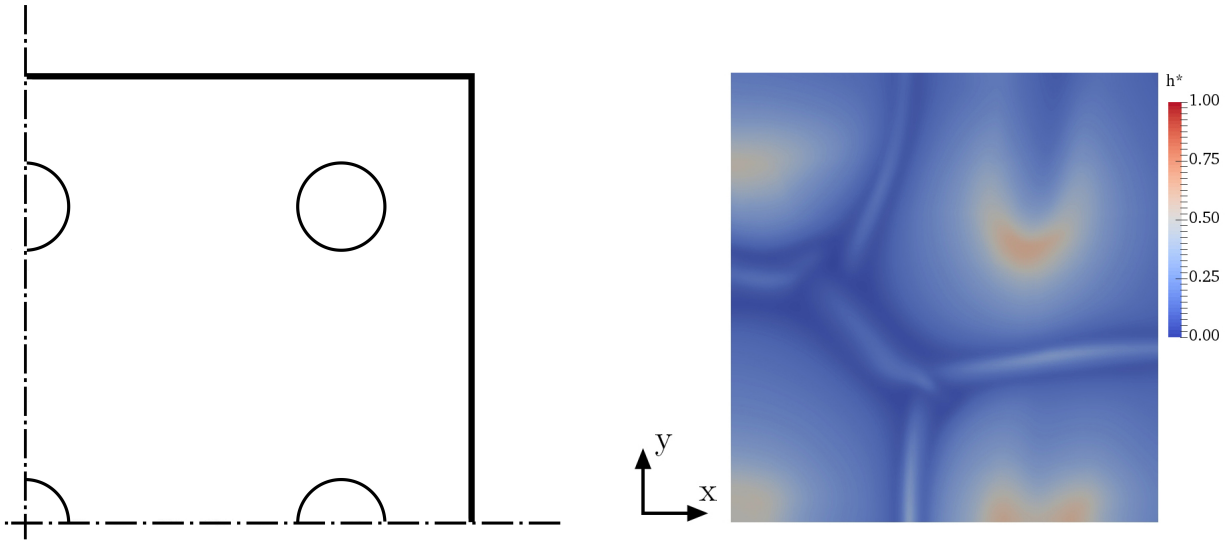

(a) (b)

Figure 7.10 Configuration L9: (a) nozzle arrangement, (b) local heat transfer coefficient on the impingement plate.

Table 7.7 Comparison between performances of configurations L9 and L13s. PEC reported are defined in equations (7.9) and (7.11).

PEC	L9	L13s
R^*_{th}	0.059	0.055
$\overline{h}^*$	26.41	29.23
P^*_p	0.0250	0.0377
C_d	0.71	0.74

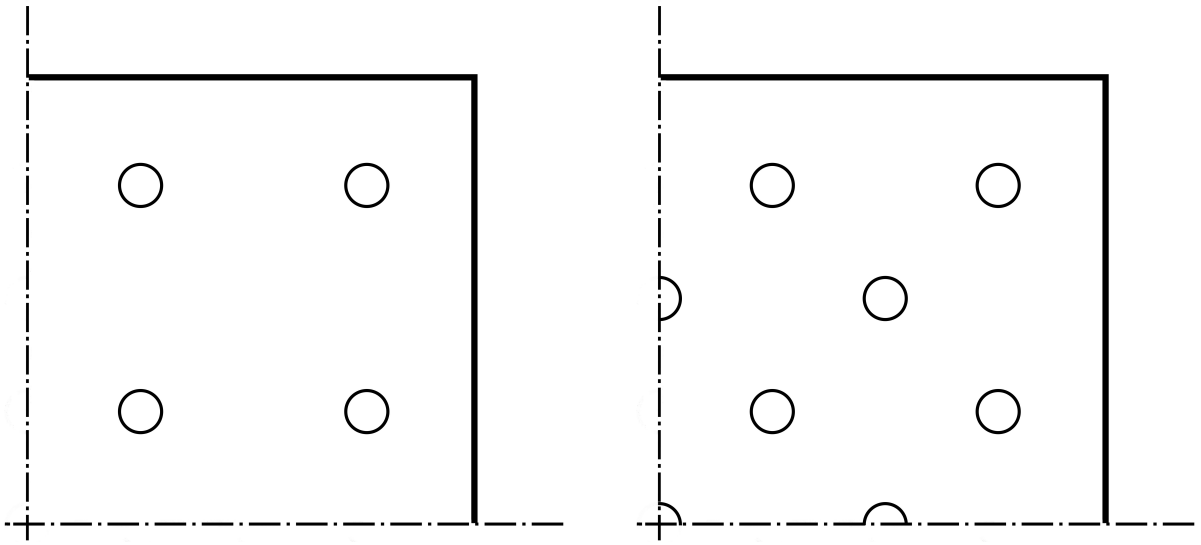

(a) (b)

Figure 7.11 Nozzle plate configurations: (a) A16, (b) A25s.

Table 7.8 Comparison between performances of configurations A16, A25s and L13s. PEC reported are defined in equations (7.9) and (7.11).

PEC	A16	A25s	L13s
R^*_{th}	0.062	0.056	0.055
$\overline{h}^*$	24.56	28.66	29.23
P^*_p	0.0108	0.0168	0.0377
C_d	0.69	0.68	0.74

on the impingement plates are reported in figures 7.12(a) and 7.12(b). Since in these cases the diameter is smaller than the previous configurations, the regions of high h^* due to impingement are narrower. Moreover, the increased number of jets leads to a more intense interaction among them, particularly in the A25s case, as shown by the skewed shapes of the impingement regions.

Configurations A16 and A25s are compared to case L13s in table 7.8. The staggered architectures (A25s and L13s) provide comparable values of R^*_{th} and $\overline{h}^*$, which denote better thermal performances than configuration A16. Surprisingly this result is achieved by configuration A25s requiring less than half the pumping power required by L13s, which at given pressure drop and constant density corresponds to less than half mass flow rate. Hence case A25s is almost two times more efficient than L13s. As apparently remarkable thermal performances can be achieved at a low cost in terms of pumping

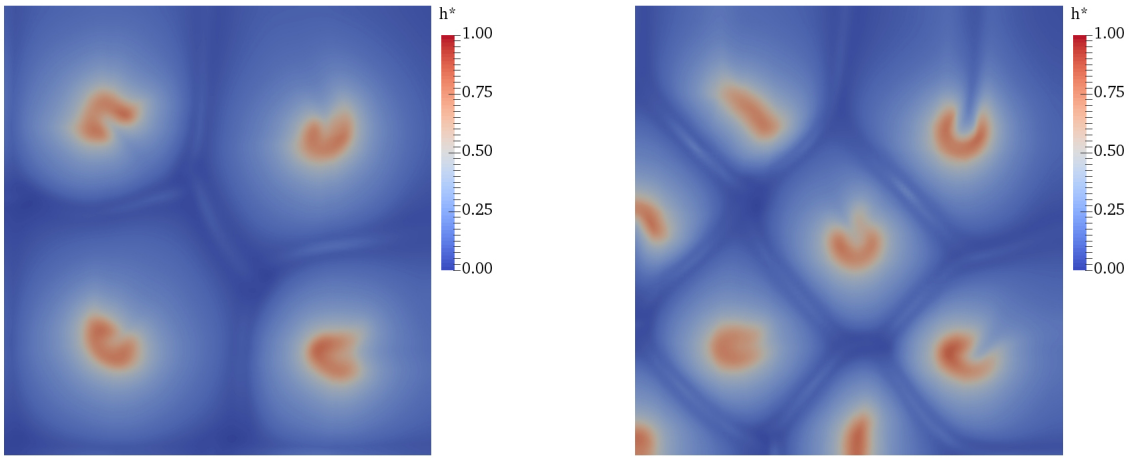

(a) (b)

Figure 7.12 Normalised heat transfer coefficient on the impingement plate: (a) configuration A16, (b) configuration A25s.

Table 7.9 Comparison between performances of configurations A36, A49, A61s, and A85s. PEC reported are defined in equations (7.9) and (7.11).

PEC	A36	A49	A61s	A85s
R^*_{th}	0.052	0.051	0.050	0.049
$\overline{h}^*$	32.13	33.60	34.43	35.12
P^*_p	0.0223	0.0275	0.0355	0.0612
C_d	0.63	0.57	0.59	0.73

power by an increased number of jets, architectures A36, A49 and the relative staggered ones, A61s and A85s, are considered; these are sketched in figures 7.13(a), 7.13(b), 7.13(c), and 7.13(d).

Overall results are presented in table 7.9. The increased number of jets leads to improved thermal performances but higher pumping power requirements. In particular, configuration A85s provides a thermal resistance 14% lower than case A25s, but require a pumping power which is more than 3.5 times higher. From these results it appears that further increases in N would lead to slightly higher thermal performances but much larger requests of mechanical power. This asymptotic trend is emphasised in the following section.

Contours of local heat transfer coefficients are presented in figures 7.14(a), 7.14(b), 7.14(c) and 7.14(d), where peaks of heat transfer rate corresponding to jets close to

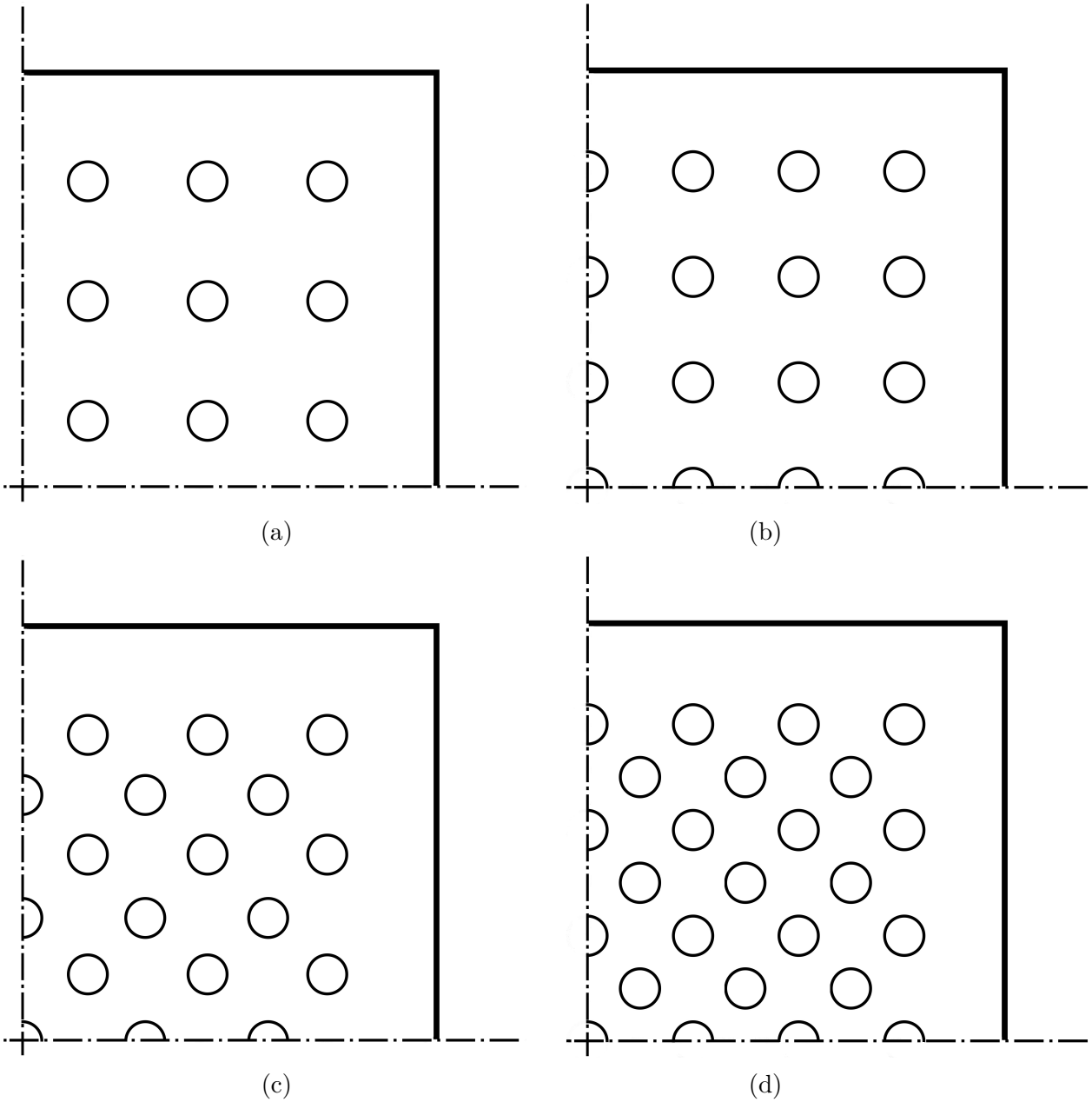

Figure 7.13 Nozzle plate configurations: (a) A36, (b) A49, (c) A61s, (d) A81s.

the outlet boundaries are markedly weaker than in the central region. As already commented, this is due to the higher mass flow rate in configurations with larger N. Indeed the (x, z) and (y, z) plenum cross-sections of configurations A36, A49, A61s and A85s are the same: l_1 and l_2 are given and $H = 3\,d_n$ is constant when d_n is fixed, *e.g.* in "A" configurations. Therefore higher mass flow rates lead to higher velocities in the (x, y) plane, which deviate the peripheral jets from the ideal, orthogonal impingement. This phenomenon is deemed to motivate the marginal heat transfer enhancement observed in configurations A36, A49, A61s and A85s.

7.5.5 Small diameter

The results in the previous sections suggest that nozzles with smaller diameter provide better thermal performances, thus a further reduction of d_n might be beneficial and simulations whose code starts with S have been designed for this reason. As for large nozzle numbers the strong flow fields in the discharge plenum prevent the effective impingement of jets, a limit is sought for the total area of nozzles:

$$A_n = (N\pi d_n^2)/4 \tag{7.12}$$

The comparison of heat transfer coefficient distributions reported in figure 7.14 shows qualitatively that configuration A36 allows for an almost undisturbed jet impingement. Thus its total area of nozzles, $A_n^{(\mathrm{A36})} = 0.09\ (\pi/4)\, l_{\mathrm{ref}}^2$, has been designated as the reference maximum total nozzle area allowing for an effective impingement of all jets. In order to match area $A_n^{(\mathrm{A36})}$ by an array of jets of diameter $d_n = 0.03\, l_{\mathrm{ref}}$ (*i.e.* the nozzles diameter in "S" configurations), one hundred jets must be employed

$$0.03^2\, N\, (\pi/4)\, l_{\mathrm{ref}}^2 = A_n^{(\mathrm{A36})} \quad \Rightarrow \quad N = 100 \tag{7.13}$$

Figure 7.15a shows configuration S100, which involves 100 nozzles arranged in a 10×10 inline array. As according to equation (7.13) configuration S100 is at the upper A_n limit, also configurations S64 and S81 are considered, respectively with N=64 and N=81 both arranged inline. These are displayed in figures 7.15b and 7.15c.

Distributions of h^* on the impingement plate of configurations S64, S81 and S100 are reported in figures 7.16(a), 7.16(b) and 7.16(c). As expected peaks related to impingement are not skewed and indicate that jets do not undergo a substantial deflection. The total nozzle area limit, set tentatively to $A_n^{(\mathrm{A36})}$, can then be considered as a practical indication for an effective impingement of all jets in present conditions.

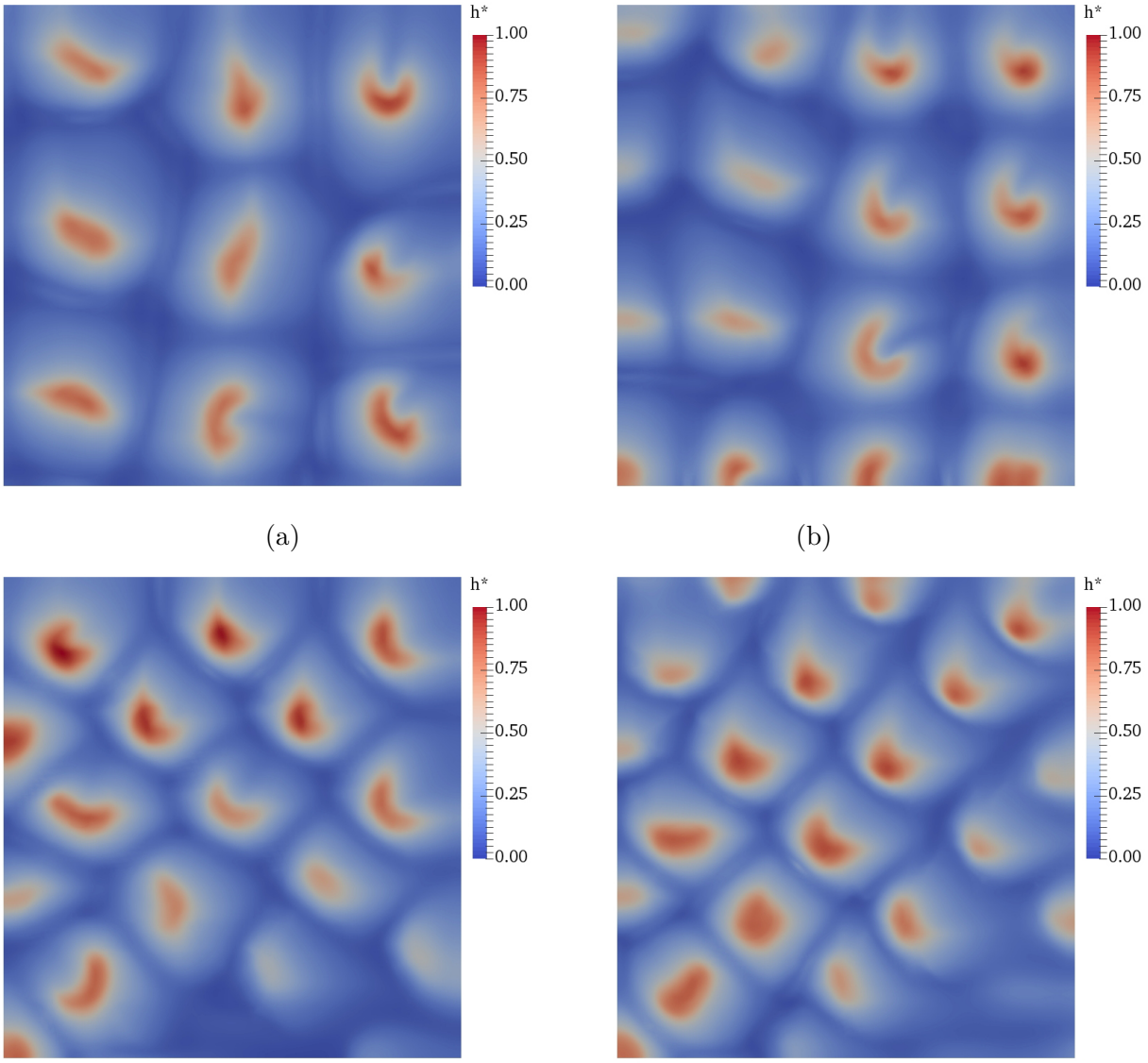

Figure 7.14 Normalised heat transfer coefficient on the impingement plate in configurations: (a) A36, (b) A49, (c) A61s and (d) A85s.

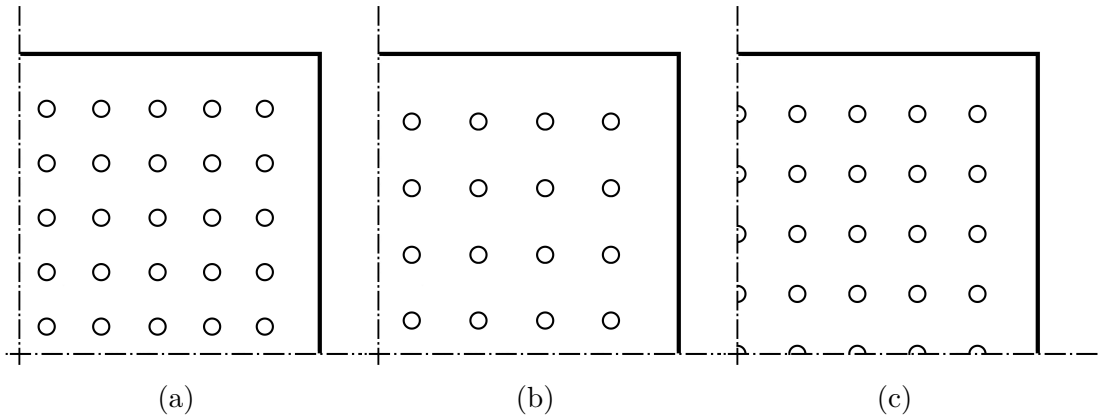

Figure 7.15 Nozzle plate configurations: (a) S100, (b) S64, (c) S81.

Table 7.10 Comparison between performances of configurations S64, S81 and S100. PEC reported are defined in equations (7.9) and (7.11).

PEC	S64	S81	S100
R^*_{th}	0.051	0.049	0.047
$\overline{h}^*$	33.59	36.30	39.01
P^*_p	0.0147	0.0186	0.0230
C_d	0.65	0.65	0.65

The PEC of configurations with small diameter are reported in table 7.10, where a consistent reduction of pumping power and better thermal performances are achieved with respect to average diameter configurations. For example, the thermal resistance of configuration S100 is comparable to case A85s, but the overall heat transfer coefficient $\overline{h}^*$ is 11% higher. Moreover, a 2.5 times reduction in pumping power is obtained. It is clear that both pumping power and thermal performance are strongly affected by the diameter of nozzles. Comparing the S architectures it can be noticed that increasing the number of jets the thermal resistance decreases while the pumping power increases.

7.6 Discussion

The problem of cooling power electronic components is often solved by using cooling fins [87] or heat transfer enhanced surfaces [88]. The use of impinging jets is currently recognised as a viable alternative [83, 89]. A numerical study is presented aiming

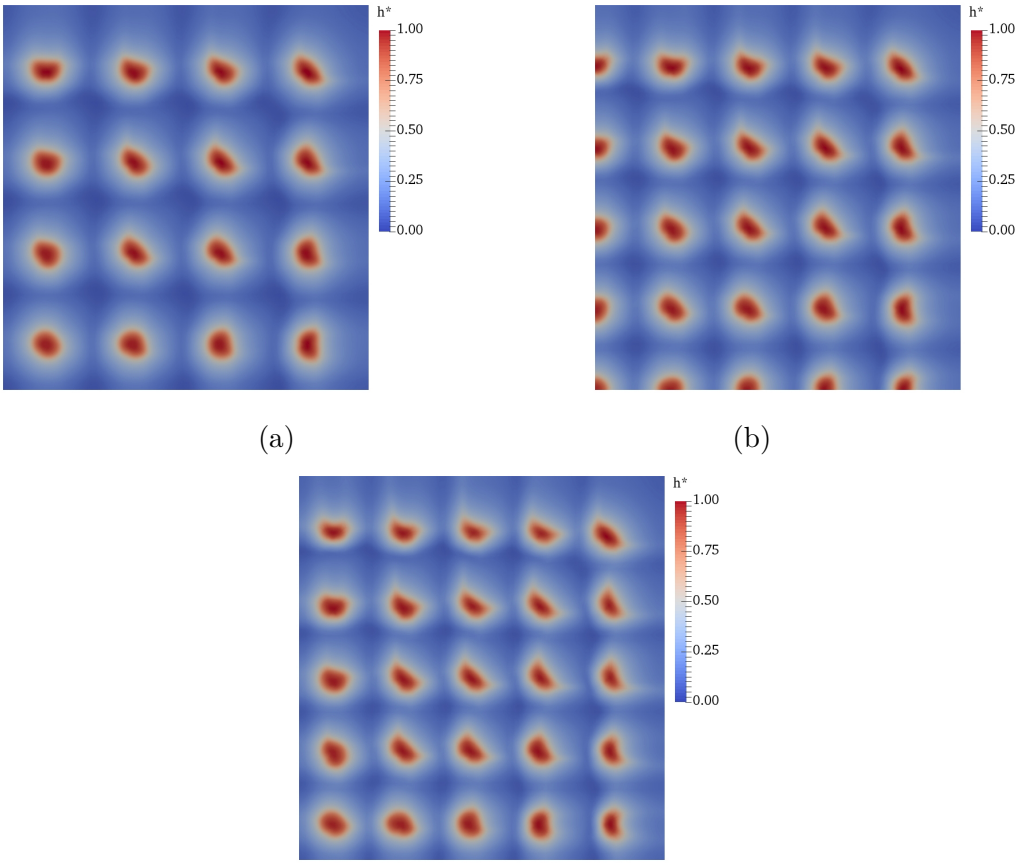

Figure 7.16 Normalised heat transfer coefficient on the impingement plate in configurations: (a) S64, (b) S81 and (c) S100.

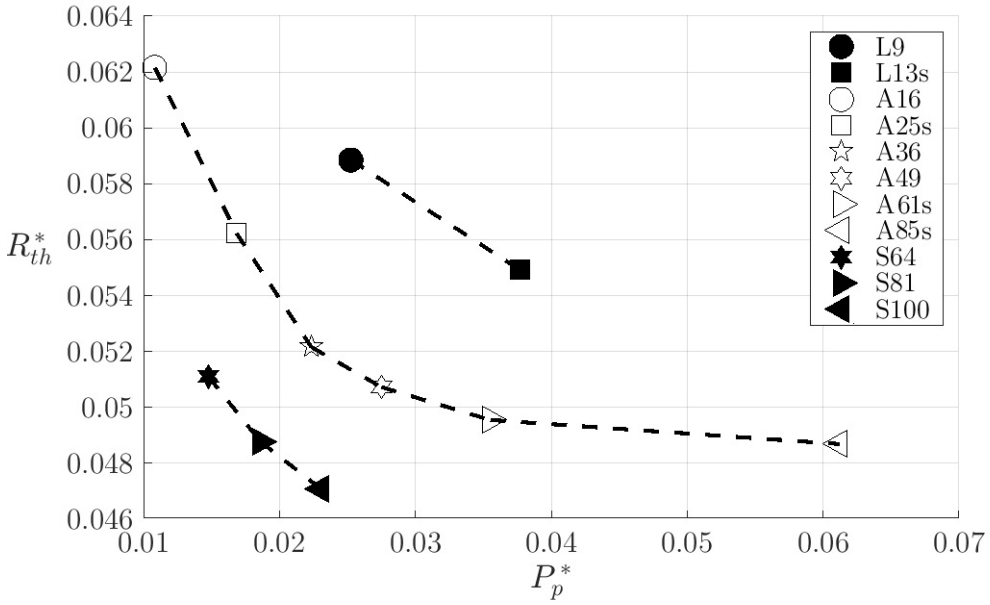

Figure 7.17 Thermal resistance as a function of the pumping power $R^*_{\text{th}}\left(P^*_p\right)$

at the discussion of the main parameters affecting pumping power and heat transfer effectiveness of heat sinks using arrays of impinging jets.

The numerical procedure is developed in the frame of the open-source software OpenFOAM®, and is validated by comparing results of a single, axisymmetric jet simulation against experimental and numerical results. As a consequence of the validation procedure, the SST $\mathrm{k}-\omega$ turbulence model is adopted. Besides validation, also a grid independence study is carried out to identify the most appropriate mesh for simulations.

Several configurations in terms of diameter, number and arrangement of nozzles are investigated, following suggestions in refs. [24, 76, 77, 25, 74, 75]. Results show that a reduction in nozzle diameter leads to an overall heat transfer enhancement, as well as reduced pumping power requirements. In addition it is observed that in configurations with average nozzles diameter ($d_n = 0.050\, l_{\text{ref}}$) and when the number of nozzles grows considerably, only a marginal heat transfer enhancement is achieved while the pumping power increases consistently. This is due to a mass flow rate increase which leads to higher discharge velocities directed towards the outlet boundaries, preventing the orthogonal impingement of jets.

Figures 7.17 and 7.18 summarise the performances of configurations investigated on charts which report R^*_{th} and $\overline{h}^*$ as a function of P^*_p. Promising configurations are characterised by low pumping power, low thermal resistance and high overall heat

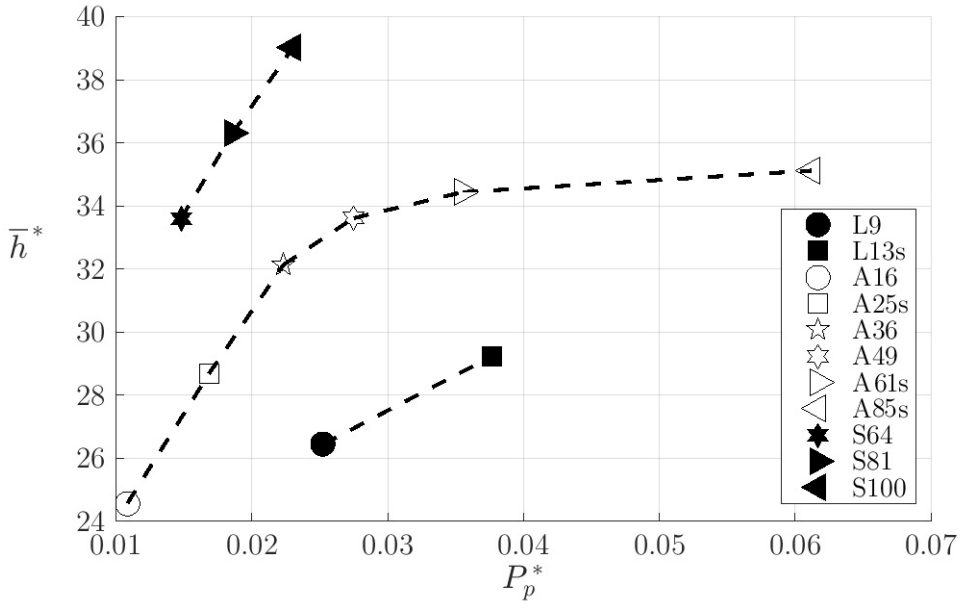

Figure 7.18 Heat transfer coefficient as a function of the pumping power $\overline{h}^*\left(P_p^*\right)$

transfer coefficient, therefore their operating point is placed close to the origin in chart $R_{\text{th}}^*\left(P_p^*\right)$ and in the upper-left part of chart $\overline{h}^*\left(P_p^*\right)$. It is clear that a reduction in nozzle diameters allows for lower thermal resistances (and higher overall heat transfer coefficient) and lower pumping powers. Since the pressure drop is the same for every configuration, a lower pumping power indicates lower mass flow rate, thus in general architectures with smaller d_n^* exchange more heat with less mass flow rate. No further reduction in nozzle diameter is considered because already the minimum d_n considered here (in the order of 0.1 mm) might cause obstructions and fouling. In addition very small diameters make heat exchangers very sensible to construction tolerances. Data pertaining to configurations with average diameter show an asymptotic behaviour: increasing the number of jets beyond a certain number leads to a pumping power increase much larger than the thermal performance enhancement.

In order to limit deviating velocities in the discharge plenum, the mass flow rate across the nozzles needs to be restricted, and this can be done considering an upper limit of the total nozzle area A_n. In the present study $A_n^{(\text{A36})}$, the total nozzle area in configuration A36, is considered as the maximum value of A_n which limits jets deviation. Results obtained in small diameter configurations, which are designed following this constraint, appear to substantiate this limit.

In summary, submerged impinging jets can exchange heat at low costs in terms of mechanical pumping power and are very flexible in terms of geometry allowing for the design heat exchangers specifically tailored to cool specific hot spots.

Chapter 8

Conclusions

Over the last years, hybrid solutions are gaining critical importance in the automotive field. Hybrid Electric Vehicles are equipped with electrical devices such as electrical machines, energy storage, and power converters. The power management among the various components is entrusted to power converters.

The present PhD thesis is devoted to a detailed thermal analysis on power conversion systems.

Since experimental approaches are too expensive in the preliminary evaluation power module devices, a Virtual Test Bench able to address the PC design has been developed and presented. Any converter configuration can be easily investigated at low computational cost. Based on look-up table approach, investigations can cover a large range of working conditions. The presented tool allows to a quick identification of PC configurations which exhibit low efficiency level and suggests design characterized by the low dissipation levels. In this way, only the most promising solutions are selected to be subjected to an eventual experimentation campaign. The numerical tool is able to evaluate PC performance by means an accurate power losses computation. A global analysis including steady-state and time-dependent conditions can be easily conducted, in addition a per-chip investigations help the designers in the understanding of the heat flux density involved. This is quite useful for the choice and the study of the cooling system equipping the power module.

After an accurate validation of the tool, a large simulation campaign is conducted. It is focused on both 2L and 3L PC topologies. They are equipped by Si and SiC devices. In detail, for 2L PC configuration, Infineon IGBT3, Infineon EDT2, and ROHM SiC MOSFET power modules are considered while 3L PC configuration is equipped with Semikron IGBT3 power module. Each configuration is investigated over a large steady-state simulation matrix including 260 points and over two drive cycles.

In general, results denote that differences between IGBT3 and EDT2 in a 2L topology are very small. It is suggested to prefer the EDT2 solution with respect the IGBT3 for low switching frequency application (f_{sw} below 20kHz). 3L topology deserves to be considered when f_{sw} reaches higher value, but SiC MOSFETs are preferred to easily manage power converter losses. When considering the dynamic conditions, the evaluation of the power losses and Usage time maps allow to obtain a detailed analysis of the PC behavior through the drive cycles. Moreover, the impact of the drive cycle on PC performance can be easily investigated. Power losses are quite higher for Cycle 1 than Cycle 2, since its toque level is higher. Finally, critical working conditions can be easily detected in terms of losses and duration. This methodology allows to avoid undesired events and to preserve PC lifetime and performance. In addition, the presented tool allows to split the chip power dissipation in conduction and switching contributions. Power semiconductors exhibit power dissipation in the order of the hundred of W, this lead to high heat flux densities at the chip location since the chip area is in the order of cm^2.

Since the power involved in such power electronic devices is quite high, to ensure performance and lifetime of power semiconductors a cooling system needs to be adopted. Submerged impinging jets are considered one of the most promising solution. To face this problem, a detailed numerical study on submerged impinging jets is presented. A systematic approach has been necessary to understand the effect of the main geometrical parameters in terms of pumping power and heat transfer effectiveness. The numerical activity is performed by using OpenFOAM®. A validation procedure is performed to assess the best set-up condition prior to the study of jet arrays. As a consequence of the validation procedure, the SST $k - \omega$ turbulence model is adopted. Besides validation, also a grid independence study is performed to identify the most appropriate computational grid for simulations. Several configurations in terms of diameter, number and arrangement of nozzles are investigated.

Results show that a reduction in nozzle diameter leads to an overall heat transfer enhancement, as well as reduced pumping power requirements. However, the nozzle diameter cannot be too small, because of manufacturing tolerances and to avoid obstructions. In addition it is observed that in configurations with average nozzles diameter and when the number of nozzles grows considerably, a not significant heat transfer enhancement is achieved while the pumping power increases consistently. This is due to a mass flow rate increase which leads to higher discharge velocities directed towards the outlet boundaries, preventing the orthogonal impingement of jets. In order to limit deviating velocities in the discharge plenum, the mass flow rate across the

nozzles needs to be restricted, and this can be done considering an upper limit of the total nozzle area A_n. In the present study $A_n^{(\mathrm{A36})}$, the total nozzle area in configuration A36, is considered as the maximum value of A_n which limits jets deviation. Results obtained in small diameter configurations, which are designed following this constraint, appear to substantiate this limit.

Finally, the present study has allowed to perform a detailed investigation of power conversion system from a thermal point of view. The prediction of power losses of the power converter by means the developed Virtual Test Bench is accurate and quick. Hence, the tool is deemed promising and can be recommended for the use in the preliminary design of power converters. In addition, the tool can be furthermore developed to allow a multi-objective optimization procedures with the aim to improve the power converter behavior for determinate operating conditions or load cycles. Furthermore, the tool can estimate the power dissipation affecting the semiconductors. This information plays an important role for the study of the power converter thermal management system. For the specific case treated in this work, array of submerged impinging jets can exchange heat at low costs in terms of mechanical pumping power. Moreover, they are very flexible in terms of geometry allowing for the design heat exchangers specifically tailored to cool specific hot spots. Moreover, the 3D-CFD activity has allowed to obtain also a thermal resistance evaluation of the various configurations investigated. They can represent the junction-to-water thermal resistance of a thermal Foster network. Therefore, it indicates that the 3D-CFD activity can support the development of the Virtual Test Bench thermal model by providing such information which depends by thermal management system involved.

Bibliography

[1] K. C. Prajapati, R. Patel, and R. Sagar. Hybrid vehicle: A study on technology. *International Journal of Engineering Research & Technology*, 3:1076–1082, 2014.

[2] D. S. Cardoso, P. O. Faela, and A. Espírito-Santo. A review of micro and mild hybrid systems. *Energy Reports*, 6:385–390, 2020.

[3] O. M. Govardhan. Fundamentals and classification of hybrid electric vehicles. *International Journal of Engineering and Techniques*, 3:194–198, 2017.

[4] Fia f1, $https://www.formula1.com/$.

[5] Y. Ren, M. Xu, J. Zhou, and F. C. Lee. Analytical loss model of power mosfet. *IEEE Transaction on Power Electronics*, 21(2):310–319, January 2006.

[6] H. Hafezi and R. Faranda. A new approach for power losses evaluation of igbt/diode module. *Electronics*, 10(3):1–21, January 2021.

[7] U. Drofenik and J. Kolar Kolar. A general scheme for calculating switching- and conduction-losses of power semiconductors in numerical circuit simulations of power electronic systems. 01 2005.

[8] M. Schweizer, T. Friedli, and J. W. Kolar. Comparison and implementation of a 3-level npc voltage link back-to-back converter with sic and si diodes. In *2010 Twenty-Fifth Annual IEEE Applied Power Electronics Conference and Exposition (APEC)*, pages 1527–1533, Feb 2010.

[9] R. Yapa, A. J. Forsyth, and R. Todd. Analysis of sic technology in two-level and three-level converters for aerospace applications. In *7th IET International Conference on Power Electronics, Machines and Drives (PEMD 2014)*, pages 1–6, April 2014.

[10] H. Nabadi. *OPTIMAL PIN FIN HEAT EXCHANGER SURFACE*. Malardalen University Sweden, 2008.

[11] D. Poulikakos, W. Escher, and B. Michel. A novel high performance, ultra thin heat sink for electronics. *International Journal of Heat and Fluid Flow*, 31:640–655, 2010.

[12] Xiang-Qi Wang, A. S. Poulikakos, and C. Yap. Thermal characteristics of tree-shaped microchannel nets for cooling of a rectangular heat sink. *International Journal of Thermal Sciences*, 45(11):1103–1112, November 2006.

[13] N. Baraldi, A. Fregni, M. Sabato, E. Stalio, F. Brusiani, M. Tranchero, and T. Baritaud. Comparison between cooling strategies for power electronic devices: fractal mini-channels and arrays of impinging submerged jets. In *Journal of Physics: Conference series; 36th UIT Heat Transfer Conference*, 1 2019.

[14] Y. Chen and P. Cheng. Heat transfer and pressure drop in fractal tree-like microchannel nets. *International Journal of Heat and Mass Transfer*, 45(13):2643–2648, June 2002.

[15] X. Q Wang, A. S. Mujumadar, and C. Yep. Thermal characteristics of tree-shaped microchannel nets for cooling of a rectangular heat sink. *International Journal of Thermal Sciences*, 45:1103–1112, February 2006.

[16] S. M. Senn and D. Poulikakos. Laminar mixing, heat transfer and pressure drop in tree-like microchannel nets and their application for thermal management in polymer electrolyte fuel cells. *Journal of Power Sources*, 140(1-2):178–191, May 2004.

[17] W. Escherab, B. Michela, and D. Poulikakosb. Efficiency of optimized bifurcating tree-like and parallel microchannel networks in the cooling of electronics. *International Journal of Heat and Mass Transfer*, 52(5-6):1421–1430, February 2009.

[18] M. Sabato, A. Fregni, E. Stalio, F. Brusiani, M. Tranchero, and T. Baritaud. Numerical study of submerged impinging jets for power electronics cooling. *International Journal of Heat and Mass Transfer*, 141:707–718, 10 2019.

[19] Arendt Wintrich, Ulich Nicolai, Werner Tursky, and Tobias Reimann. *Application Manual Power Semiconductros*. SEMIKRON International GmbH, 2 edition, 2015.

[20] Infineon Technologies. Fs400r07a1e3_s7, *https* : *//www.infineon.com/dgdl/infineon − fs*400*r*07*a*1*e*3$_s$7 *− ds − v*03$_0$2 *− en.pdf?fileid* = 5546*d*46262*b*31*d*2*e*0163019334*ad*33*a*3.

[21] Infineon Technologies. Fs820r08a6p2b, *https* : *//www.infineon.com/dgdl/infineon − fs*820*r*08*a*6*p*2*b − datasheet − v*03$_0$1 *− en.pdf?fileid* = 5546*d*4625*fe*36784015*fe*7*bf*8*e*872948.

[22] ROHM Semiconductors. S4103, *https* : *//fscdn.rohm.com/en/products/databook/datasheet/discrete/sic/mosfet/s*4103*− e.pdf*.

[23] Semikron GmbH. Skim401mli07e4, *https* : *//www.semikron.com/products/product − classes/igbt − modules/detail/skim*401*mli*07*e*4 *−* 23918910*.html*.

[24] Suresh V Garimella and Boris Nenaydykh. Nozzle-geometry effects in liquid jet impingement heat transfer. *International Journal of Heat and Mass Transfer*, 39(14):2915–2923, 1996.

[25] Chin-Yuan Li and Suresh V Garimella. Prandtl-number effects and generalized correlations for confined and submerged jet impingement. *International Journal of Heat and Mass Transfer*, 44(18):3471–3480, 2001.

[26] GK Morris, SV Garimella, and RS Amano. Prediction of jet impingement heat transfer using a hybrid wall treatment with different turbulent Prandtl number functions. *Journal of heat transfer*, 118(3):562–569, 1996.

[27] Garron K Morris and Suresh V Garimella. Orifice and impingement flow fields in confined jet impingement. *Journal of Electronic Packaging*, 120(1):68–72, 1998.

[28] D. Zhu and X. Zheng. Fuel consumption and emission characteristics in asymmetric twin-scroll turbocharged diesel engine with two exhaust gas recirculation circuits. *Applied Energy*, 238:985–995, 2019.

[29] J. Zhao, Q. Xi, S. Wang, and S. Wang. Improving the partial-load fuel economy of 4-cylinder si engines by combining variable valve timing and cylinder-deactivation through double intake manifolds. *Applied Thermal Engineering*, 141:245–256, 2018.

[30] J. D. Osorio and A. Rivera-Alvarez. Efficiency enhancement of spark-ignition engines using a continuous variable valve timing system for load control. *Energy*, 161:649–662, 2018.

[31] N. E. Galushkin, N. N. Yazvinskaya, and D. N. Galushkin. A critical review of using the peukert equation and its generalizations for lithium-ion cells. *Journal of Electrochemical Society*, 167(12), August 2020.

[32] A. Rufer. *Energy Storage:System and Components*. Taylor & Francis Ltd, 2017.

[33] Paul C. Krause, Oleg Wasynczuk, and Scott D. Sudhoff. *Analysis of Electric Machinery and Drive Systems*. John Wiley & Sons, Ltd, 2013.

[34] *Speedś Electric Motors*. TJE Miller University of Glasgow, 2002-2007.

[35] A. E. Fitzgerald, C. Kingsley, and S. D. Umans. *Electric Machinery*. Mcgraw-Hill Education - Europe, 2002-2007.

[36] G. Cimini, D. Bernardini, A. Bemporad, and S. Levijoki. Online model predictive torque control for permanent magnet synchronous motors. *IEEE International Conference on Industrial Technology (ICIT)*, pages 2308–2313, 2015.

[37] M. Morandin. *Electric Drives with Permanent Magnet Synchronous Machines Connected to Internal Combustion Engines*. PhD thesis, UNIVERSITÀ DEGLI STUDI DI PADOVA, 2013.

[38] A. Soliman, R. Alammari, M. El-Hawary, and A.H. Mantaway. Parks transformation application for power system harmonics identification and measurements. *Electric Power Components and Systems*, 31(8):778–789, 10 2003.

[39] S. Morimoto, M. Sanada, and Y. Takeda. Wide-speed operation of interior permanent magnet synchronous motors with high-performance current regulator. *IEEE TRANSACTIONS ON INDUSTRY APPLICATIONS*, 30:920–926, 1994.

[40] S. Kim, Y. Yoon, S. Sul, and K. Ide. Maximum torque per ampere (mtpa) control of an ipm machine based on signal injection considering inductance saturation. *IEEE Transactions on Power Electronics*, 28(1):488–497, 1 2015.

[41] T. S. Kwon and S. K. Sul. Novel antiwindup of a current regulator of a surface-mounted permanent-magnet motor for flux-weakening control. *IEEE Transactions on Industry Applications*, 42(5):1293–1300, 9 2006.

[42] M. Caruso, A. O. Di Tommaso, R. Miceli, C. Nevoloso, C. Spataro, and C. Trapanese. Maximum torque per ampere control strategy for low-saliency ratio ipmsms. *International Journal of Renewable Energy Research*, 9(1), 3 2019.

[43] D. Lu, N. C. Kar, and N. C. Kar. A review of flux-weakening control in permanent magnet synchronous machines. *2010 IEEE Vehicle Power and Propulsion Conference*, 9 2010.

[44] Erickson R.W. and Makrimovic D. *Fundamentals of Power Electronics*. KLUWER ACADEMIC PUBLISHERS, 2004.

[45] Sedra A. S. and Smith K. C. *Microelectronic Circuits*. OXFORD University Press, 2010.

[46] Rashid M.H. *POWER ELECTRONICS HANDBOOK*. Academic Press, 2001.

[47] A. Sproul. Understanding the p-n junction. *Solar Cells: Resource for the Secondary Science Teacher*, pages 13–24.

[48] D. Holmes and T. Lipo. *Pulse Width Modulation for Power Converters: Principles and Practice*. John Wiley & Sons, 2003.

[49] J. Holts. Pulsewidth modulation for electronic power conversion. *Proceeding of Transactions*, 82(8):1194–1214, 1994.

[50] Andreas Volke and Michael Hornkamp. *IGBT Modules*. Infineon TEchnologies AG, 2 edition, 2012.

[51] X. Hu, S. Lin, S. Stanton, and W Lian. A foster network thermal model for hev7ev battery modeling. *IEEE Transaction on Industry Applications*, 2(3):1692–1699, May 2011.

[52] E. Khun, C. Forgez, P. Lagonotte, and G. Friedrich. Modelling ni-mh battery using cauer and foster structures. *Journal of Power Souces*, 158(2):1490–1497, Dicember 2005.

[53] J. K. Reed, J. McFarland, J. Tangudu, E. Vinot, R. Trigui, G. Venkataramanan, S. Gupta, and T. Jahns. Modeling power semiconductor losses in hev powertrains using si and sic devices. In *2010 IEEE Vehicle Power and Propulsion Conference*, pages 1–6, Sep. 2010.

[54] Angus T. Bryant, Nii-Adotei Parker-Allotey, and Patrick R. Palmer. The use of condition maps in the design and testing of power electronic circuits and devices. *IEEE Transactions on Industry application*, 43(4):902–910, July-August 2007.

[55] Z. Asus, El-Hassane Algzim, D. Cherenko, Zul-Hilmi Che Daud, and L. Le Moyne. Dynamic modeling and driving cycle prediction for a racing series hybrid car. *IEEE Journal of Emerging and Selected Topics in Power Electronics*, 2(3):541–551, September 2014.

[56] S. Munk-Nielsen, L. N. Tutelea, and U. Jaeger. Simulation with ideal switch models combined with measured loss data provides a good estimate of power loss. In *Conference Record of the 2000 IEEE Industry Applications Conference. Thirty-Fifth IAS Annual Meeting and World Conference on Industrial Applications of Electrical Energy (Cat. No.00CH37129)*, volume 5, pages 2915–2922 vol.5, Oct 2000.

[57] MATLAB/Simulink. Matlab/simulink, $https : //it.mathworks.com/?s_tid = gn_logo$.

[58] A.P. Arribas, F. Shang, M. Krishnamurthy, and K. Shenai. Simple and accurate circuit simulation model for sic power mosfets. *IEEE Transactions on Electron Devices*, 62(2):449–457, April 2015.

[59] M. Shen and S. Krishnamurthy. Simplified loss analysis for high speed sic mosfet inverter. In *2012 Twenty-Seventh Annual IEEE Applied Power Electronics Conference and Exposition (APEC)*, Mar 2012.

[60] D. Christen and J. Biela. Analytical switching loss modelling based on datasheet parameters for mosfets in a half-bridge. *IEEE Transactions on Power Electronics*, 34(4):3700–3710, April 2019.

[61] Ingo Staudt. *3L NPC & TNPC Topology*. SEMIKRON International GmbH, 10 2015. Rev. 5.

[62] YOKOGAWA. Wt1800 high performance power analyzer, $https : //tmi.yokogawa.com/solutions/discontinued/wt1800 - high - performance - power - analyzer/$.

[63] YOKOGAWA. Wt1800 high performance power analyzer, $https : //cdn.tmi.yokogawa.com/imwt1801 - 02en.pdf$.

[64] Semikron GmbH. Semisel simulation, free support for your converter design, $https : //www.semikron.com/service - support/semisel - simulation.html$.

[65] A. Christmann and D. Levett. Design considerations for next generation traction drive IGBT based power modules. In *2016 IEEE Transportation Electrification Conference and Expo (ITEC)*, pages 1–5, 2016.

[66] M. Schweizer, I. Lizama, T. Friedli, and J. W. Kolar. Comparison of the chip area usage of 2-level and 3-level voltage source converter topologies. In *IECON 2010 - 36th Annual Conference on IEEE Industrial Electronics Society*, Nov 2010.

[67] K. Nishizawa, T. Kinoshita, and J. Itoh. Optimization for the number of parallel-connected switching devices in high-efficiency high-power converters. In *PCIM Europe 2019; International Exhibition and Conference for Power Electronics, Intelligent Motion, Renewable Energy and Energy Management*, Jul 2019.

[68] F. P. Incropera, D. P. Dewitt, T. L. Bergman, and A. S. Lavine. *Fundamentals of Heat and Mass Transfer*. JOHN WILEY and SONS, 111 River Street, Hoboken, NJ, 2007.

[69] K Kataoka, M Suguro, H Degawa, K Maruo, and I Mihata. The effect of surface renewal due to largescale eddies on jet impingement heat transfer. *International Journal of Heat and Mass Transfer*, 30(3):559–567, 1987.

[70] DJ Womac, S Ramadhyani, and FP Incropera. Correlating equations for impingement cooling of small heat sources with single circular liquid jets. *Journal of heat transfer*, 115(1):106–115, 1993.

[71] SW Churchill and R Usagi. A general expression for the correlation of rates of transfer and other phenomena. *AIChE Journal*, 18(6):1121–1128, 1972.

[72] Robert Gardon and J Cahit Akfirat. The role of turbulence in determining the heat-transfer characteristics of impinging jets. *International journal of heat and mass transfer*, 8(10):1261–1272, 1965.

[73] BR Hollworth and SI Wilson. Entrainment effects on impingement heat transfer: Part i—measurements of heated jet velocity and temperature distributions and recovery temperatures on target surface. *Journal of heat transfer*, 106(4):797–803, 1984.

[74] Suresh V Garimella and RA Rice. Confined and submerged liquid jet impingement heat transfer. *Journal of Heat Transfer*, 117(4):871–877, 1995.

[75] Suresh V Garimella. Influence of nozzle geometry on heat transfer in submerged and confined liquid jet impingement. *Proceedings of the ASME Cooling and Thermal Design of Electronic Systems, 1995*, 1995.

[76] Anja Royne and Christopher J Dey. Effect of nozzle geometry on pressure drop and heat transfer in submerged jet arrays. *International Journal of Heat and Mass Transfer*, 49(3-4):800–804, 2006.

[77] Brian P Whelan and Anthony J Robinson. Nozzle geometry effects in liquid jet array impingement. *Applied Thermal Engineering*, 29(11-12):2211–2221, 2009.

[78] Janice A Fitzgerald and Suresh V Garimella. A study of the flow field of a confined and submerged impinging jet. *International journal of heat and mass transfer*, 41(8-9):1025–1034, 1998.

[79] David B Tuckerman and Roger Fabian W Pease. High-performance heat sinking for VLSI. *IEEE Electron device letters*, 2(5):126–129, 1981.

[80] M. D. McGuinness. *Flow with a separation bubble:steady and unsteady aspects*. PhD thesis, Cambridge University Engineering Department, 1978.

[81] J. A. Fitzgerald. Fluid flow through an axisymmetric jet nozzle. Technical report, Independent Study Report, Mechanical Engineering Department, University of Wisconsin-Milwaukee, 1994.

[82] A. J. Ward-Smith. *Pressure Losses in Ducted Flows*. Butterworths, London, 1971.

[83] AJ Robinson and E Schnitzler. An experimental investigation of free and submerged miniature liquid jet array impingement heat transfer. *Experimental Thermal and Fluid Science*, 32(1):1–13, 2007.

[84] G Nasif, R Balachandar, and RM Barron. Conjugate analysis of wall conduction effects on the thermal characteristics of impinging jets. *International Journal of Heat and Mass Transfer*, 116:259–272, 2018.

[85] Prithvi Sai Penumadu and Arvind Gangoli Rao. Numerical investigations of heat transfer and pressure drop characteristics in multiple jet impingement system. *Applied Thermal Engineering*, 110:1511–1524, 2017.

[86] Holger Martin. Heat and mass transfer between impinging gas jets and solid surfaces. In *Advances in heat transfer*, volume 13, pages 1–60. Elsevier, 1977.

[87] Sidy Ndao, Yoav Peles, and Michael K Jensen. Multi-objective thermal design optimization and comparative analysis of electronics cooling technologies. *International Journal of Heat and Mass Transfer*, 52(19-20):4317–4326, 2009.

[88] Orsola Errico and Enrico Stalio. Direct numerical simulation of turbulent forced convection in a wavy channel at low and order one Prandtl number. *International Journal of Thermal Sciences*, 86:374–386, 2014.

[89] Gregory J Michna, Eric A Browne, Yoav Peles, and Michael K Jensen. The effect of area ratio on microjet array heat transfer. *International Journal of Heat and Mass Transfer*, 54(9-10):1782–1790, 2011.